AD–A115 713   BATTELLE COLUMBUS LABS OH   F/G 9/1
           STUDY OF THE EFFECTS OF SURFACE ROUGHNESS AND TI DIFFUSION ON I--ETC(U)
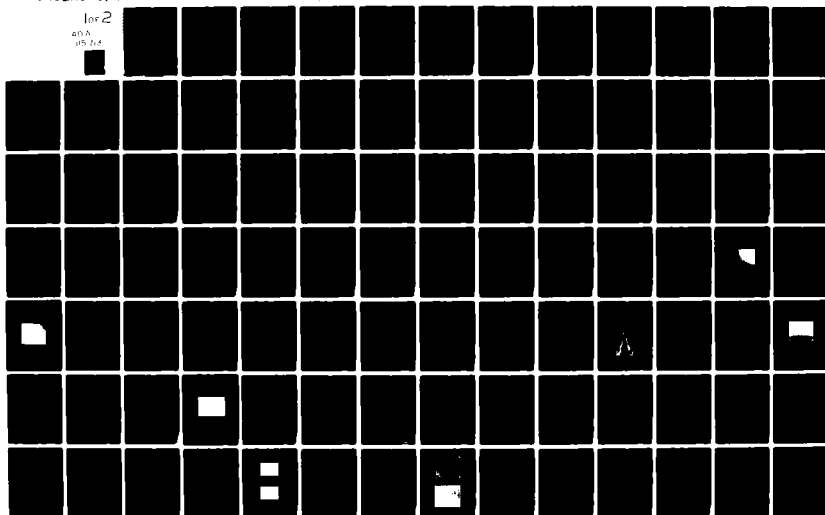   MAR 82   D W VAHEY, J R BUSCH   N00173-80-C-0420
UNCLASSIFIED   NL

1 of 2

STUDY OF THE EFFECTS OF SURFACE ROUGHNESS AND
Ti DIFFUSION ON IN-PLANE SCATTERING IN Ti-LiNbO$_3$
WAVEGUIDES

David W. Vahey and James R. Busch
BATTELLE
Columbus Laboratories
505 King Avenue
Columbus, Ohio 43201

March 31, 1982

Final Report for the Period September 20, 1980 – November 19, 1981

Prepared for

NAVAL RESEARCH LABORATORY
Washington, DC 20375

DTIC
JUN 1 7 1982

F

STUDY OF THE EFFECTS OF SURFACE ROUGHNESS AND
Ti DIFFUSION ON IN-PLANE SCATTERING IN Ti-LiNbO$_3$
WAVEGUIDES

David W. Vahey and James R. Busch
BATTELLE
Columbus Laboratories
505 King Avenue
Columbus, Ohio 43201

March 31, 1982

Final Report for the Period September 20, 1980 - November 19, 1981

REPORT DOCUMENTATION PAGE	READ INSTRUCTIONS BEFORE COMPLETING FORM

1. REPORT NUMBER	2. GOVT ACCESSION NO. $AD-A115749$	3. RECIPIENT'S CATALOG NUMBER

4. TITLE (and Subtitle)	5. TYPE OF REPORT & PERIOD COVERED
STUDY OF THE EFFECTS OF SURFACE ROUGHNESS AND Ti DIFFUSION ON IN-PLANE SCATTERING IN Ti-LiNbO$_3$ WAVEGUIDES	Final - 9/20/80 - 11/19/81
	6. PERFORMING ORG. REPORT NUMBER

7. AUTHOR(s)	8. CONTRACT OR GRANT NUMBER(s)
David W. Vahey and James R. Busch	N00173-80-C-0420

9. PERFORMING ORGANIZATION NAME AND ADDRESS	10. PROGRAM ELEMENT, PROJECT, TASK AREA & WORK UNIT NUMBERS
Battelle Columbus Laboratories 505 King Avenue Columbus, OH 43201	

11. CONTROLLING OFFICE NAME AND ADDRESS	12. REPORT DATE
Naval Research Laboratory Washington, DC 20375	March 26, 1982
	13. NUMBER OF PAGES

14. MONITORING AGENCY NAME & ADDRESS(if different from Controlling Office)	15. SECURITY CLASS. (of this report)
	15a. DECLASSIFICATION/DOWNGRADING SCHEDULE

16. DISTRIBUTION STATEMENT (of this Report)

This document has been approved for public release and sale; its distribution is unlimited.

17. DISTRIBUTION STATEMENT (of the abstract entered in Block 20, if different from Report)

18. SUPPLEMENTARY NOTES

19. KEY WORDS (Continue on reverse side if necessary and identify by block number)

integrated optics, optical waveguides, LiNbO$_3$, Ti-diffusion, spectrum analyzer, scattering

20. ABSTRACT (Continue on reverse side if necessary and identify by block number)

The primary objective of this program has been to understand and subsequently reduce the sources of scattering in planar Ti-diffused LiNbO$_3$ waveguides. On the basis of previous work these were perceived to be surface roughness and surface index inhomogeneities associated with Li-Ti-O compound formation during diffusion. A secondary objective has been to characterize state-of-the-art waveguides to determine their potential for use in an integrated optical spectrum analyzer providing at least 40 dB dynamic range at the fourth off-axis pixel. A key ingredient to meeting these objectives was found to be the accurate determination of

DD $_{1\ JAN\ 73}^{FORM}$ 1473   EDITION OF 1 NOV 65 IS OBSOLETE

20.

waveguide scattering parameters from in-plane scattering measurements. These were frustrated by superimposed background scattering associated with input and output coupling. Both prism and end-fire techniques were used. A statistical analysis employed to effectively subtract the background contribution provided this best estimate: Existing waveguides provide the 40 dB dynamic range at the fourth pixel that is marginally acceptable for the spectrum analyzer application; however, a $\pm$ 5 dB uncertainty in dynamic range is within one standard deviation of our average value. In the case of 35 dB dynamic range at the fourth pixel, consistent with this uncertainty, an analysis of dynamic range versus pixel number is used to show that 40 dB dynamic range is still achieved at the tenth off-axis pixel.

Among the accomplishments of the program are (1) a formalism for calculating dynamic range given values for scattering parameters, (2) An analysis of scattering mechanisms to determine their probable importance to limiting spectrum analyzer dynamic range, and (3) development of statistical methods for analyzing in-plane scattering data. No information was generated indicating the superiority of any of the common methods for fabricating Ti-diffused $LiNbO_3$ waveguides. However, a previously unnoticed effect was observed in which a good-quality waveguide degraded after thermal treatments at temperatures less than 500°C. This may have to do with the use of certain fabrication methods designed to eliminate the Li_2O outdiffusion effect.

Accession For

NTIS GRA&I   ☑
DTIC TAB   ☐
Unannounced   ☐
Justification

FL-182 on file

By_____
Distribution/
Availability Codes
        Avail and/or
Dist   Special

A

DTIC
COPY
INSPECTED
3

TABLE OF CONTENTS

TABLE OF CONTENTS
(Continued)

LIST OF FIGURES

Page

LIST OF TABLES

v

I. INTRODUCTION

This report describes a research program to determine the sources
of scattering in Ti-diffused $LiNbO_3$ waveguides, to eliminate or reduce these
sources and their effects, and to evaluate the finished waveguides for their
potential use in the integrated optical spectrum analyzer (IOSA) application.[1]
The motive for the research is the fact that light scattered in the plane of
the waveguide can arrive at unintended elements in the IOSA detector array.
Scattering is therefore a source of noise that limits the smallest detectable
information signal, or equivalently, the dynamic range of the system. Reduc-
tion in waveguide scattering, especially in-plane waveguide scattering, is
therefore useful in improving the dynamic range of systems like the IOSA, and
in helping these systems to attain their maximum theoretical potential.

The logical plan for scattering reduction research involves the use
of diagnostic tools for "visualizing" the scattering centers, the development
of waveguide fabrication or processing techniques to reduce the density and/or
the scattering cross section of these scattering sources, the development of
waveguide evaluation procedures for verifying the quality of the waveguides,
and a theory to relate the measured level of scattering to the performance of
integrated optical systems, such as the IOSA, that will employ the waveguides.

We report only limited success in achieving the first three of these
tasks, experimental in nature. A variety of standard diagnostic tools have been
tested for their ability to provide information about the size and density of
scattering centers. These include differential-interference-phase-contrast
microscopy, scanning electron microscopy, e-beam X-ray analysis, and multiple-
beam-interference microscopy. In general, we find direct evidence of scatter-
ing centers only in waveguides that have been purposely fabricated under adverse
conditions. Conventional fabrication methods produce waveguides that have no
apparent scattering centers as determined by the diagnostic methods listed above.

This negative result has motivated us to look for scattering centers
by indirect methods. The measurement of in-plane scattering is one such method.
It is an important one in that it provides the ultimate information as to how
the waveguide will function in an integrated optical signal processing applica-
tion. With in-plane scattering measurements, we can at least predict how a
waveguide will perform in a specific application, even if we can't identify
the actual scattering centers at work.

In-plane scattering can further serve as a diagnostic tool if careful models of waveguide scattering centers are constructed. To do this, we identify those steps in the waveguide fabrication procedure where inhomogeneities are likely to be introduced into the material. We estimate or otherwise determine the refractive index difference associated with a specific inhomogeneity, and then we determine if reasonable values of scattering center size and density on the waveguide surface produce a calculated level of in-plane scattering consistent with measured levels. If so, the scattering mechanism being considered is a plausible one worthy of further consideration. This may involve modifying the waveguide fabrication process to effect a change in the candidate scattering mechanism, and then checking to see that the in-plane scattering is similarly affected. A good example is that of scattering by surface roughness. If measured levels of scattering are consistent with a certain level of surface roughness, then polishing of the surface should result in a decreased level of in-plane scattering. If it does not, volume scattering centers are indicated, and a different set of fabrication procedures may be employed to learn the source of these.

This indirect approach has provided the main thrust of our work in the absence of useful diagnostic tools. However, even this approach has been frustrated by the difficulties encountered in taking reliable in-plane scattering data. The measurements invariably contain a background scattering contribution associated with input and output coupling from the waveguide. This contribution compares with and in some cases dominates the scattering from the waveguide that we wish to measure. As a result, the error bars on the experiments are too large to permit us to draw conclusions regarding the efficacy of various modifications of the waveguide fabrication procedure. As far as we can tell from our experiments, a wide range of Ti-film thicknesses, diffusion times and temperatures are useful in producing equally good waveguides. The most promising interpretation of our experimental results shows that the waveguides are better than required to meet dynamic range specifications for an integrated optical spectrum analyzer. The most negative interpretation is that 5 dB improvement is still required.

For the near term then, the question as to whether waveguide quality is sufficient for integrated-optical-systems applications will have to be answered by the fabrication and characterization of those systems. The present research will be useful as a starting point to those who may continue it. Additionally, we have identified two promising candidates for in-plane

2

scattering and eliminated several others. The two promising candidates are surface roughness and near-surface inhomogeneities associated with the diffusion process. The latter may be the lithium titanate compounds identified by Burns et al[2] using Secondary Ion Mass Spectroscopy (SIMS). The relative importance of these candidate scattering mechanisms may be determined by performing SIMS, Talystep profilometry and in-plane scattering measurements on samples fabricated using a variety of procedures. This was in fact the plan of the most recent research, but it was not implemented in view of the in-plane scattering experimental problem. Our effort was reduced to in-plane scattering measurements on existing waveguides to determine as accurately as possible the suitability of those waveguides for an integrated optical spectrum analyzer. The origin of scattering centers in the waveguides was not addressed experimentally.

The organization of this report is as follows. In Section II, we derive the IOSA dynamic range dependence on generalized scattering parameters such as Σ, the surface density in cm^{-2} of scattering centers, and $\sigma(\phi)$ the differential scattering cross section. Then we derive expressions for $\sigma(\phi)$, in terms of the characteristic size and refractive index of the scattering centers. This leads us to the consideration of three distinct scattering regimes: Rayleigh scattering from inhomogeneities small compared to a wavelength, Rayleigh-Gans-Debye scattering from inhomogeneities larger than a wavelength but with a small refractive index difference from the environment, and Mie scattering from inhomogeneities larger than a wavelength and having a large refractive index difference from the environment.

In Section III, we will consider a variety of possible scattering mechanisms including surface roughness, the formation of lithium-titanate compounds, the formation of the separated phase $LiNb_3O_8$, and nonuniform distribution of diffused Ti. We will select a range of scattering parameters associated with each mechanism and use these to calculate theoretical values of IOSA dynamic range. This exercise is useful in that it tells us which scattering mechanisms are likely to have the most impact on IOSA dynamic range, and which mechanisms are likely to be unimportant even if they are present. Perhaps the most significant piece of information generated here is the likelihood that Rayleigh scattering is not a factor limiting dynamic range if waveguide attenuation losses are 1/4 dB/cm or less.

3

In Section IV we will present our experimental results and interpret them in relation to the analysis of Sections II and III. We will begin with results showing the total integrated scattering measured as a function of prism separation. These results suggest the importance and even the dominance of prism-associated scattering to the total scattering generated in the free waveguide. We will describe attempts to avoid this problem using end-fire coupling techniques, longer waveguide paths, and a novel optical geometry that distinguishes between waveguide scattering and scattering generated at the point of input coupling. Finally, we will discuss results corrected for prism scattering by acquiring data at two different coupling prism separations, and then subtracting to get the free-waveguide contribution. The results will be associated with waveguides formed using a wide variation of fabrication conditions and waveguides fabricated at another laboratory.

In Section V we present our conclusions as to likely sources of scattering, best methods for fabricating waveguides to minimize the effects of these sources, and finally, the prospects for achieving an integrated-optical spectrum analyzer having the desired 40 dB dynamic range.

II. THE EFFECTS OF OPTICAL WAVEGUIDE SCATTERING ON IOSA DYNAMIC RANGE

CHARACTERIZATION OF THE SCATTERING PHENOMENON

The effect of in-plane waveguide scattering on the dynamic range of an IOSA depends on the design geometry of the device and on the scattering parameters of the waveguide. The scattering effect of a single scattering center may be characterized by a differential cross section $\sigma(\phi)$ defined as follows: If I is the optical power per unit width of the confined beam at the location of the scattering center, then

$$\Delta P = I\sigma(\phi)\Delta\phi \qquad (1)$$

is the power scattered in the plane of the waveguide at an angle ϕ into an angular sector $\Delta\phi$. The total scattered power is obtained by summing the individual contributions described by Eq. (1). This is most readily done by taking $\sigma(\phi)$ to be a statistically averaged cross section for the ensemble of scattering centers, by taking the scattering centers to be uniformly distributed with a density $\Sigma[\text{cm}^{-2}]$ over the waveguide surface, and by integrating Eq. (1) over the area spanned by the waveguided beam. The total power scattered into the sector $\Delta\phi$ at an angle ϕ is found to be

$$\Delta P_{tot} = P\Sigma L\sigma(\phi)\Delta\phi \ , \qquad (2)$$

where L is the path length and P is the power in the unscattered beam. It is assumed that P is not significantly depleted over the path length by either scattering or absorption phenomena.

A measurmement of ΔP_{tot} versus ϕ enables us to determine the product $\Sigma\sigma(\phi)$. With this information and knowledge of the device geometry, we can predict the dynamic range of an IOSA. The mathematical analysis, as we will present it, requires the specification of the functional form of $\sigma(\phi)$. This depends, in general, on the size and refractive index of the scattering centers. However, certain simplifications result in the special cases of Rayleigh scattering (RS) and Rayleigh-Gans-Debye scattering (RGDS). For the latter, we will use

$$\sigma(\phi) = \sigma(0) \; [1 + (ka\phi)^2]^{-1} \qquad\qquad (3)$$

where $k = 2\pi/\lambda$, λ is the wavelength in the material, a is the characteristic scattering center size, (assuming $a \gg \lambda$ for RGDS), and ϕ is the scattering angle in the material, given in radians. The Lorentzian form for $\sigma(\phi)$ has been derived by Marcuse,[3] and we will later show its appropriateness using a somewhat different analysis. For Rayleigh scattering, the form of the scattering cross section is complicated by the waveguide geometry. We will use formulas derived for uniform three-dimensional space, but applied only in the plane of the waveguide. They are

$$\sigma(\phi) = \sigma(0) \; \cos^2 \phi, \text{ (TE polarization)}, \qquad\qquad (4)$$

$$\sigma(\phi) = \sigma(0) \; , \text{ (TM polarization)}.$$

The case of Mie scattering is too complicated to be dealt with rigorously here. Generally the angular range will be intermediate to the small angular range for RGD scattering and the large range for Rayleigh scattering. This will enable us to qualitatively discuss the case of Mie scattering in relation to our findings for Rayleigh and RGD scattering.

CHARACTERIZATION OF THE IOSA GEOMETRY

Spectrum analyzer dynamic range depends on design parameters as well as scattering parameters. Figure 1 shows the system geometry used in the Westinghouse IOSA.[4] The actual numerical values for the parameters listed in Fig. 1 are shown in Table I. We have called attention to four different regions of the spectrum analyzer where separate calculations of the scattered power incident on the detector array are to be made, with the results added to obtain the total scattered power. In regions C and D, two beams are present, called 1 and 0, standing respectively for the diffracted (1st-order) and undiffracted (0-order) beams obtained after passage of the guided beam through the surface acoustic wave that divides regions B and C of the IOSA. The scattering contribution from each of these beams must be considered separately, so there are a total of six different scattered powers to be added to obtain the total scattered power at the various elements of the IOSA detector array. We refer to these powers as P_i, where the subscript i

6
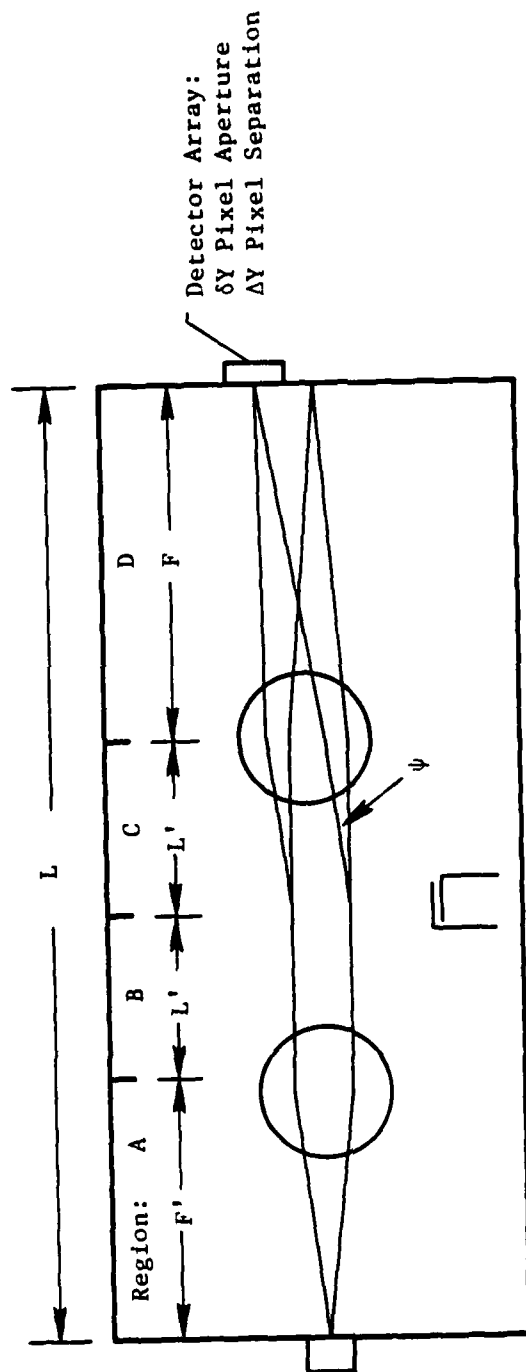
Figure 1. Geometry of IOSA used to calculate scattering
limitations to dynamic range.

7

TABLE I. PARAMETERS AND PARAMETER VALUES USED IN
IOSA DYNAMIC RANGE ANALYSIS

Parameter	Description	Numerical Values
L	length of waveguide	72.4 mm
F'	collimating lens focal length	27.2 mm
L'	lens-SAW separation	9 mm
F	Fourier-transform lens focal length	27.2 mm
ψ	AO diffraction angle	0.066 radians
η	AO diffraction efficiency	5%
δy	pixel width	12 μm
Δy	pixel spacing	12 μm
n	mode index	2.2
λ_o	free-space wavelength	0.83 μm
k	$2\pi n/\lambda_o$, wave vector magnitude	16.65 μm^{-1}
a	scattering center size	various
$\sigma(0)$	peak differential scattering cross section	various
Σ	scattering center surface density	various

is AO, BO, CO, Cl, DO, or Dl, depending on the region and the beam that generates the scattering. Some simplification of the calculation is afforded by the fact that subscripts AO, DO, and Dl are associated with cylindrical waves, while BO, CO, Cl are associated with plane waves. We consider the scattering from these first.

Scattered Power from Plane-Wave Portions of the Guided Beam

For power scattered from plane waves into an angular sector $\Delta\phi$ located at ϕ, the Fourier-transform lens in Fig. 1 will deliver the power to a location removed from the beam axis in the plane of the detector array by a distance $F\phi$. The power will be distributed over a width $F\Delta\phi$. We will define the transverse coordinate in the array plane to be Y, where $Y = 0$ is located at the central element in the detector array. If each element has a width δY, the subtended scattering angle is $\Delta\phi = \delta Y/F$. For the diffracted beam Cl, the actual scattering angle is $\phi = Y/F$. The scattered power received by the detector located at Y is therefore

$$\Delta P_{C1}(Y) = P_{C1} \ \Sigma L' \ \sigma(Y/F)(\delta Y/F), \tag{5}$$

where L' is defined in Fig. 1 as the distance of the acoustic wave center from the center of the Fourier-transform lens. P_{C1} is the unscattered power in the diffracted beam in region C. If we set $P_{C1} = P$ and, in general, define P_i as the unscattered power for all of the beams in the IOSA, where $i = $ AO, BO, CO, Cl, DO, and Dl, the relation between the six values of P_i and P is determined from the acoustic-wave diffraction efficiency η as follows:

$$P_{AO} = P_{BO} = P/\eta \ ,$$

$$P_{C1} = P_{D1} = P \ , \tag{6}$$

$$P_{CO} = P_{DO} = (P/\eta)(1-\eta).$$

9

This treatment ignores guided-wave attenuation associated with out-of-plane scattering or absorption.

To calculate the scattered power from the undiffracted beam in region C, we use the third of these relationships along with the fact that the undiffracted guided beam propagates at an angle ψ relative to the optical axis defined by the direction of the diffracted beam. As a result light which impinges at a position Y in the detector plane is scattered through an angle $\approx \psi - Y/F$. The scattered power received at a detector centered at Y and associated with beam C0 is therefore

$$\Delta P_{CO}(Y) = (P/\eta)(1-\eta)\Sigma L'\sigma(\psi-Y/F)(\delta Y/F) \tag{7}$$

The scattered power from the collimated beam incident on the acoustic wave is similarly given by

$$\Delta P_{BO} = (P/\eta)\Sigma L'\sigma(\psi-Y/F)(\delta Y/F). \tag{8}$$

The total scattered power from the collimated beam between the two lenses of the IOSA is the sum of Eqs. (5), (7), and (8). Referring to this scattered power as ΔP_{BC}, we find

$$\Delta P_{BC}(Y) = P\Sigma L'(\delta Y/F) \; [\sigma(Y/F) + (2/\eta-1)\sigma(\psi-Y/F)]. \tag{9}$$

Scattered Power From Cylindrical-Wave Portions Of The Guided Beam

The analysis is more complicated for beams in regions A and D, where the wavefront is cylindrical rather than planar. (The reader will have noted that we are considering each geodesic lens to act as would a thin lens located at the geodesic lens center). Consider first the scattered power contributed by the diffracted beam D1. Figure 2 shows a scattering event at a distance z from the array at an off-axis position y. Integrating the contributions from all distances z and positions y, we find the scattered power distributed over a detector element centered at Y to be

10
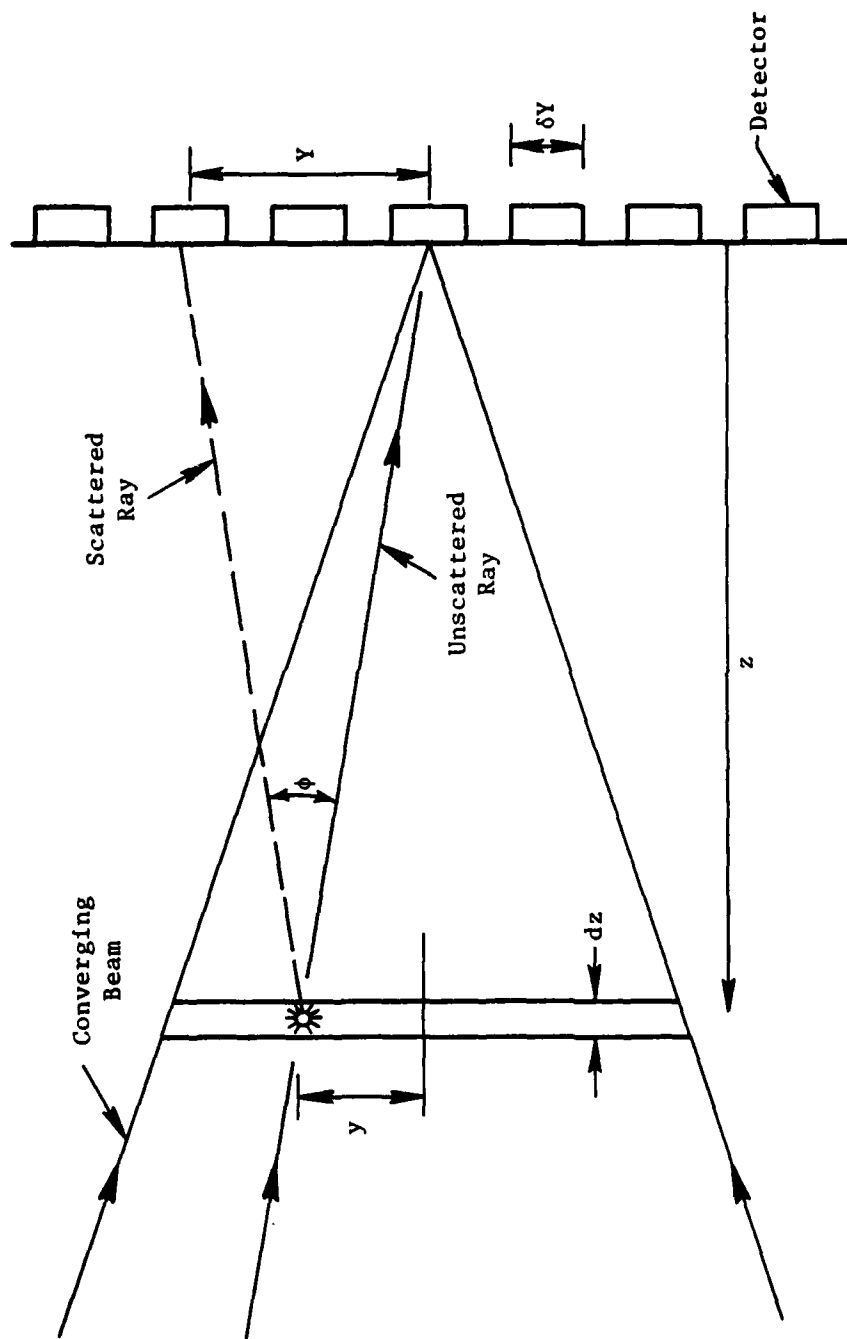
Figure 2. Geometry for analyzing scattering events that occur in the converging beam.

11

$$\Delta P_{D1} (Y) = \Sigma \int_{0}^{F} dz \int_{-\infty}^{\infty} dy I(y,z) \int_{\phi_{-}(Y,y,z)}^{\phi_{+}(Y,y,z)} d\phi \, \sigma(\phi) \quad , \tag{10}$$

where the upper and lower limits of the last integrand are the extremal scattering angles subtended by the detector under consideration. For most values of y and z of interest, $\sigma(\phi)$ will not vary significantly as ϕ varies from ϕ_{-} to ϕ_{+}, and we can replace the last integral above by $\sigma(\bar{\phi})(\phi_{+}-\phi_{-})$, where $\bar{\phi}$ is the value of ϕ at the center of the detector element. From Fig. 2, we find

$$\bar{\phi} = \tan^{-1}[(Y-y)/z] + \tan^{-1}(y/z)$$

$$\phi_{+}-\phi_{-} = \tan^{-1}[(Y-y + \delta Y/2)/z] \tag{11}$$

$$- \tan^{-1}[(Y-y - \delta Y/2)/z]$$

Even this simplification is not enough to reduce Eq. (10) to a tractable integral. However we can do so without much additional loss of accuracy by setting y = 0 in Eq. (11). That is, we take the scattering angle $\bar{\phi}$ and the subtended angle $\phi_{+} - \phi_{-}$ to be independent of the off-axis location of the scattering event. This is a good approximation for converging beams subtending a low numerical aperture, as is usually the case in planar integrated optical applications. We find

$$\bar{\phi} \simeq \tan^{-1}(Y/z) \tag{12}$$

$$\phi_{+}-\phi_{-} \simeq \tan^{-1}[(Y + \delta Y/2)/z] - \tan^{-1}[(Y-\delta Y/2)/z]. \tag{13}$$

The subtended angle can be further simplified to

$$\phi_{+}-\phi_{-} \simeq 2\tan^{-1}\delta Y/2z \quad , \quad Y = 0 \tag{14}$$

$$\simeq \delta Y z/(z^2 + Y^2), \quad Y \neq 0$$

The first of these expressions is obtained directly by setting Y = 0 in Eq. (13). The second is obtained by rewriting the right hand side of Eq. (13) as $\tan^{-1}\delta Y z/(z^2 + Y^2 - \delta y^2/4)$, and then replacing the inverse-tangent function

12

by its argument. Furthermore, we eliminate the $\delta Y^2/4$ term in comparison to Y^2. Since $Y^2 = m^2 \delta y^2$ for the m th off-axis detector, where $m^2 > 1$, Y^2 is at least four times larger than the neglected term.

With these approximations, the scattered power from the diffracted beam in Region D is given by the integral

$$\Delta P_{D1}(Y) = \Sigma \int_0^F dz \int_{-\infty}^{\infty} dy I(y,z) \sigma(\tan^{-1} Y/z) \begin{Bmatrix} 2\tan^{-1}(\delta Y/2z) \\ \text{or} \\ \delta Y z/(z^2 + Y^2) \end{Bmatrix} , \qquad (15)$$

where the top (bottom) term in curly brackets is used when Y equals (does not equal) zero, and where the functional form of σ is that of either Eq. (3) or (4), depending on the type of scattering that dominates. The integral over y is readily evaluated to give the power in the optical beam. For the diffracted beam in region D,

$$P_{D1} = P = \int_{-\infty}^{\infty} dy \ I(y,z). \qquad (16)$$

If the waveguide is lossless, as we assume, P is independent of z because energy is conserved at each distance along the beam axis. For lossy waveguides, attenuation mechanisms effect scattered and unscattered light similarly. Since dynamic range is calculated as the ratio of scattered to unscattered power, the effects of losses are largely self-cancelling. This shows, in a qualitative way, the appropriateness of neglecting waveguide attenuation. After inserting Eq. (16) into Eq. (10), and incorporating Eqs. (3) and (4) for the various forms of the scattering cross section, we may write Eq. (15) as

$$\Delta P_{D1}(Y) \simeq P\Sigma\sigma(0) \int_0^F dz \begin{Bmatrix} [1 + k^2 a^2(\tan^{-1}Y/z)^2]^{-1} \\ z^2/(z^2 + Y^2) \\ 1 \end{Bmatrix} \begin{Bmatrix} 2\tan^{-1}(\delta Y/2z) \\ \delta Y z/(z^2 + Y^2) \end{Bmatrix} \qquad (17)$$

This is really six different equations, one for each combination of terms in the two sets of curly brackets. The three different functions in the first set of curly brackets are associated with the type of scattering center (RS

13

or RGDS) and the polarization of guided light employed (TE or TM, but TE in
the IOSA application). The second set of curly brackets contains the approxi-
mate angle subtended by the detector element centered at Y. For the on-axis
detector at Y = 0, the top term in the second set of curly brackets applies,
and the first set of curly brackets contains only unity. The integral over
the inverse tangent function can be carried out exactly. The result is

$$\Delta P_{D1}(0) \simeq P\Sigma\sigma(o)\delta Y [u \tan^{-1}(1/u) + \ell n(1 + u^2)^{1/2}], \tag{18}$$

where $u = 2F/\delta Y$. With F typically several centimeters and Y typically ten
microns, u is on the order of 10^4. For this large value, Eq. (18) simplifies
further to

$$\Delta P_{D1}(0) \simeq P\Sigma\sigma(0)\delta Y \ \ell n 2F/\delta Y \tag{19}$$

For nonzero values of Y, Eq. (17) consists of three different in-
tegrals for the three different expressions in the first set of curly brackets
multiplied by $\delta yz/(z^2 + Y^2)$. The two integrals for Rayleigh scattering can
be calculated analytically, as can the integral for RGD scattering if we re-
place $\tan^{-1} Y/z$ by Y/z in the first set of curly brackets. This approxima-
tion is invalid at small z; however, the integrand vanishes at z = 0 whether
or not the approximation is employed. Consequently, there is not likely to
be a significant error in the integral as a result.

The values for the three integrals are displayed in Table II. In
two of the three expressions there is a second term that is generally small
in comparison to the first. If we ignore this term in Table II, the three ex-
pressions acquire the same form; namely

$$\Delta P_{D1}(Y) \simeq P\Sigma\sigma(0)\delta Y \ \ell n[(F^2 + q^2Y^2)/q^2Y^2]^{1/2} \ , \tag{20}$$

where $q = ka \gg 1$ in the case of RGD scattering and q = 1 in the case of Rayleigh
scattering, independent of the polarization of light in the waveguide. The
expression of Eq. (20) diverges as Y→0. However, we know that Eq. (19) should
be used instead of Eq. (20) as this limit is approached. It is useful to

14

TABLE II.   SCATTERED POWER FROM THE DIFFRACTED BEAM IN
REGION D, FOR DETECTOR ELEMENTS LOCATED OFF-
AXIS AT A DISTANCE Y

Type of Scattering	Differential Scattering Cross Section	$\Delta P_{D1}(Y)/P\Sigma\sigma(0)\delta Y$
Rayleigh Gans Debye	$\sigma(0)\,[1 + k^2a^2\phi^2]^{-1}$	$[k^2a^2/(k^2a^2-1)]\ln[(F^2+k^2a^2Y^2)/k^2a^2Y^2]^{1/2}$ $-[1/(k^2a^2-1)]\ln[(F^2+Y^2)/Y^2]^{1/2}$
Rayleigh (TE polarization)	$\sigma(0)\,\cos^2\phi$	$\ln[(F^2 + Y^2)/Y^2)]^{1/2} - (1/2)F^2/(F^2+Y^2)$
Rayleigh (TM polarization)	$\sigma(0)$	$\ln[(F^2 + Y^2)/Y^2]^{1/2}$

phenomenologically combine the two results by replacing q^2Y^2 in the denominator of Eq. (20) by $q^2Y^2 + \delta y^2/4$. The added term removes the divergence at $Y = 0$ and provides the correct expression as that limit is approached. At the same time, it does not produce a significant error at nonzero values of Y of interest, namely $Y = m\delta y$, where $m = \pm1, \pm2, \pm3...\pm M$ is the number of the detector element in the array relative to the on-axis detector element, having $m = 0$. In summary the scattered power at detector m from the diffracted beam in region D is approximately given by

$$\Delta P_{D1}(m) = P\Sigma\sigma(0)\delta Y \ell n[(F^2 + q^2 m^2\delta Y^2)/(\delta Y^2/4 + q^2 m^2\delta Y^2)]^{1/2}. \tag{21}$$

The scattered power from the undiffracted beam in region D is obtained from this expression by replacing m by $F\tan\psi/\delta y - m = m_0 - m$. This accounts for the propagation of the undiffracted beam at an angle ψ relative to the propagation direction of the diffracted beam. We also replace P by $(P/\eta)(1-\eta)$ to account for the power variation in the diffracted and undiffracted beams. The result is

$$\Delta P_{D0}(m) = (P/\eta)(1-\eta)\Sigma\sigma(0)\delta Y \ \ell n\{[F^2 + q^2(m_0-m)^2\delta Y^2]$$

$$/[\delta Y^2/4 + q^2(m_0-m)^2\delta Y^2]\}^{1/2} \tag{22}$$

The undiffracted beam in region A is also accounted for by an expression of this type. This is not immediately obvious because the scattering in this region is produced by a diverging rather than a converging beam. However one effect of the collimating and Fourier-transform lenses in the IOSA device is to produce in the detector plane an image of the light pattern in the laser plane. The effect of scattering centers in region I is to produce cylindrical wavefronts that may be regarded as emanating from virtual sources in the laser plane. The distribution of the virtual intensity associated with these sources is calculated by propagating the scattered wavefronts backward through the scattering centers to the laser plane. The virtual image that results from the scattering of a diverging spherical wave is therefore identical to the real image that results from the scattering of a converging beam. The IOSA collimating and Fourier-transform lenses, in producing a real image

of the virtual wavefront in the laser plane, simply replicate the scattered-intensity distribution from the undiffracted beam in Region D. The only difference is that associated with the variation of optical power in the two regions. We have

$$\Delta P_{AO}(m) = P_{DO}(m)/(1-\eta). \tag{23}$$

The Dynamic-Range Formula

The total scattered power at detector m is obtained by adding the results of Eqs. (9), (21), (22), and (23). Neglecting polarization corrections Eq. (9) can be written in the form

$$\Delta P_{BC}(m) = P\Sigma L'(\delta Y/F)\sigma(0) \tag{24}$$

$$\{[1 + q'^2 m^2 \delta Y^2/F^2]^{-1} + (2/\eta-1)\ [1 + q'^2(m_o-m)^2\delta Y^2/F^2]^{-1}\}$$

where $q' = 0$ for Rayleigh scattering, and $q' = ka$ for RGD scattering. The geometry of the IOSA is such that the coefficients of q'^2 are much smaller than unity for all detectors m. Consequently, not much error is made by replacing q' by q in Eq. (24), where $q = ka$ for RGD scattering and $q = 1$ for Rayleigh scattering. This enables us to write the total scattered power in a unified form, valid for both Rayleigh and RGD scattering; namely,

$$\Delta P_{tot}(m)/P\Sigma\delta Y\sigma(0) =$$

$$(L'/F)\{[1+q^2m^2\delta Y^2/F^2]^{-1} + (2/\eta-1)\ [1+q^2(m_o-m)^2\delta Y^2/F^2]^{-1}\}$$

$$+\ln[(1+q^2m^2\delta Y^2/F^2)/(q^2m^2\delta Y^2/F^2 + \delta Y^2/4F^2)]^{1/2} \tag{25}$$

$$+(2/\eta-1)\ln\{[1+q^2(m_o-m)^2\delta Y^2/F^2]/[q^2(m_o-m)^2\delta Y^2/F^2 + \delta Y^2/4F^2]\}^{1/2}$$

17

The top term on the right hand side is the contribution from the plane waves in regions B and C, the second term is the contribution from the focused diffracted wave in region D, and the third term is the contribution from the undiffracted cylindrical waves in regions A and D.

The only parameter in Eq. (25) that relates to the type of scattering mechanism is q, where $q = 1$ for Rayleigh scattering, and $q = ka$ for RGD scattering. For these two cases at least, q varies approximately as the inverse of the scattering angle. We will assume that this situation holds for the general case of Mie scattering. That will enable us to apply Eq. (24) to any scattering mechanism by suitably choosing an appropriate value of q.

Table III shows the design parameters for an IOSA similar to the one reported by Mergerian et al.[4] Using these parameters we can calculate the relative values of the three contributions to the scattered power in Eq. (25) as a function of q, taking $m = 4$. This choice of m is made because IOSA specifications require the achievement of 40 dB dynamic range or better at the 4th off-axis pixel.

TABLE III. DESIGN PARAMETERS FOR AN IOSA

Lens Focal Lengths	F	27.2 mm
Lens-Lens Separation	L	18.0 mm
Detector Aperture and Spacing	δY	12.0 μm
Diffraction Angle	ψ	0.066 radians
Diffraction Efficiency	η	5%
Free Space Optical Wavelength	λ_o	0.83 μm
Refractive Index	n	2.2

The results of the calculation are shown in Fig. 3. At small values of q, the dominant contribution comes from the undiffracted beam in regions A and D, labeled I in Fig. 3. The power in this beam is about 20 times larger than in the diffracted beam, resulting in greater scattered power. Additionally small values of q are associated with large scattering angles, so that a significant portion of scattered light can reach the detector array.

For large values of q, the scattering angles are small and light from the undiffracted beam does not reach the detector array. In this case
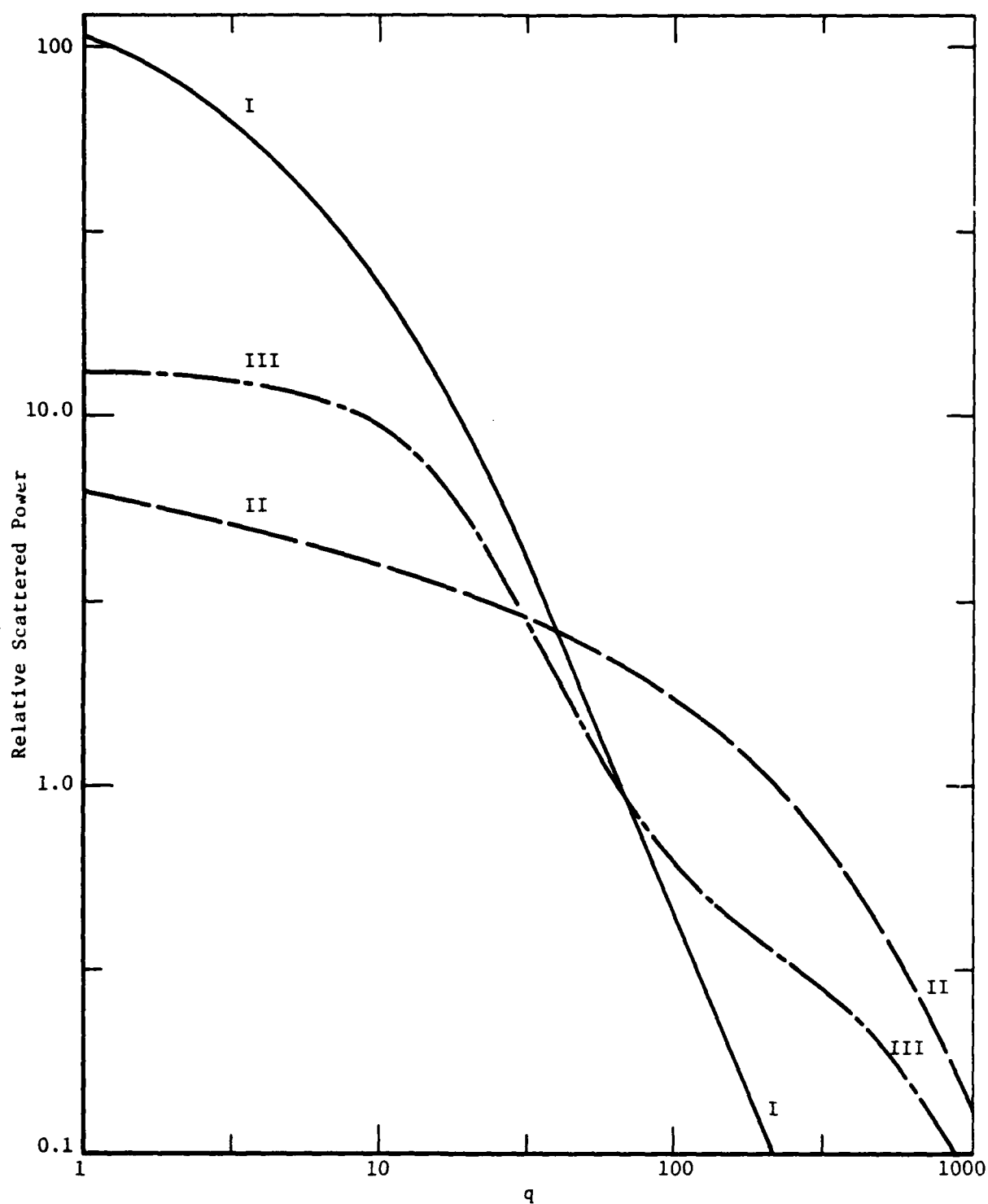
Figure 3.   Relative scattered power at the fourth pixel vs q.
I: contribution from the undiffracted beam in regions
A and D.   II: contribution from the diffracted beam
in region D.   III: contribution from the plane waves
in regions B and C.

19

the dominant contribution to scattering-generated noise is the focused-diffracted beam in region D, labeled II in Fig. 3. The plane wave contribution from regions B and C of the IOSA is labeled III in Fig. 3 and is intermediate to the other contributions at most values of q.

IOSA dynamic range is computed from the ratio of scattered power captured by the 4th detector element to the total power captured by the on-axis detector. Because the detector elements in the IOSA array are large compared to the focal spot size of the beam, the power illuminating the on-axis detector is essentially P. The corresponding dynamic range is $10 \log[\Delta P_{tot}(4)/P]$. This may be calculated from Eq. (25) when the values of $\Sigma\sigma(0)$ and q are specified. The use of Eq. (25), although it is an approximation, is expected to provide a level of accuracy commensurate with the accuracy of the measurements used to obtain the scattering parameters. Furthermore the equation is simple enough to program on most common programmable hand calculators.

CALCULATIONS OF SCATTERING CROSS SECTIONS AND DYNAMIC-RANGE PERFORMANCE FOR VARIOUS TYPES OF SCATTERING CENTERS

While values of $\Sigma\sigma(0)$ and q are measured experimentally, it is useful to calculate the dependence of $\sigma(0)$ on the size and refractive-index inhomogeneity of the scattering center. This facilitates the use of the data to draw conclusions about the source of the scattering. We consider three different situations: (1) Rayleigh Scattering (RS) from particles of characteristic size a small compared to the wavelength ($a<<\lambda$), and real index of refraction different from that of the immediate environment by δn; (2) Rayleigh Gans Debye Scattering (RGDS) from particles large compared to the wavelength ($a>>\lambda$) and refractive index such that $\delta n k a<<1$; (3) Mie Scattering (MS), for all other situations. The analyses employed to calculate $\sigma(0)$ in terms of δn and a are not rigorous but are supported by attractive physical arguments. Our objective is to obtain the correct dependences on the parameters involved without concern for exact numerical factors or for unnecessary complications associated with the waveguide geometry.

The Case of Rayleigh Scattering

Figure 4 shows a schematic drawing of Rayleigh (dipole) scattering centers distributed throughout a waveguide layer of depth D. If we ignore the effects introduced by the waveguide geometry, the differential scattering cross section is[5]

$$\sigma'(\alpha) = [k^4 a^6 (m^2-1)^2/(m^2+2)^2]\cos^2\alpha, \tag{26}$$

where $\pi/2-\alpha$ is the angle between the scattering direction and the incident polarization, and $m = 1 + \delta n/n$. The terms containing m may be replaced by the approximation $(4/9)\delta n^2/n^2$. While this approximation is obtained in the limit of small δn, it is fairly accurate even when the scattering centers are voids having $n + \delta n = 1.0$ and, for the example of $LiNbO_3$, $n = 2.2$. The angle α in Eq. (26) is the same as the scattering angle ϕ for TE polarized light scattered in the plane of the waveguide, while $\alpha = 0$ for TM polarized light scattered in plane. This has been used in writing Eq. (4); however, $\sigma(0)$ of Eq. (4) can not be identified with the coefficient $\sigma'(0)$ of $\cos^2\alpha$ in Eq. (26). The latter coefficient is associated with scattering into a solid angle $\Delta\Omega$ in three dimensional space, while $\sigma(0)$ is associated with scattering into an angular sector $\Delta\phi$ in the plane of the waveguide.

The relation between the two cross sections can be obtained by deriving the power scattered into a waveguide detector by two equivalent methods, one utilizing the in-plane cross section $\sigma(\phi)$ and the other utilizing the three-dimensional cross section $\sigma'(\alpha)$. For the former, the intercepted power is given by Eq. (1). For the latter, the intercepted power generated from a single scattering center is

$$\Delta P = \mathcal{I}\sigma'(\alpha)\Delta\Omega \quad , \tag{27}$$

where $\mathcal{I}$ is the power-per-unit-area illuminating the scattering center and $\Delta\Omega$ is the effective solid angle subtended by the detector. For a guided-wave power-per-unit width I and a confinement depth D, $\mathcal{I} \simeq I/D$. In calculating the effective solid angle subtended by a detector, $\Delta\Omega$, we consider
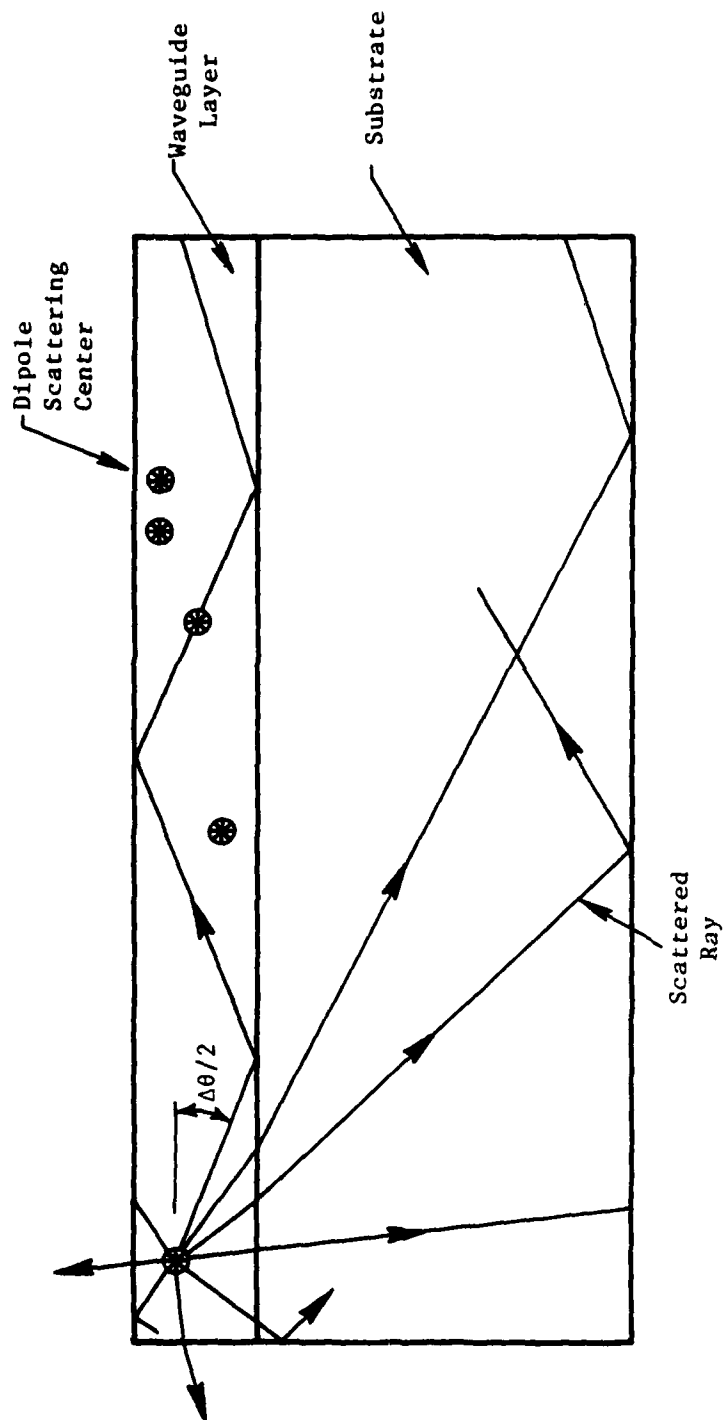
Figure 4. Schematic drawing of dipole scattering centers confined to the waveguide layer. $\Delta\theta$ = full acceptance angle of the waveguide.

22

only scattered rays which are bounded in-plane by the detector aperture $\Delta\phi$ and which are simultaneously trapped in the waveguide. Trapped rays are generated from those scattered within the acceptance angle of the waveguide, $\Delta\theta$. This angle is identified in Fig. 4, and is found, using Snell's Law, to be

$$\Delta\theta \simeq 2(2\Delta n/n)^{1/2} \quad , \tag{28}$$

where Δn is the index change associated with the waveguide layer and $n \gg \Delta n$ is the substrate index. The effective solid angle subtended by the waveguide detector elements is $f\Delta\phi\Delta\theta$. The factor f is added to describe the fact that only a fraction of rays scattered within the acceptance angle of the waveguide are trapped within waveguide modes.

Using these results in Eq. (27), we find the detected power to be

$$\Delta P = (I/D) \; \sigma'(\alpha) \quad 2f(2\Delta n/n)^{1/2}\Delta\phi \quad . \tag{29}$$

For power scattered in the plane of the waveguide, $\sigma'(\alpha)$ is replaced by either $\sigma'(0)\cos^2\phi$ or $\sigma'(0)$, depending on whether the guided-wave modes are TE or TM. By comparison of this result with Eqs. (1) and (4), we make the identification

$$\sigma(0) = \sigma'(0) \; (2f/D)(2\Delta n/n)^{1/2} \tag{30}$$

This expression has the correct dimension of $[\text{length}]^1$.

The dynamic range depends on the product $\Sigma\sigma(0)$, where Σ is the number of scattering centers per unit area. If ρ is the volume density of scatterers in the waveguide, then $\Sigma = \rho D$ and

$$\Sigma\sigma(0) = \rho\sigma'(0) \; (2f) \; (2\Delta n/n)^{1/2} \quad . \tag{31}$$

It is further useful to note that

$$\sigma'(0) = (3/8\pi)\sigma_{tot} \quad , \tag{32}$$

where σ_{tot} is the total scattering cross section obtained by integrating $\sigma'(\alpha)$ over all solid angles.[5]   Substituting this result into Eq. (31), we obtain

$$\Sigma\sigma(0) = (\rho\sigma_{tot})(3/8\pi)(2f)(2\Delta n/n)^{1/2} \ . \tag{33}$$

Since only a small fraction of all scattered rays are retrapped in guided modes, $\rho\sigma_{tot}$ may be identified with the waveguide attenuation coefficient associated with out-of-plane scattering. This is the total attenuation co-efficient in waveguides for which absorption is negligible, and for which Rayleigh scattering centers dominate. Assuming this to be the case for Ti-diffused LiNbO$_3$ waveguides used in IOSA development, Eq. (33) gives us the capability of calculating IOSA dynamic range performance once the attenuation coefficient is known. Figure 5 shows the results of such a calculation for the case $f = 1/2$ and $\Delta n = 0.01$. The IOSA dynamic range specification of 40 dB at the fourth pixel is achieved if the attenuation coefficient is less than 0.25 dB/cm. This level of attenuation should be readily attained in Ti:LiNbO$_3$ waveguides.[6]   Consequently Rayleigh scattering from small inhomogeneities should not be an important factor limiting IOSA dynamic-range performance in systems that employ Ti:LiNbO$_3$ waveguides.

The Case of Rayleigh-Gans-Debye Scattering

We now consider scattering centers that are much larger than a wave-length, but which are optically soft. By this we mean that the field inside the scattering center is essentially the same as the incident field, and the effect of the scattering center is simply to perturb the wavefront of the incident light by an amount small compared to a wavelength. These require-ments are satisfied when $q = ka \gg 1$, and $ka\delta n \ll 1$, where δn is the index per-turbation associated with the scattering center.

Figure 6 defines the geometry of the problem under consideration. If $A_o\exp(ikz)$ is the unperturbed wavefront, the wavefront after passing through the scattering center is $A_o\exp(ikz) + A_{pert}$, where A_{pert} is the perturbed field. If the scattering center has a characteristic size a, then the perturbed field just beyond the scattering center is
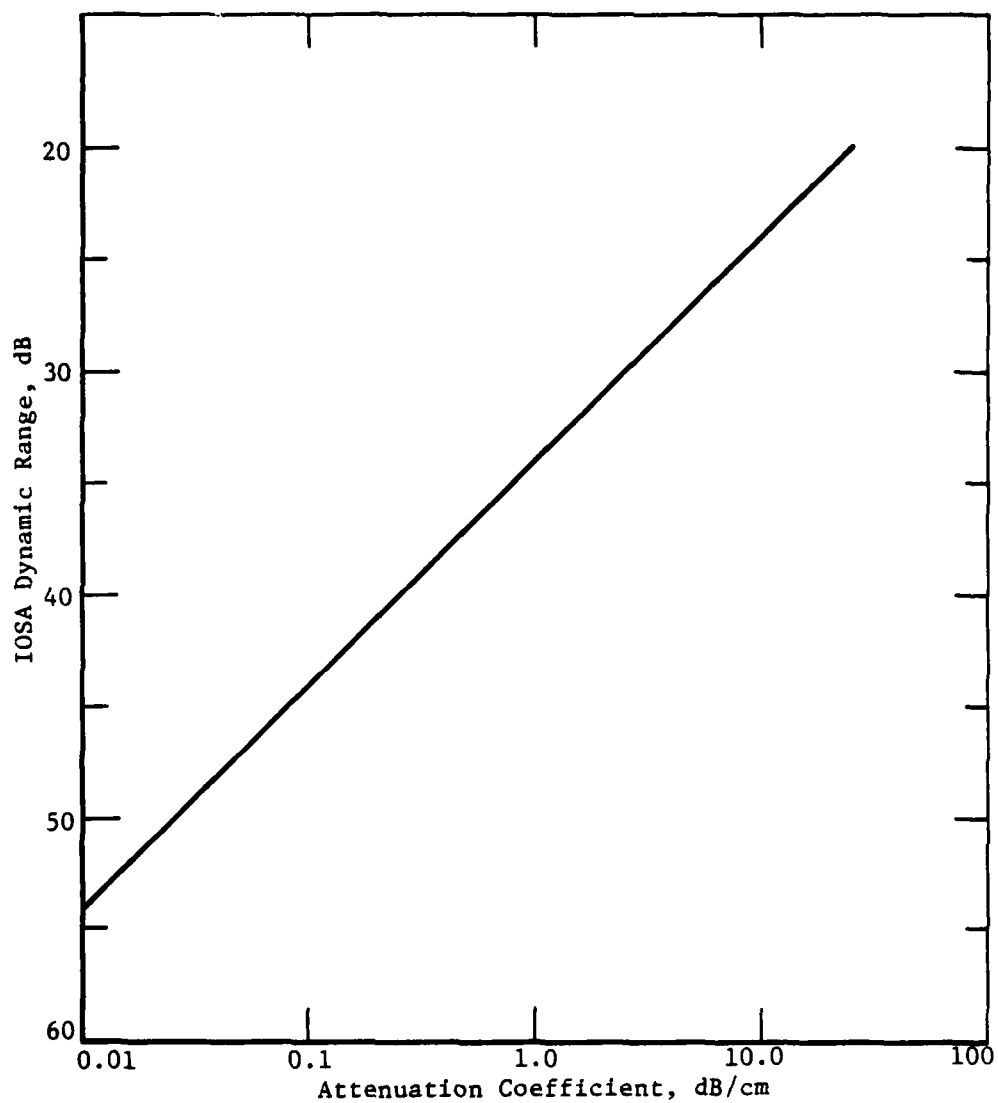
24

Figure 5.   IOSA dynamic range versus waveguide attenuation
            coefficient for the case of Rayleigh scattering
            centers.
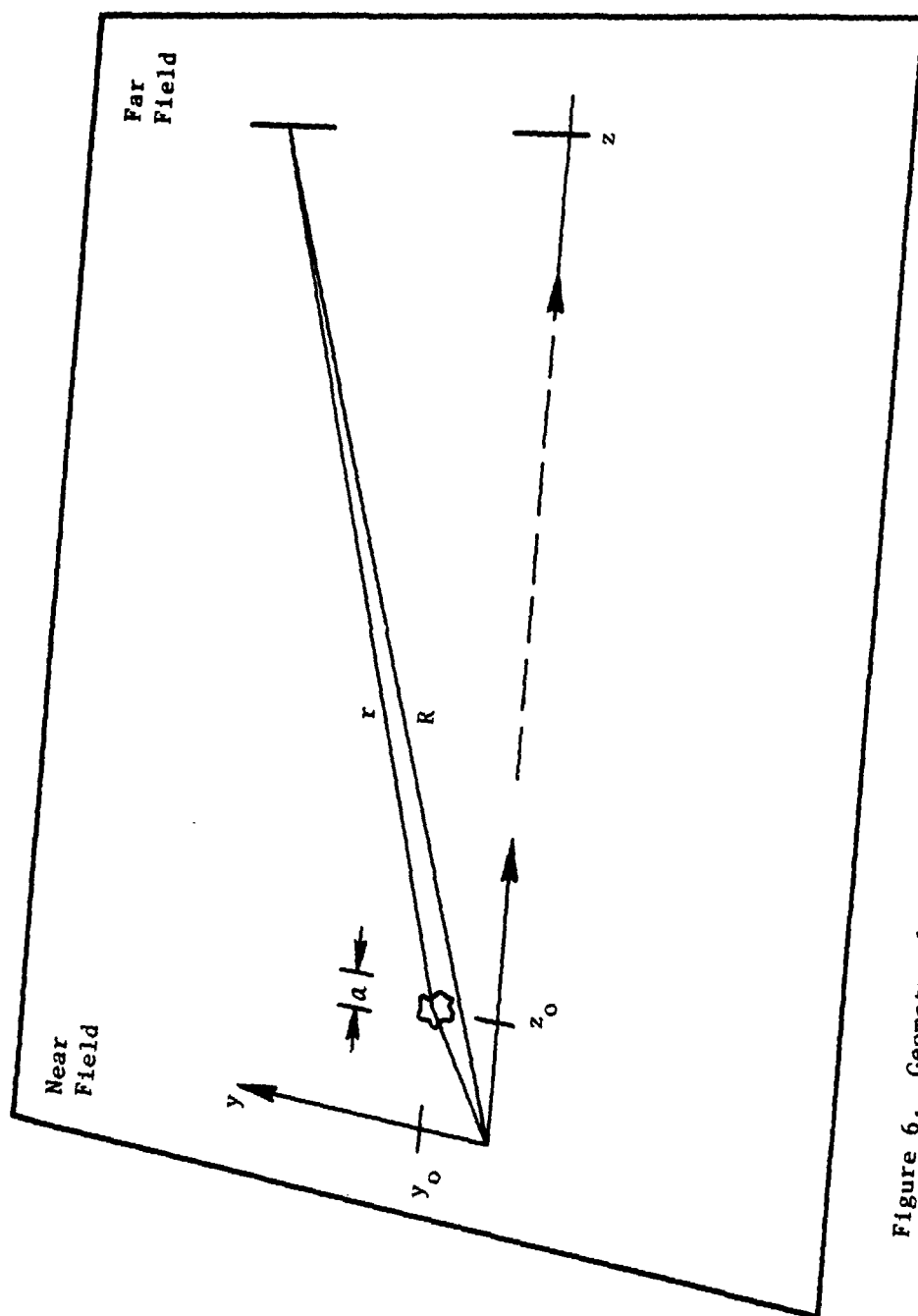
Figure 6. Geometry for calculating the field produced by an RGD scattering center.

$$A_{pert} \simeq ik_o a\delta n_g \, A_o exp[ik(z_o + a/2)], \text{ in } y_o - a/2 \le y \le y_o + a/2$$

$$\simeq 0, \text{ elsewhere} \qquad (34)$$

In our notation $k = k_o n_g$, where $k_o = 2\pi/\lambda_o$, λ_o is the free space wavelength, n_g is the mode index of the guided wave, and δn_g is the change in mode index associated with the material index perturbation δn. Equation (34) is derived for a square-shaped inhomogeneity to simplify the analysis without sacrificing its important features. The coordinate pair (y_o, z_o) describes the center of the scattering site.

In the near zone, the perturbed field of Eq. (34) propagates as a plane wave, but in the far zone, diffraction causes the wavefronts to become circles centered at (y_o, z_o). The form of the perturbed field in the far zone is found from a straightforward application of Fraunhofer diffraction theory to be [7]

$$A(R,\phi) = A_o e^{ikR} (i\lambda z)^{1/2} ik_o a^2 \delta n_g sinc(a\phi/\lambda)$$

$$e^{-iky_o sin\phi + ikz_o(1-cos\phi)}, \qquad (35)$$

where R is the radial distance from the scatterer, z is the distance along the axis of propagation, and ϕ is the angle of observation relative to the direction of the unperturbed beam.

For an ensemble of N scattering centers the total scattered field is the sum of N expressions like that of Eq. (35). These expressions are identical except for the replacement of (y_o, z_o) by (y_i, z_i), the center co-ordinates of the ith scattering site. The result of squaring the magnitude of the total scattered field is a randomly fluctuating intensity distribution commonly referred to as a speckle pattern. Because the longitudinal dis-tances between the scattering centers can exceed many wavelengths, the speckle pattern is a high-contrast pattern with intensity minima near zero and inten-sity maxima which can be several times larger than the average intensity.[8] The average intensity is the same as would be calculated by summing the intensi-ties of the light scattered from individual scattering sites, and is

$$I_{scat} = I_o N(k_o a^2 \delta n_g)^2 (\lambda z)^{-1} sinc^2(a\phi/\lambda). \qquad (36)$$

27

The angular variation of the scattered intensity with ϕ is contained in the $\text{sinc}^2(a\phi/\lambda)$ term. However this function itself has structure that results from our unphysical assumption of square scattering centers of uniform size. Following a more general statistical analysis by Marcuse,[3] the formula

$$I_{scat} = 4I_o N(k_o a^2 \delta n_g)(\lambda z)^{-1} L(ka\phi),$$

(37)

$$L(ka\phi) = [1 + (ka\phi)^2]^{-1}$$

is derived. Using this formula, the scattered power received at a detector of width δY from a remote scattering area of length L and width W is $\Delta P = I_{scat}\delta Y$, or

$$\Delta P = P\Sigma L 4(k_o a^2 \delta n_g)^2 \lambda^{-1} \Delta\phi L(ka\phi)$$

(38)

We have used $N = \Sigma LW$, $P = I_o W$ and $\Delta\phi = (\delta Y/z)$ to facilitate comparison of this result with Eq. (2). The comparison enables us to identify the differential scattering cross section for RGD scattering as

$$\sigma(\phi) = (2/\pi) \, n_g k_o^3 a^4 \delta n_g^2 L(ka\phi).$$

(39)

This is of the form given in Eq. (3), with $\sigma(0) = (2/\pi)n_g k_o^3 a^4 \delta n_g^2$.

IOSA dynamic range depends on the product $\Sigma\sigma(0)$. The worst case situation is that of contiguous scattering centers, for which $\Sigma = 1/a^2$, and

$$\Sigma\sigma(0) = (2/\pi)n_g k_o^3 a^2 \delta n_g^2 \quad .$$

(40)

Figure 7 shows the functional relationship between a and δn_g that will result in an IOSA dynamic range of 40 dB. For scattering centers between 1 and 100 μm in size, δn_g values in the range from 10^{-5} to 2×10^{-6}, or smaller, are indicated. The scattering index inhomogeneity δn, in other words, should perturb the guided wave mode index by an amount three-to-four orders of magnitude less than the waveguide index change Δn. Just what values of δn can be tolerated depends on the depth of the scattering center beneath the waveguide surface, its thickness measured normal to the surface, and the
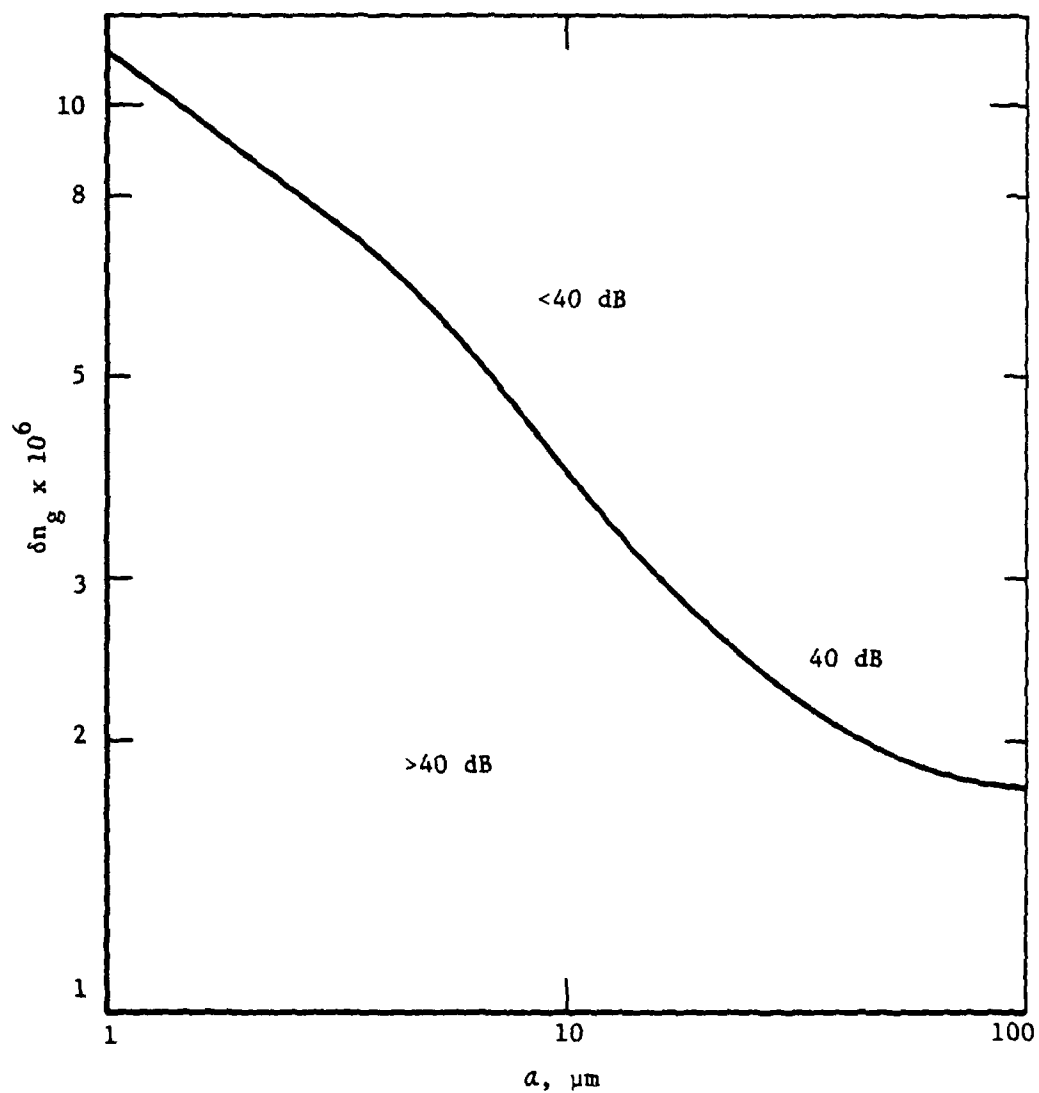
Figure 7. Relation between δn_g and a consistent with an
IOSA dynamic range of 40 dB.

modal structure of the guided wave. Thus a separate analysis is required for each different scattering mechanism. The dependence on the waveguide modal parameters suggests the possibility of reducing in-plane scattering by appropriately modifying waveguide fabrication procedures which influence these parameters.

Calculation of δn_g in Terms of Scattering Parameters

The perturbed mode index depends on the actual index inhomogeneity associated with the scattering center, δn, and on the extent to which the scattering center experiences the modal field. An RGD scattering center may be characterized as having a characteristic size a measured in the plane of the waveguide and a characteristic thickness z_o measured normal to the wave-guide. If $z_o << D$, the thickness of the waveguide layer, the scattering center may be described as a surface scattering center. If $z_o \simeq a >> D$, it may be described as a volume scattering center. The former samples only the surface modal field, and may be reduced in importance by generating waveguides having a low surface field. The latter samples the entire mode, and may only be reduced in importance by reducing δn or the density of scattering centers, Σ.

These considerations are made quantitative by the approximate relationship

$$\delta n_g \simeq <E_o(z)|\delta n(z)|E_o(z)>/<E_o(z)|E_o(z)> \tag{41}$$

where $E_o(z)$ is the amplitude profile of the TE_o electric field, assumed to be employed in an IOSA. The refractive index is

$$\delta n(z) = \delta n \quad 0<z<z_o$$
$$= 0 \quad \text{elsewhere} \tag{42}$$

where $z = 0$ is the waveguide surface. Utilizing the forms for $E_o(z)$ derived by Marcuse for a strongly asymmetric step index waveguide having a small surface index change Δn and an air superstrate, we find for $z_o << D$,

$$\delta n_g = [4n/(n^2-1)] \, (k_o z_o \delta n) \, S(\Delta n_g)$$
$$S(\Delta n_g) = (\Delta n - \Delta n_g)(2n \, \Delta n_g)^{1/2} \, [1 + k_o D(2n \, \Delta n_g)^{1/2}]^{-1} \, . \tag{43}$$

30

In this result, S is a function proportional to the modal intensity at the surface. It uses the parameter $\Delta n_g = n_g - n$, where n is the substrate index. For the IOSA application, suitable waveguides are those for which Δn_g is small enough to preserve single-mode characteristics, yet large enough to reduce propagation losses associated with geodesic lens curvature.[9] We take as representative $n = 0.01$, $\Delta n_g = 0.003$, and $D = 2.15$. For a free space wavelength $\lambda_o = 0.83$ μm and $n = 2.2$, we find $S(\Delta n_g) = 2.80 \times 10^{-4}$. The mode index perturbation is then

$$\delta n_g = 6.42 \times 10^{-4} \, \delta n \, z_o \qquad (44)$$

where z_o is given in microns. To achieve $\delta n_g = 2 \times 10^{-6}$, a figure for which IOSA dynamic range is likely to be above 40 dB, we require $\delta n \cdot z_o = 3.11 \times 10^{-3}$ μm. In Section III we will estimate the importance of some real scattering mechanisms in view of this requirement.

Note that for $z_o > D$, Eq. (43) has the simple result

$$\delta n_g = \delta n \qquad (45)$$

In this case, the actual scattering center index inhomogeneity must be made less than 2×10^{-6} to achieve a high probability of attaining dynamic range values in excess of 40 dB.

The Case of Mie Scattering

For present purposes, Mie scattering is taken to describe scattering from index inhomogeneities much larger than a wavelength, and having values of δn large enough to justify the use of geometrical-optics principles in analyzing their scattering effects. If the typical radius of curvature of a Mie scattering center in the vicinity of the guided beam is a, an approximate application of the lens-makers formula suggests that the refracted beam will focus at a distance $R \simeq a/2\delta n$. At distances greater than R, the refracted beam diverges with a half angle $\theta \simeq \tan^{-1}(a/R) \simeq \tan^{-1} 2\delta n$.

Figure 8 shows a highly schematic representation of the event, in which the diverging beam is represented as a cone of light. The top portion
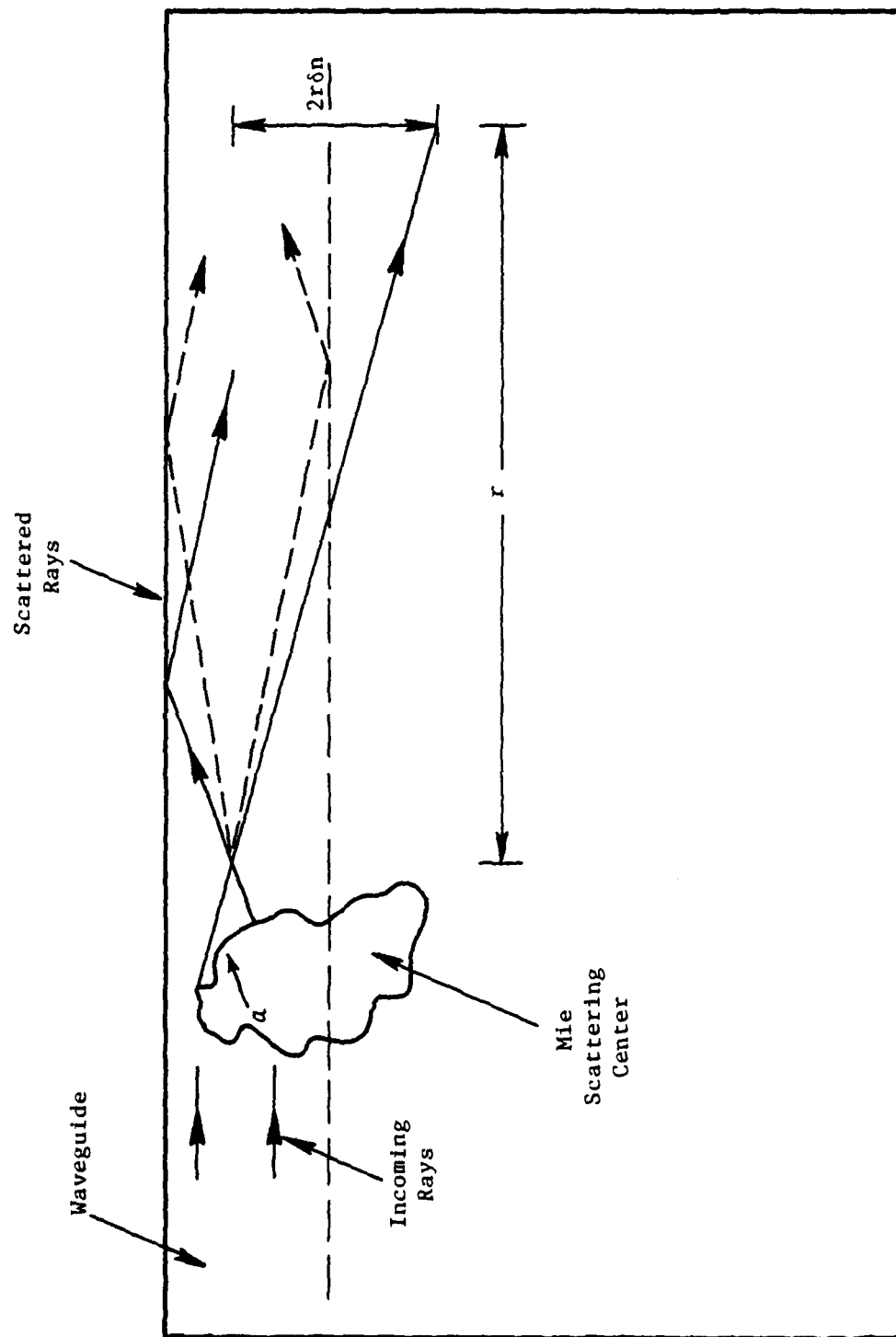
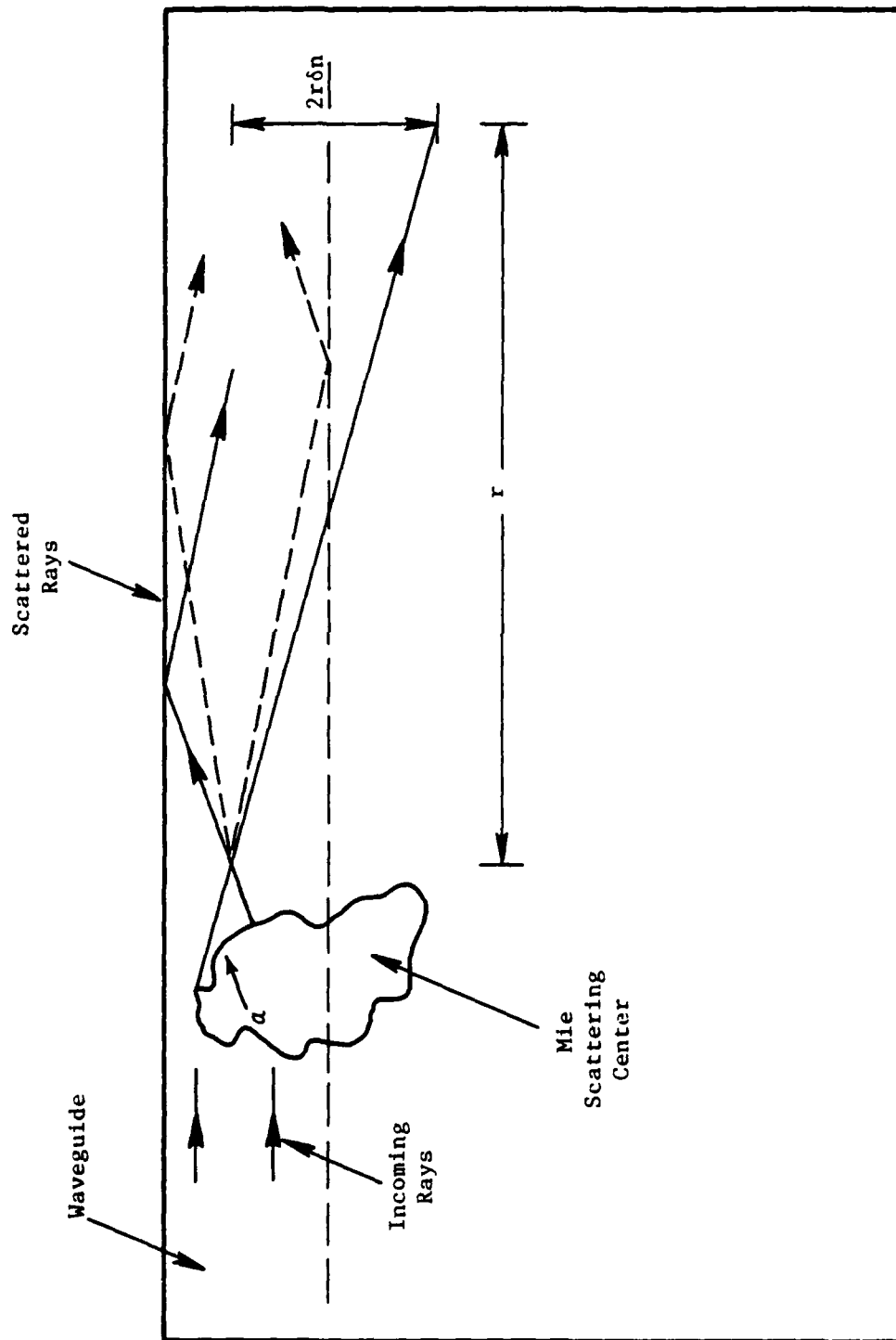Figure 8. Geometry for Mie Scattering.

Figure 8. Geometry for Mie Scattering.

of the light cone is reflected from the surface of the waveguide into the substrate, doubling the average intensity in that region. At a distance $r \gg R, a$ from the scattering center, the area subtended by the light cone is a semi-circle of radius $r \tan\theta \simeq 2r\delta n$. The area of the semicircle is $A = 2\pi r^2 \delta n^2$. If the power scattered by the imperfection is equal to the power intercepted by it, then $\Delta P \simeq Ia$, and the average power per unit area in the scattered beam is

$$\Delta P_{tot}/A = Ia/2\pi r^2 \delta n^2 \quad . \tag{46}$$

The effective area spanned by a waveguide detector at a distance r is $A' = r^2 \Delta\Omega$, where $\Delta\Omega$ is the effective solid angle given previously as $f\Delta\phi\Delta\theta$, where $\Delta\theta \simeq 2(2\Delta n/n)^{1/2}$ is the acceptance angle of the waveguide, and f is the fraction of light scattered within this angle that is trapped in waveguide modes (dashed rays in Fig. 8). As long as the detector is within the light cone, the power intercepted by it is $\Delta P = (\Delta P_{tot}/A)A'$, or

$$\Delta P = (1/2\pi) \, 2f(2\Delta n/n)^{1/2} \, (Ia/\delta n^2)\Delta\phi. \tag{47}$$

Outside the light cone, the intercepted power is zero. By comparison with Eq. (2) the differential scattering cross section is therefore

$$\sigma(\phi) = \Delta P/I\Delta\phi = (1/2\pi)(2\Delta n/n)^{1/2} \, (af/\delta n^2), \text{ in } -\tan^{-1} 2\delta n < \phi < \tan^{-1} 2\delta n$$

$$= 0, \qquad \text{elsewhere.} \tag{48}$$

Calculations of IOSA dynamic range require knowledge of $\Sigma\sigma(0)$ and q, where, as indicated earlier, q is correlated with the inverse of the scattering half angle. For the example of Mie scattering, we will take q to be the larger of unity or $1/\tan^{-1} 2\delta n$. Assuming that most of the scattered power from a single scattering event is lost to the waveguide, the total power lost in traversing a path length L is $\Delta P = \Sigma LWIa = \Sigma LaP$. The waveguide attenuation coefficient is therefore $\Delta P/PL = \alpha = \Sigma a$. We may write

$$\Sigma\sigma(0) = (1/2\pi) \, (2\Delta n/n)^{1/2} \, (\alpha f/\delta n^2). \tag{49}$$

33

Figure 9 shows IOSA dynamic range calculated from Eqs. (48) and (25) as a function of α with δn as a parameter. We have used $f = \frac{1}{2}$ and $\Delta n = 0.01$. Values of n less than 0.05 are not plotted because for these values the scattered light cone falls within the acceptance angle of the waveguide, and the assumption that most of the scattered light is lost to the waveguide may not be valid. Nevertheless, for plotted values of δn, we find that Mie scattering can be very deleterious to IOSA dynamic range. The criterion is that the scattering centers be present in sufficient numbers to produce attenuation levels on the order of 0.1 dB/cm.
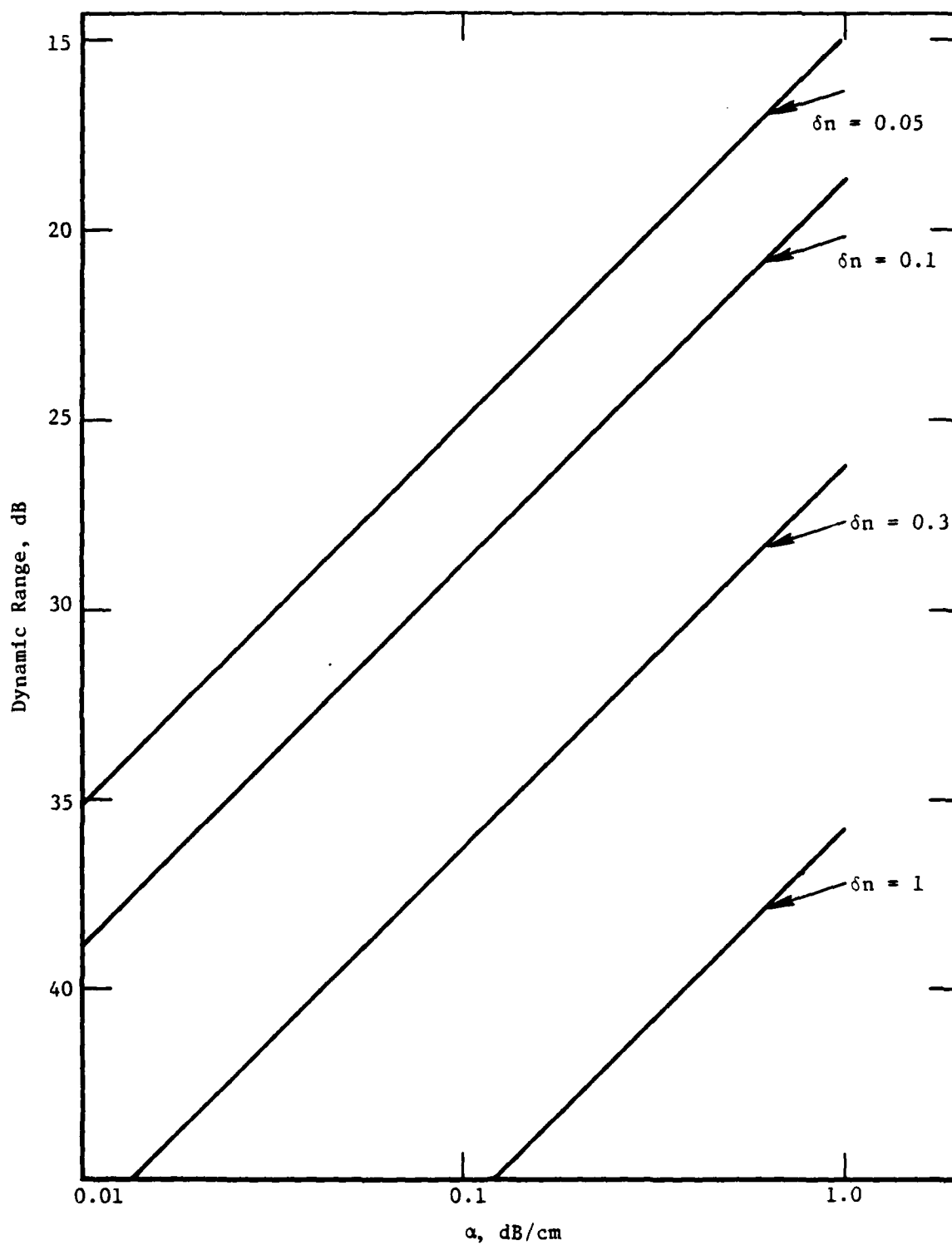
Figure 9. IOSA dynamic range versus waveguide attenuation
coefficient, for the case of Mie scattering
centers.

III. CONSIDERATION OF VARIOUS SCATTERING MECHANISMS AND THEIR INFLUENCE ON IOSA DYNAMIC RANGE

The results of the previous section show the relative dominance of Rayleigh-Gans-Debye and Mie scattering to Rayleigh scattering in limiting IOSA dynamic range. This conclusion is supported experimentally by results presented in the following section, which indicate the presence of small-angle scattering confined to within a few degrees of the beam propagation direction.

There are a number of steps in the fabrication of Ti-diffused LiNbO$_3$ waveguides where either Mie or RGD scattering centers can be introduced. The purpose of this section is to identify such steps and evaluate whether reasonable estimates of scattering center size, refractive index, and density lead to unacceptable values of IOSA dynamic range. Candidate scattering mechanisms to be considered are (1) surface roughness, (2) lithium-titanate surface compounds, (3) the occurrence of the separated phase LiNb$_3$O$_8$, (4) Ti-concentration inhomogeneity, and (5) polishing imperfections.

SURFACE ROUGHNESS

Surface roughness scattering centers are characterized by values of δn on the order of unity when the waveguide superstrate is air. A more careful analysis of surface roughness scattering shows that $\delta n = (n^2-1)/2n = 0.87$ for Ti-diffused LiNbO$_3$ TE modes. We will also identify z_0 with σ, the standard notation for rms surface roughness, and α with the roughness auto-correlation length. We will continue to write z_0 instead of σ to avoid confusion with our notation for scattering cross section.

Substituting $\delta n = 0.87$ into Eq. (43), we find the relation between z_o and δn_g to be

$$\delta n_g = (5.59 \times 10^{-4} \ \mu m^{-1}) z_o \qquad (50)$$

for a step-index waveguide. In the case of surface roughness scattering it is possible to be avoid specifying the nature of the waveguide by using the differential relationship $\delta n_g \simeq (\partial n_g/\partial D) z_o$. For LiNbO$_3$ waveguides, the derivative is accurately described by the relationship

$$\partial n_g/\partial D = k_o \Delta n (2n\Delta n)^{1/2} (\partial b/\partial V), \qquad (51)$$

where b is the normalized mode index and V is the normalized depth. The function b(V) is described by the universal curve appropriate for the wave-guide index profile.[10] In the case of a Gaussian profile, $\partial b/\partial V \simeq 0.1$ for a well confined mode having $b = 0.3$ to 0.4. The use of this value in Eq. (51), along with $\lambda_o = 0.83 \ \mu m$, $n = 2.2$ and $\Delta n = 0.01$, results in

$$\delta n_g = (1.59 \times 10^{-3} \ \mu m^{-1}) z_o \qquad (52)$$

in place of Eq. (50).

Figure 10 shows the corresponding IOSA dynamic range as a function of z_o with a as a parameter. Dynamic range levels of 40 dB are achieved for $z_o \leq 10$ A, and possibly for larger values of z_o if a is as small as several tens of microns. National Bureau of Standards measurements on an undiffused, polished crystal of LiNbO$_3$ obtained from Crystal Technology Corporation show roughness levels ≤ 3.5 A and autocorrelation lengths in the range 20-40 μm.[11] We have noted, however, using differential-interference-phase-contrast micros-copy, an increased roughness in heavily diffused samples. In other experi-ments, we have measured the scattered component of laser light reflected from the waveguide surface, and used the data to evaluate roughness levels of about 30 Å and autocorrelation lengths in the range 50-80 μm.[11] Accord-ing to Fig. 10 these waveguides would be associated with IOSA dynamic range values of about 32 dB, or 8 dB below requirements.

These results show that surface roughness can be a factor limiting IOSA dynamic range to substandard values. However, the potential exists for
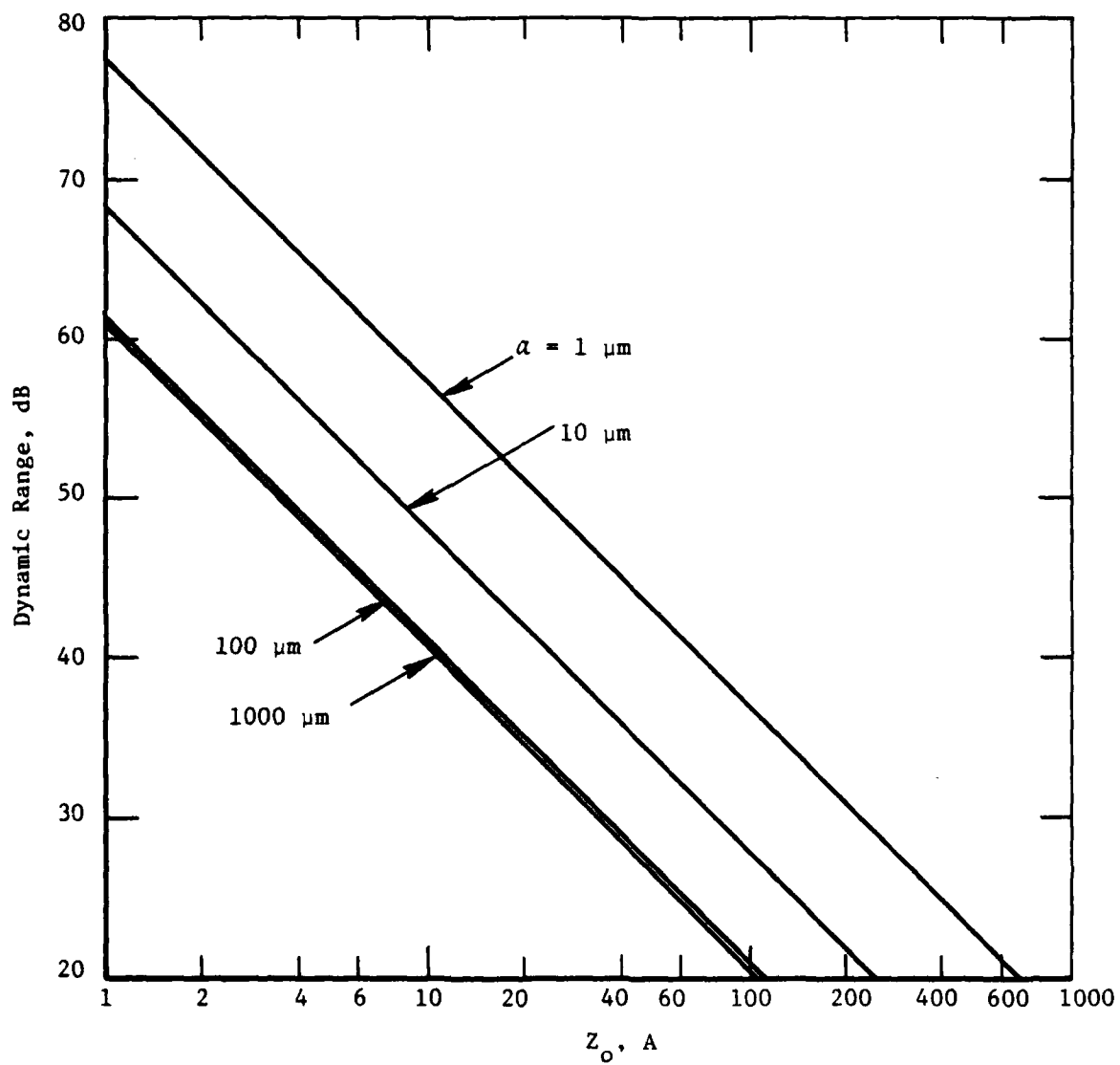
Figure 10. IOSA dynamic range versus surface roughness with autocorrelation length as a parameter.

38

repolishing the fabricated waveguides to improve dynamic range. Reduction of z_o from 30 A to 10 A would appear to be sufficient. We have measured improved scattering performance in waveguides that were polished following Ti diffusion, as indicated in Fig. 11. However, the initial waveguide was heavily diffused with a 720 A thick Ti film. When waveguides formed with Ti films in the vicinity of 200 A were polished after diffusion, no noticeable improvement occurred. The efficacy of post-diffusion polishing for waveguides of the type fabricated for IOSA applications remains to be certified.

Li-Ti-O SURFACE COMPOUNDS

Burns, West, Klein and Plew have presented Secondary Ion Mass Spectroscopy data showing the presence of anomalously high Ti concentrations peaking about 0.1 μm beneath the surface of a Ti-diffused $LiNbO_3$ waveguide.[2] This peak, shown in Fig. 12, apparently served as the Ti source for a Gaussian profile offset from the surface by 0.9 μm and having a diffusion depth of 2 μm (2.9 μm relative to the surface). Holman has noted that Ti-diffused $LiNbO_3$ waveguides will occasionally support a relatively dim mode having a higher effective index than the apparent TE_o mode.[12] Burns has suggested that this mode could be identified with the near-surface Ti concentration peak;[13] that is, the energy of the mode could be localized largely within the peak.

We observed the mode in the sample used to obtain the results of Fig. 11. At the time, the waveguide had been polished for a total of seven hours after diffusion of a 720-A Ti film for 3h at 950°C. The mode was observed for TE propagation parallel to the optical axis only. The effective index of the mode was about 0.002 above that of the nominal TE mode, and the relative scattered intensity at a given angle was about 5 dB greater for the dim mode than for the nominal mode. After 11 hours total polishing, the dim mode disappeared, and a dramatic improvement in waveguide quality, as shown by the last datum in Fig. 11, ensued. These observations suggest that the formation of near-surface inhomogeneities can be a significant source of in-plane scattering, apart from any surface roughness generated during diffusion. Burns, Klein, West and Plew have characterized these inhomogeneities as Li-Ti-O compounds (Li_2TiO_3 or $Li_2Ti_3O_7$) formed in a dilute mixture with
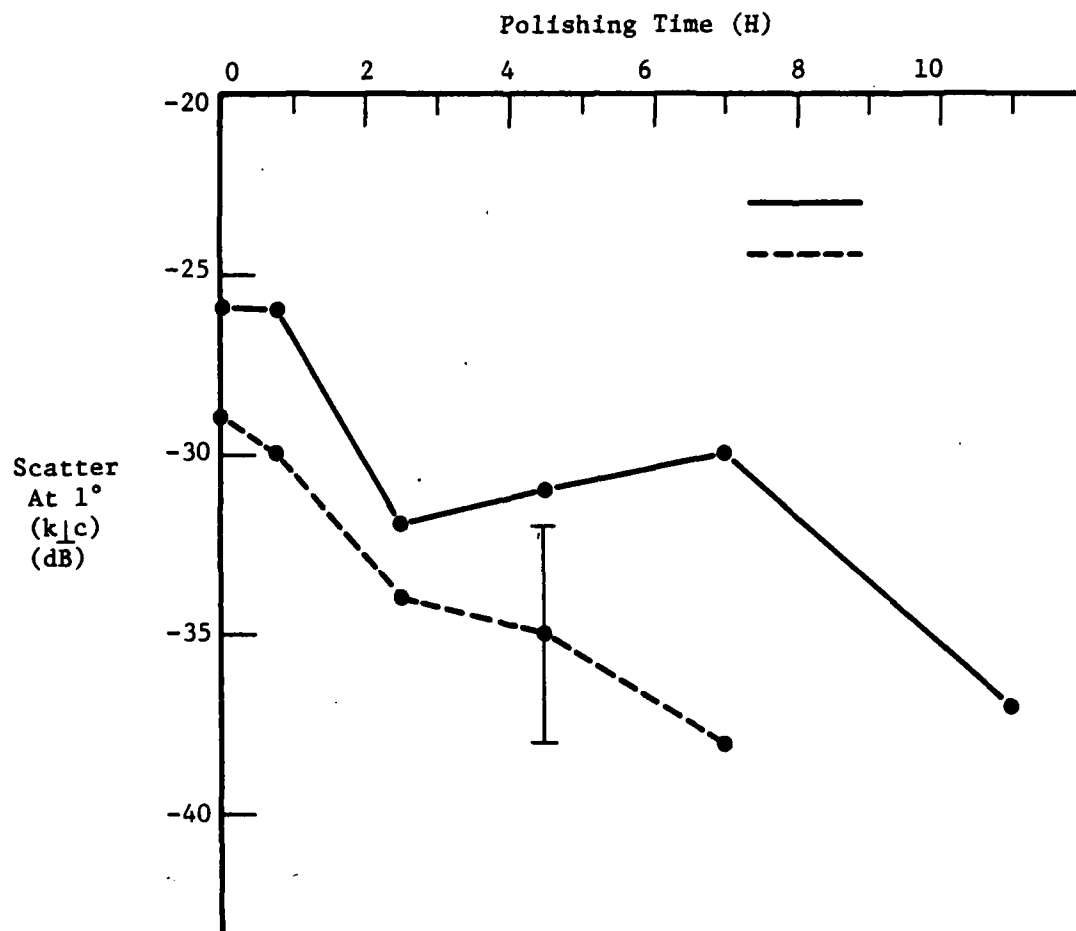
Figure 11. Dependence of scattering on post-fabrication, polishing of a waveguide formed using a 720 Å Ti film. Solid line = TE_O. Dashed line = TM_O mode.
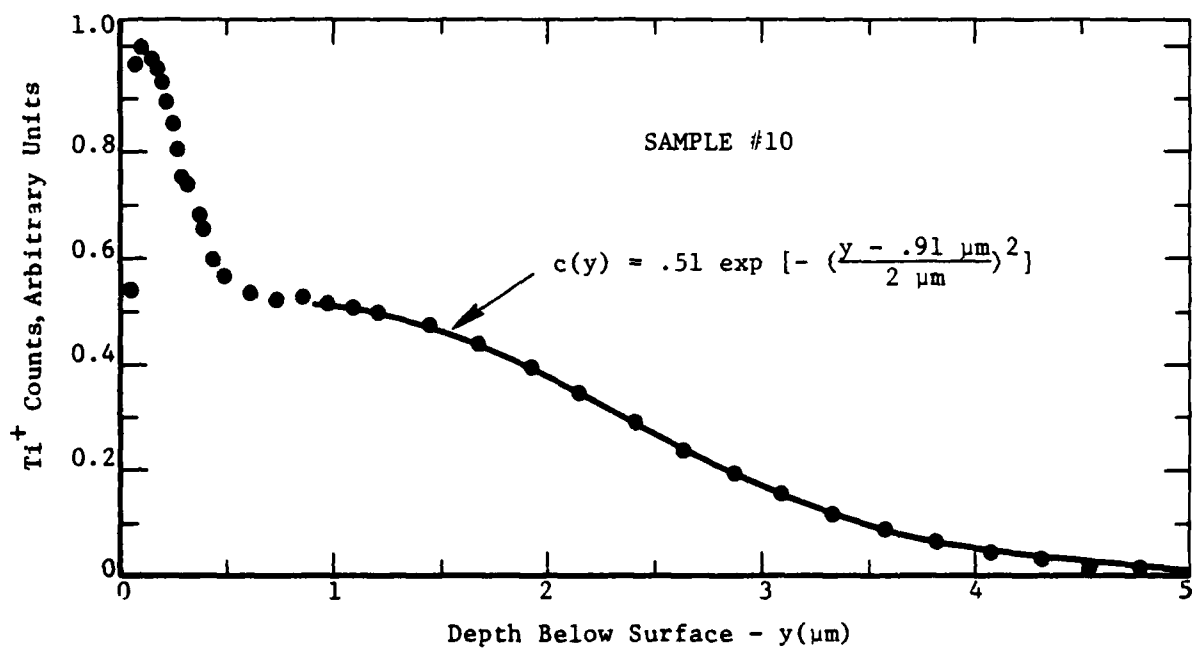
Figure 12. Ti-concentration versus depth beneath the waveguide surface. From Ref. (2).

$LiNbO_3$.[2]   They estimate the concentration of Li-Ti-O compounds to be less than 10 mol%.

In order to estimate IOSA dynamic range limitations associated with the compounds, it is necessary to specify their index perturbation δn and their depth beneath the surface z_0. The latter quantity is estimated from Fig. 12 as 0.4 μm. The former quantity depends on how inhomogeneously the compounds are distributed within z_0. The index perturbation could be negligible for a uniform distribution or it could be as large as the index difference between the Li-Ti-O compounds and the host crystal. The index of Li_2TiO_3 is 2.09, and the other compounds probably have similar values, suggesting that $\delta n \simeq 0.1$ is a good estimate. Since the compounds are believed to be in dilute solution of 10 mol% or less with the host $LiNbO_3$, the effective value of δn may be reduced another order of magnitude to 0.01.

From Eq. (43), based on an analysis for a step index waveguide, the mode index perturbation is calculated to be $\delta n_g = 2.57 \times 10^{-6}$. A factor-of-three increase in δn_g is probably associated with a Gaussian waveguide profile, as we found to be the case for the surface roughness perturbation. In this event, Fig. 7 shows that IOSA dynamic range values greater than 40 dB require $a \leq 3$ μm. This indicates reasonable cause for concern that Li-Ti-O compound formation can be a severe problem in achieving IOSA dynamic range specifications. As with surface roughness, one remedy is post diffusion polishing of the waveguide to remove the compound layer. It is also possible that the layer becomes more homogeneous as the indiffusion process is continued for longer periods.[14] This would avoid the need for post-diffusion polishing but it may produce weakly guiding or multimode waveguides unsuited for the IOSA application.

Recently we have noted less "orange peel" structure on the surface of waveguides formed in the presence of moist, flowing H_2O vapor.[15] This orange peel is probably associated with the increased roughness of diffused waveguides compared to the initial substrate. It may also be indicative of the formation of subsurface Li-Ti-O compounds. The reduction of orange peel using moist flowing H_2O vapor in the presence of oxygen therefore offers promise for reduced waveguide scattering.

PHASE SEPARATION

Another method by which index inhomogeneities can arise in $LiNbO_3$ is formation of the separated phase $LiNb_3O_8$. The process is known to occur most rapidly when the crystal is heated to the vicinity of 800-850°C.[16] Figure 13 shows the severe surface degradation that resulted from an experiment in which a polished sample of $LiNbO_3$ was held at 850°C for 10 minutes. The phenomenon of phase separation may have served to decorate strains that were generated in the crystal during its previous history. If this is true, phase separation is a mechanism for enhancing the scattering stength of existing, small index inhomogeneities.

Although heating of waveguide samples in the vicinity of 850°C for long periods does not normally occur during conventional fabrication procedures, we have noticed increased scattering from some waveguides allowed to cool slowly from the diffusion temperature. This prompted us to initiate a policy of quenching waveguides from the diffusion temperature, usually 950°C, to 600°C, followed by a slower cool to room temperature. This resulted in waveguides that show none of the effects of Fig. 13. However, crystals from a subsequent batch fractured during this quenching operation. When it was temporarily abandoned in response, there was no apparent sacrifice in surface quality. We conclude that problems associated with phase separation are strongly sample dependent.

Fabrication techniques that minimize induced crystalline strain may be the best guard against phase separation effects in $LiNbO_3$ waveguides. These would probably include techniques which reduce Li-Ti-O compound inhomogeneities near the waveguide surface as well. To the extent that phase separation occurs near the vicinity of these inhomogeneities, formation of $LiNb_3O_8$ may add to the inherent scattering. The refractive indices of the monoclinic crystal $LiNb_3O_8$ are 2.28, 2.36, and 2.40. The scattering effect from this phase is therefore comparable to that from similarly sized lithium-titanate inhomogeneities.

In event that $LiNb_3O_8$ aggregates extend through the waveguide layer into the substrate, they will likely produce either Mie scattering centers with $\delta n \lesssim 0.1$ or RGD scattering centers with $\delta n_g >> 10^{-6}$. In either situation IOSA dynamic range values less than the required 40 dB should result. In the
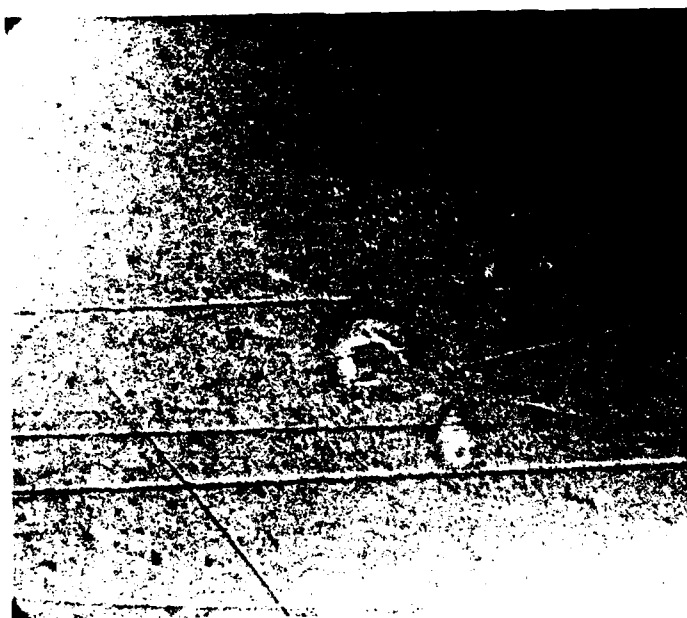
Fig. 13. Nomarski micrograph showing the results of
a 10 min heat treatment of LiNbO₃ at 850°C
in flowing O_2. (500X)

worst case, phase separation produces surface degradation like that shown in
Fig. [13]. The index inhomogeneity associated with these scattering centers
$\delta n \simeq 1$. If their depth is 0.4 μm, they will produce 40 dB more scattered
intensity than we estimate for near surface Li-Ti-O compounds. While this
would be disastrous for the IOSA application, we note that surface degrada-
tion like that of Fig. [13] is not the norm for Ti:LiNbO$_3$ waveguides, and it
can be readily seen when it occurs.

Ti CONCENTRATION INHOMOGENEITIES

One possible source of scattering in Ti:LiNbO$_3$ waveguides is non-
uniform Ti concentration resulting from defects in the initial Ti film. For
example, dust trapped beneath the film during its formation can prevent dif-
fusion of the metal into the waveguide surface. This could be caused by an
explosive removal of the film in the vicinity of the dust particle as the
high diffusion temperature is approached. Alternatively, the dust could
carbonize, react with the metal or the crystal, or otherwise inhibit the
normal diffusion mechanism. Figure [14] shows a micrograph of the edge of a
nominally good waveguide where both of these mechanisms may be in evidence.
The smooth round artifacts that have the appearance of craters are consistent
with the explosive removal hypothesis, in that Ti is known to produce a thick-
ness change in diffused LiNbO$_3$. Where this change is not observed, we may
not have diffused Ti. In contrast globular aggregates in Fig. [14] may show
regions where chemical reactions have inhibited the diffusion mechanism.

None of the structures in Fig. [14] are observed in the center of the
waveguide sample, where surface cleanliness is easier to achieve and maintain.
Nevertheless an occasional dust particle could produce a Ti-free region of
the waveguide where the effective index is reduced from n_g to the substrate
index n. For a well-confined TE$_o$ mode in a single-mode waveguide, the re-
sultant index inhomogeneity would be $\delta n_g \simeq 0.003$. While this is a fairly
strong RGD scattering center or a weak Mie scattering center, IOSA dynamic
range will only be seriously impaired if the density of these scattering
centers is sufficiently large. Figure 15 shows a plot of IOSA dynamic
range versus Σ with scattering center size a as a parameter. The plot is
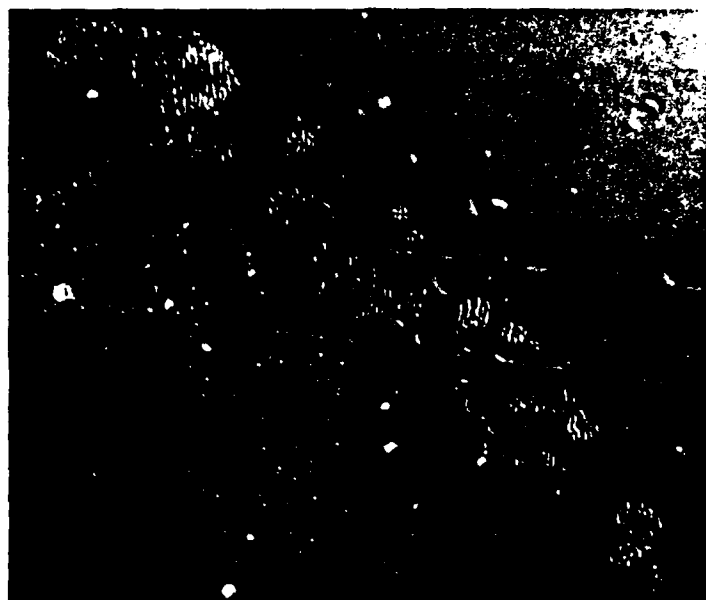based on an RGD scattering analysis. The size of the smooth craters in

Fig. 14. Nomarski micrograph showing artifacts
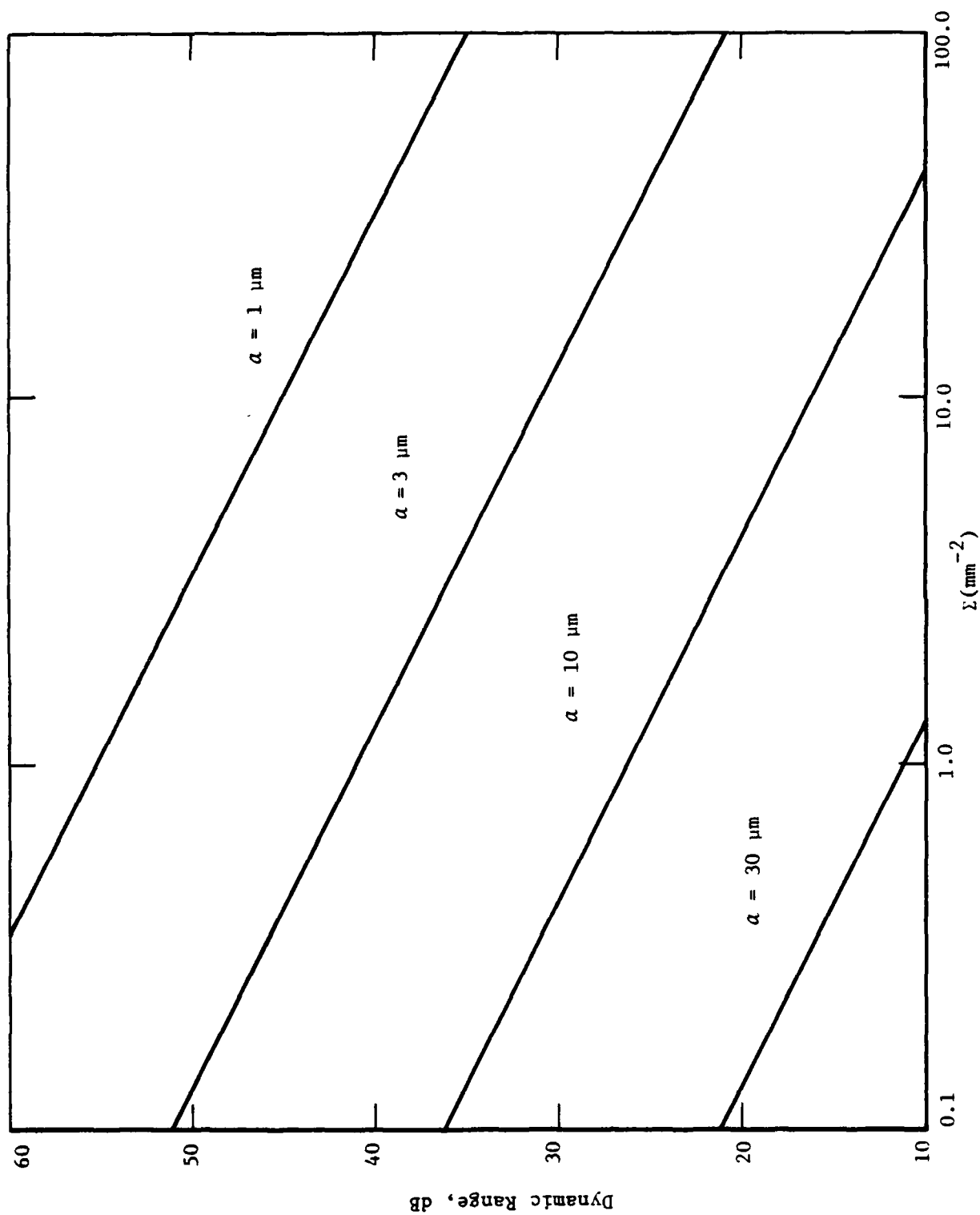near the edge of a Ti-diffused LiNbO$_3$
waveguide. (500X)

Figure 15. IOSA dynamic range versus surface density of Ti-voids in the diffused waveguide, with void size as a parameter.

47

Fig. 14 is in the range 3-10 μm. Therefore, achievement of an IOSA dynamic range greater than 40 dB requires that the density of such craters be reduced to about 0.1 mm^{-2} or 10 cm^{-2}. This is within the realm of careful sample preparation procedures.

POLISHING IMPERFECTIONS

When glass is polished improperly, it is possible to obtain a smooth surface on top of a layer containing voids and inhomogeneities. This occurs because of the ability of glass to flow during the polishing operation, and thereby to cover as well as remove damage generated during previous polishing steps. Although the polishing characteristics of $LiNbO_3$ are very different from glass, there is concern that a similar situation could exist in the case of improperly polished $LiNbO_3$.

Subsurface damage, if it exists, must be comprised of scattering centers small compared to a wavelength or it would very likely be visible under a microscope. If the damage is small compared to a wavelength, IOSA dynamic range is described by Fig. 5 for Rayleigh scattering. The achievement of 40 dB or more dynamic range is tied to the reduction of waveguide attenuation levels to 0.25 dB/cm or less. Since this is within the state of the art, and since our experiments to be described do not show the presence of Rayleigh Scattering, we do not perceive polishing imperfections to be a serious problem limiting IOSA dynamic range.

SUMMARY

The analysis of this section shows that RGD scattering centers associated with surface roughness and near-surface compound formation should be among the hardest to diagnose and prevent, as well as among the most damaging to IOSA dynamic range. Much of our experimental evidence in the following section will be found to support this assertion.

IV. EXPERIMENTAL STUDIES OF IN-PLANE
SCATTERING IN Ti:LiNbO$_3$ WAVEGUIDES

MEASUREMENT OBJECTIVE

The objective of our experimental program has been to measure the parameters $\Sigma\sigma(0)$ and q using observations of in-plane scattering in diffused Ti:LiNbO$_3$ waveguides fabricated in various ways. According to the theory developed in Sec. II, measurement of $\Sigma\sigma(0)$ and q allows us to predict the scattering limits to dynamic range in the IOSA application. By correlating the values of the scattering parameters with waveguide fabrication parameters, we may, in addition, hope to develop a set of optimized fabrication conditions. We may also, by careful interpretation and analysis of results, hope to reach valid conclusions about the dominant source of scattering in the waveguides.

The obvious method for measuring the in-plane scattering parameters is shown in Fig. 16. A collimated laser beam is coupled into and out of the waveguide and brought to a focus. In-plane scattered energy is distributed along the "m-line" consisting of a brightly focused central spot and a diffuse component that decreases in intensity symmetrically with distance on either side. This component fluctuates in intensity owing to optical interference of coherent rays generated by randomly positioned scattering centers.

If a slit of width s is positioned a distance y from the focus, the slit will pass rays scattered in the waveguide plane within an angular sector extending from $\phi - \Delta\phi/2$ to $\phi + \Delta\phi/2$, where

$$\phi = y/nf,$$

$$\Delta\phi = s/nf. \tag{53}$$

The focal length of the lens is f, and a factor n is introduced to account for the refraction of light rays in leaving the waveguide medium and entering air. From Eq. (2), the scattered power passed by the slit is
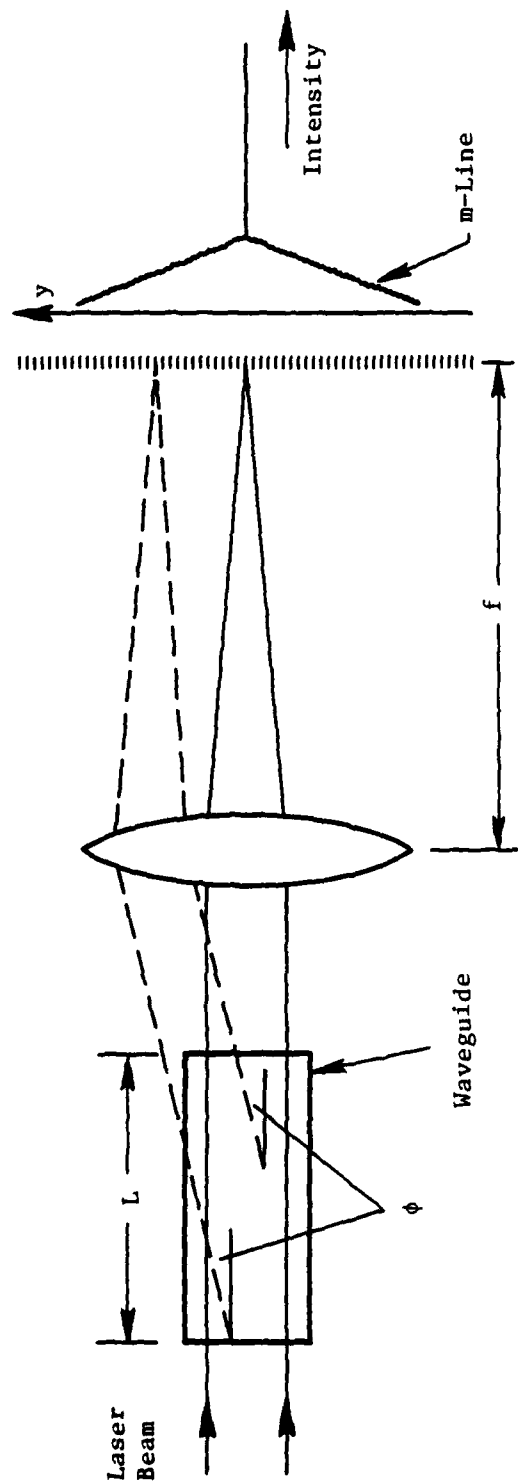
$$\Delta P(y) = PL\Sigma\sigma(y/nf)(s/nf). \tag{54}$$

49

Figure 16. Fourier-transform geometry for measurement of in-plane scattering parameters.

50

At $y = 0$, the scattered power is swamped by the focused power associated with the unscattered beam. This is

$$P(0) = P \; \text{erf}(\pi 2^{1/2} \; sW/4f\lambda_o). \tag{55}$$

In processing the experimental data, the scattered power is usually divided by the peak power. The measured quantity is then

$$\Delta P(y)/P(0) = L\Sigma\sigma(y/nf)(s/nf) \, [\text{erf}(\pi 2^{1/2} \; sW/4f\lambda_o)]^{-1}. \tag{56}$$

For a slit width small compared to the focal spot size, this result reduces to

$$\Delta P(\phi)/P(0) \simeq (2/\pi)^{1/2}(L/W)(\lambda_o/n)\Sigma\sigma(\phi), \tag{57}$$

where we have reinserted ϕ in place of y/nf. All parameters in the equation other than $\Sigma\sigma(\phi)$ are known. Therefore the data is directly proportional to the scattering parameters and the constant of proportionality can be calculated.

THE DEVELOPMENT OF
EXPERIMENTAL PROCEDURES

Evidence for Scattering from Prism Coupling

The main experimental problem is that of insuring that the measured scattered light is produced only by waveguide scattering along the path L between input and output coupling. All optical components that refract, reflect, or aperture the beam contribute to light intensity outside the focal spot. This is effectively a source of measurement noise that must be either eliminated or carefully accounted for. Most optical components can be selected to be of sufficiently high optical quality that scattering from them is not a serious problem. In addition, scattered light from components well removed from the measurement plane can be effectively shielded from the plane by careful aperturing.

The source of the worst problems is scattering generated during input and output coupling from the waveguide. This source of scattering is in-plane and cannot effectively be apertured because of its close proximity to the scattered light from the waveguide. In the case of prism coupling, evidence for coupling-related scattering is the observation of nearly identical m-lines for different coupling-prism separations. Figure 17 shows one example of the variation of total scattered power as a function of
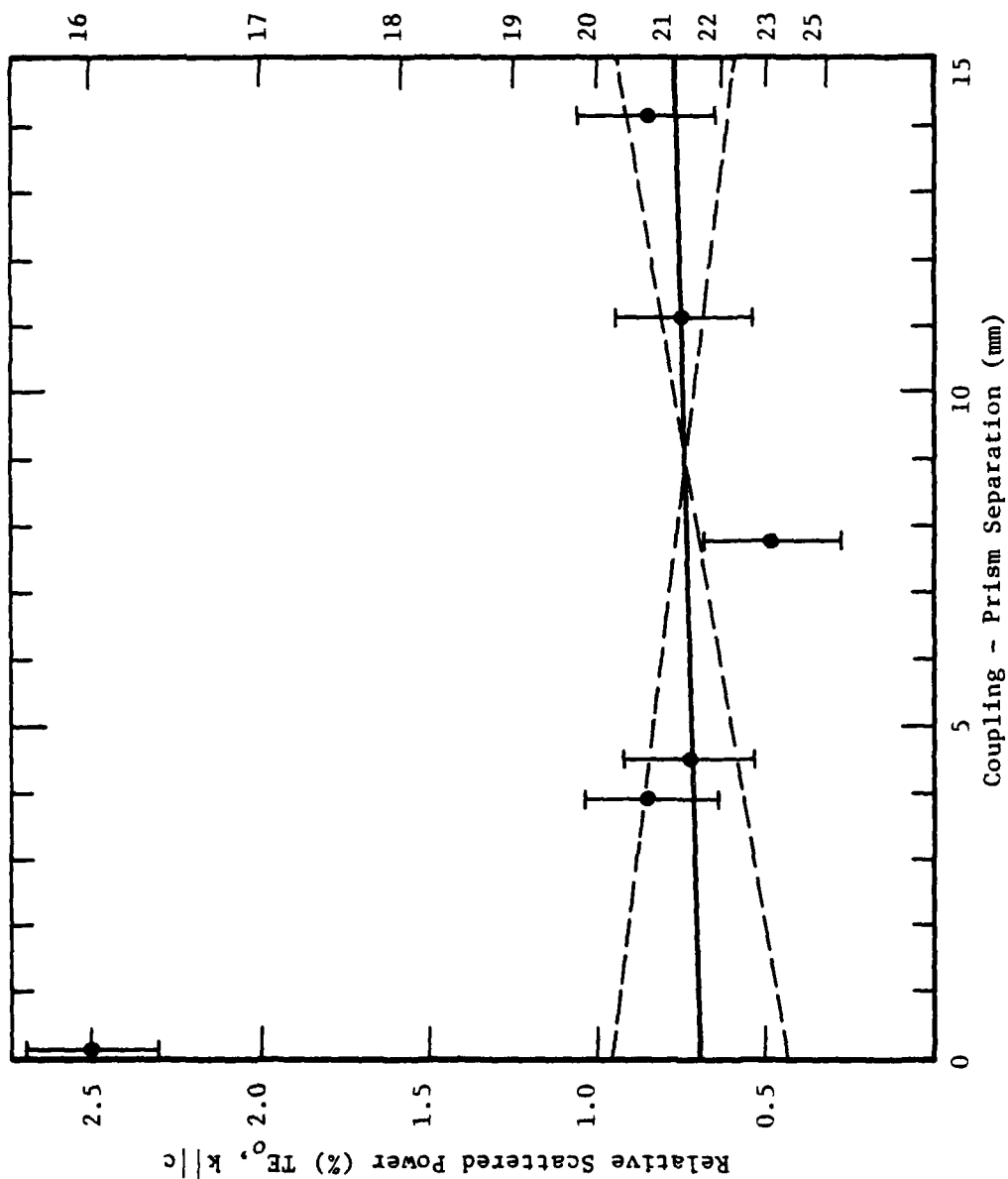
51

Figure 17. Relative scattered power vs. coupling prism separation for Ti:LiNbO3 waveguide #166 (TE$_o$ mode, k||c).

coupling prism separation. The experiment measured the total power scattered into an angular sector about 1.3° on either side of the optical axis. The results were normalized by dividing by the unscattered power leaving the waveguide. For RGD scattering, the expected variation is obtained by inserting Eq. (1) into Eq. (2) and integrating from $\phi = -1.3°$ to $\phi = +1.3°$. The result is

$$\Delta P_{tot}/P = 2L\Sigma\sigma(0)(k_o a)^{-1} \tan^{-1}(0.024\ k_o a), \qquad (58)$$

A plot of $\Delta P_{tot}/P$ versus path length L should plot as a straight line with zero intercept. The results of Fig. 17 show, in contrast, a finite intercept associated with prism-related scattering. The best fitting straight line indicates that at a path length of 15 mm, only 9% of the total scattering observed comes from the waveguide. 91% comes from prism coupling. The dashed straight lines are within one standard deviation of the best fitting straight line, and they show the possibility that the correct straight line through the data has zero slope, indicative of the result $\Sigma\sigma(0) = 0$. That is, the waveguide is scatter free.

The best straight line fit is used to obtain the lower curve in the graph of Fig. 18. This curve shows that the waveguide used to obtain the Fig. 17 results is capable of providing an IOSA dynamic range better than 40 dB if scattering center size is greater than about 3 μm. However, the upper curve in Fig. 18 is associated with the dashed fit to the data of Fig. 17 showing a slope just one standard deviation higher than the best fitting slope. And this curve indicates that a dynamic range of 40 dB is not achieved for any scattering-center size in the range from 1-100 μm.

Data taken using the TM_o mode instead of the TE_o mode are also disheartening. For that data, the most likely IOSA dynamic range curve is the same as the top curve in Fig. 18. A further 3 dB dynamic range is sacrificed when the steepest slope within one standard deviation of the best slope is employed in the calculation. However the shallowest slope within one standard deviation of the best slope allows for the possibility of zero waveguide scattering. In short, the data tells us that the waveguide may be adequate for the IOSA application, or that 10 dB further scattering reduction is needed. Unfortunately the error bars do not allow for a more precise conclusion.
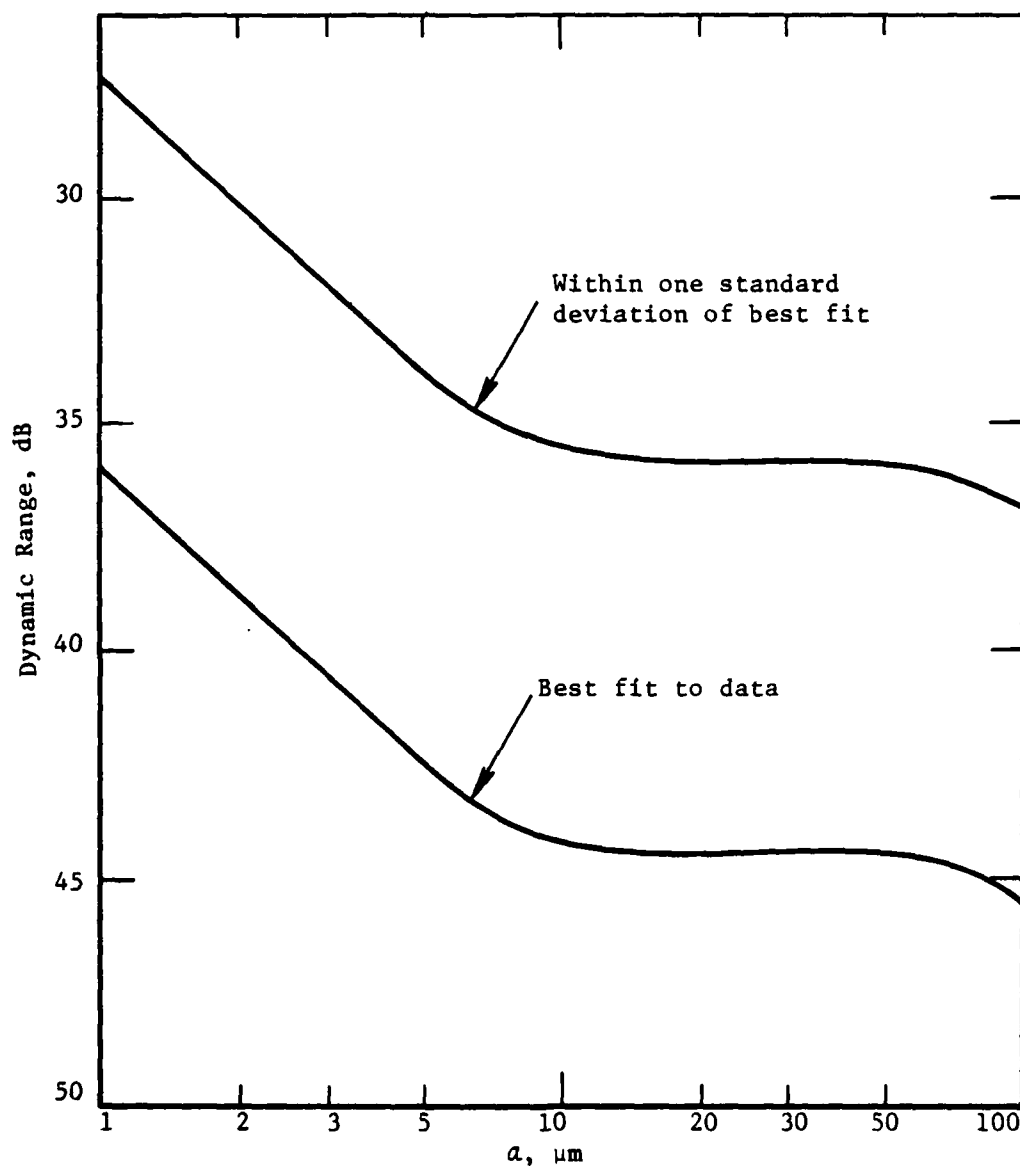
Figure 18. IOSA dynamic range versus scattering center size, based on the experimental data of Figure 17.

Figure 19 shows a different type of measurement on the same waveguide, in which 10 log $\Delta P(\phi)/P(0)$ is plotted as a function of scattering angle in the waveguide. The measurement was made by continuously scanning a slit along the focused m-line. A fiber bundle coupled to the slit collected the light passed by it and transmitted the light a photomultiplier tube. Figure 19 actually contains the results of two separate experiments, in which the coupling- prism separation was either 15 mm or 1 mm, approximately. The data for the two experiments are superimposed, with the dashed curve representing the results obtained using closely spaced coupling prisms. The overall envelopes of the two curves are nearly identical. A statistical analysis has been used to generate Lorentzian shaped best fitting curves for the two measurements. These are also plotted in Fig. 19. They indicate a slight excess of scattering for the case of well-separated coupling prisms. However the excess is small compared with the fluctuations associated with laser speckle. Accordingly it is difficult to use Eq. (55) to obtain an accurate determination of $\Sigma\sigma(\phi)$, as required to predict IOSA dynamic range. To the extent that the data can be trusted, the two Lorentzian curves determine the values $\Sigma\sigma(0) = 5.7 \times 10^{-2}$ mm^{-1} and $\alpha = 20$ μm. The corresponding IOSA dynamic range at the fourth off-axis pixel is 32 dB. This is 4 dB worse than the more pessimistic value indicated in Fig. 18.

Mechanisms for Scattering from Prism Coupling

We have considered two mechanisms by which prism coupling can add to the amount of in-plane scattered light, even if the prism contains no scattering centers itself.

One is based on the possibility that the electromagnetic field at the surface is enhanced in the region where light is being prism coupled into the waveguide. The field in this region consists of the waveguide modal field plus the evanescent field generated in the base of the coupling prism by the incoming laser beam. Some of this field is reflected and does not contribute to the modal field. Yet it is phase-matched with the modal field and can presumably generated scattered light which is trapped in the waveguide. This scattering mechanism relies on the incoming laser beam and so it exists only for prism input coupling. We have observed
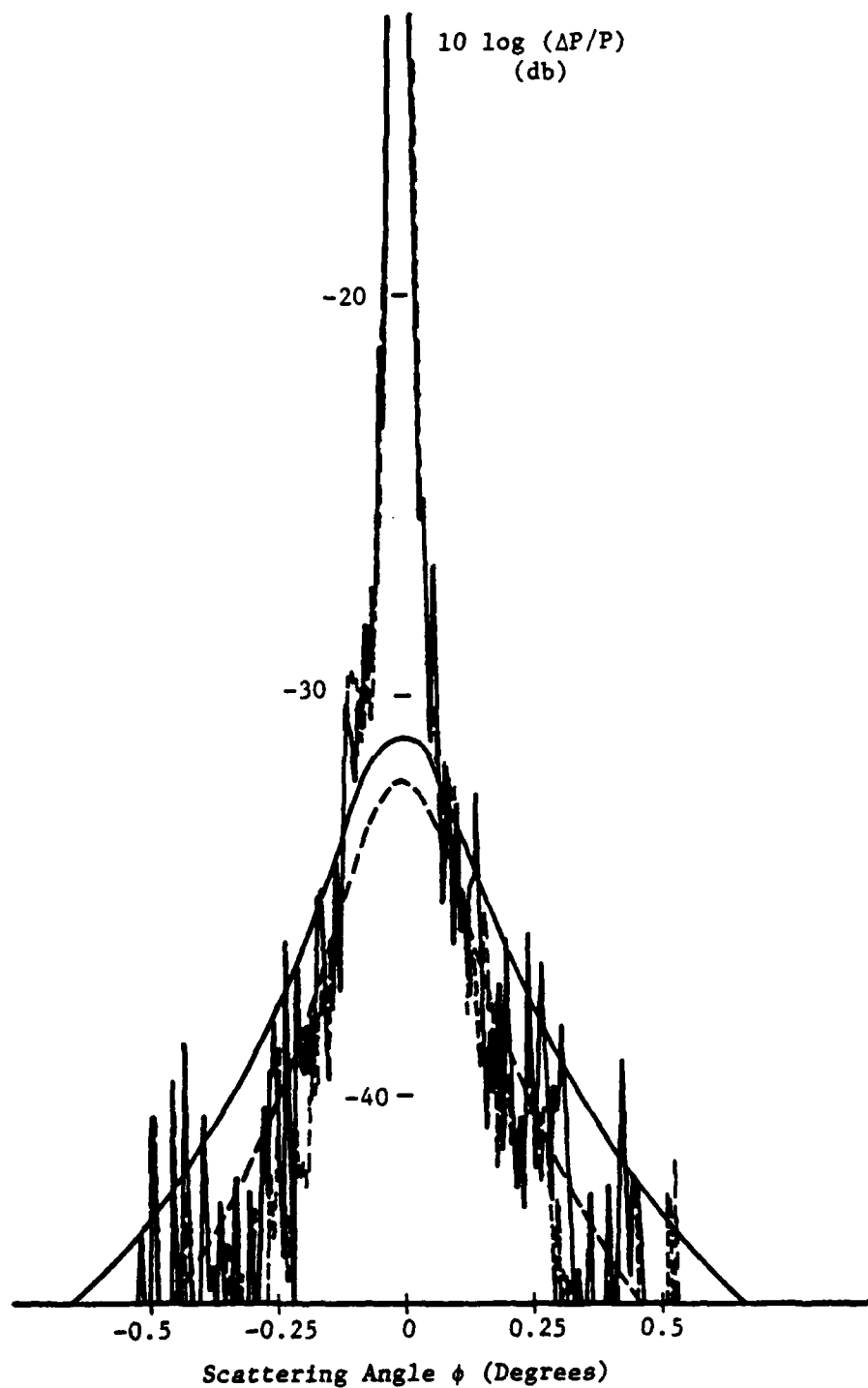
55

Figure 19. In-plane scattered energy distribution for sample 166 (TM$_o$, k$\perp$c). Scattering angles are referenced to wave-guide material.

cases for which light was end-fire coupled into a waveguide and prism coupled out. Qualitatively, the scattering in this situation was less than when the coupling roles were reversed. However, data to support this were not acquired. Calculations presented in Ref. 11 show that the postulated mechanism is realistic, but they do not support the extent to which prism scattering appears to dominate waveguide scattering in practice.

A second mechanism for prism scattering is found in spatial variations in coupling efficiency across the width of an incoming beam. After coupling, the profile of an initially Gaussian beam may contain structure of characteristic size Δ. The diffraction pattern produced in the far field is indistinguishable from that produced by scattering centers of the same size. This mechanism exists for both input and output prism coupling.

To estimate the size of this effect, let us assume that $A(y)$ is the amplitude profile of an ideal Gaussian beam, y being the transverse direction in the plane of the waveguide. The actual profile of an in-coupled beam is $[1 + t(y)]A(y)$, where $t(y)$ is related to the spatial variation of input coupling efficiency. If the beam of light is coupled out of the waveguide and focused by a lens of focal length f, the field at the focal plane will be

$$E(Y) = E_o(Y) + E_p(Y)$$

$$E_p(Y) = (if\lambda_o)^{-1/2} \int_{-\infty}^{\infty} t(y)A(y)e^{-2\pi iyY/f\lambda_o}\, dy \tag{59}$$

where $E_o(Y)$ is the ideal Gaussian field and $E_p(Y)$ is the field associated with nonuniform prism coupling efficiency. The relative power in the field E_p is $\Delta P_p(Y)/P(0) = \langle E_p E_p^* \rangle / E_o^2(0)$. The bracketed quantity is

$$\langle E_p E_p^* \rangle = (f\lambda_o)^{-1} \int_{-\infty}^{\infty} \int_{-\infty}^{\infty} dy\,dy' \, \langle t(y)t(y') \rangle \, A(y)A(y')e^{-2\pi i(y-y')Y/f\lambda_o} \tag{60}$$

A standard approach to integrals of this type is to set $\langle t(y)t(y') \rangle = t_o^2 \exp(-|y-y'|/\Delta)$, where t_o is the rms amplitude transmission fluctuation, and Δ is the correlation length associated with these fluctuations. If the beam waist W is large compared to Δ, we find

$$\Delta P_p(\phi)/P(0) = 2(2/\pi)^{1/2} t_o^2 (\Delta/W) [1 + (k_o \Delta\phi)^2]^{-1} \qquad (61)$$

where $\phi = Y/f$. The angular variation is a Lorentzian function in which Δ plays the same role that the scattering-center size a plays in scattering analysis.

To estimate the magnitude of this pseudo-scattering effect, we have measured output-coupled beam profiles within 2 cm of the output coupling prism. The result is shown in Fig. 20. The detector was a linear photo-diode array with a 25-μm center-to-center pixel spacing. The deviations of the beam profile from an ideal Gaussian shape are described by $[1 + t(y)]^2 \simeq 1 + 2t(y)$. Without being quantitative, an examination of Fig. 20 suggests that fluctuations from a smooth, average beam profile are typically 30%, and that individual fluctuations span about 4 channels or 100 μm. Thus we estimate $2t_o \simeq 0.30$ and $\Delta = 100$ μm. The on-axis scattered power associated with prism coupling effects is therefore $2(2/\pi)^{1/2} t_o(\Delta/W)$ $\simeq 3.6 \times 10^{-4}$ or -24.4 dB when $W = 1$ mm. This is comparable to what we have observed in many experiments. The on-axis scattered power from the wave-guide is $(L/W)\Sigma\sigma(0)\lambda_o/n$. If this value is small compared to -25 dB, the wave-guide scattering is swamped by the pseudo-scattering associated with input coupling variations.

Experimental Approaches to the Prism-Scattering Problem

To circumvent this problem we have utilized five different experi-mental approaches: (1) Acquire scattering data using two or more separations between the input and output coupling prisms. (2) Avoid the use of prisms by implementing end-fire entry and exit of light from polished waveguide terminations. (3) Use waveguides with a long path length to increase the amount of waveguide scattering detected. (4) Take data at increasingly large scattering angles to avoid interference with prism scattering that predominates at small angles. (5) Use an imaging technique to avoid detec-tion of light scattered during input coupling. Our comments on these approaches are as follows:

(1) Vary coupling prism separation. We have discussed this ap-proach in connection with Figs. 17-19 and we will use it again later with reference to other data.
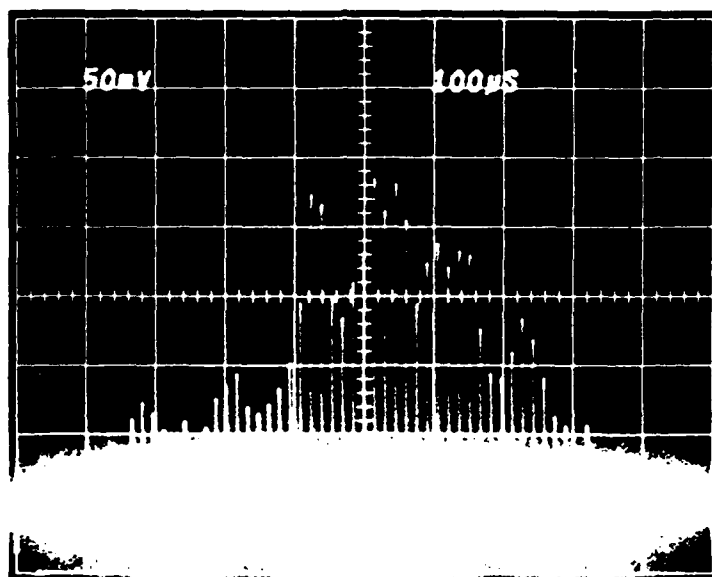
Figure 20. Output beam profile showing effects of
nonuniform prism coupling efficiency.
(Pixel spacing is 25 µm).

(2) <u>Use end-fire coupling</u>. With this method we have found scattering levels greater than obtained using prism coupling.

(3) <u>Increase waveguide path length</u>. We have used paths as long as 57 mm without increasing the waveguide scattering level significantly above the background level.

(4) <u>Examine larger scattering angles</u>. If Δ is larger than a, then the prism-scattered component described by Eq. 59 will eventually fall below the waveguide scattered component described by Eq. (55). To take advantage of this we have increased the angular range of our measurements a factor of about five beyond the range indicated in Fig. 19. At large angles, however, the relative scattered power varies as $\Sigma\sigma(0)/k^2 a^2 \phi^2$. The data serves only to determine the combination of parameters $\Sigma\sigma(0)a^{-2}$. Not enough information is available to determine $\Sigma\sigma(0)$ and a separately, as required for IOSA dynamic-range prediction.

(5) <u>Use of an imaging technique</u>. In this technique a focused beam is coupled into the waveguide using either prism or end-fire methods. The beam diverges as it propagates in the waveguide. After output coupling the beam is again brought to a focus. Light scattered in the region of input coupling is imaged at the focus. Consequently it is swamped by unscattered light and does not contribute to the measured level of scattered power. This technique is useful only if output coupling can be performed without adding scattered light to the beam. Thus, it is not useful if coupling efficiency nonuniformities are the dominant cause of prism-associated scattering. Possibly for this reason, our results with this technique were not encouraging.

EXPERIMENTAL RESULTS

Comparison of Waveguide Fabrication Methods

The samples employed in this research were of two general categories: those fabricated at Battelle and those fabricated at Westinghouse. In both cases, polished crystals of $LiNbO_3$ were purchased from Crystal Technology. The Battelle waveguides were formed on 25 mm x 25 mm x 3 mm substrates, while the Westinghouse waveguides were formed on 75 mm x 25 mm x 3 mm substrates. The Westinghouse waveguides were made identical to those used in the fabrication of their IOSA systems.[4] Titanium film thicknesses were in the

range 275-300 Å. Diffusions were performed at 1000°C for 6 hr in an environment containing $LiNbO_3$ powder, to prevent outdiffusion, and sufficient O_2 to prevent discoloration. The Battelle samples were made using Ti-film thicknesses in the range 175-600 Å, but most samples were made with thicknesses about equal to those used by Westinghouse. Battelle diffusion temperatures tended to be similar ($\leq$ 1000°C) and shorter (typically 3 hr.). Contrary to the common experience, we find these conditions sufficient to complete the diffusion process. This possibly has to do with the initial oxygen content of the sputtered or e-beam evaporated Ti film. However, one would anticipate that the Battelle waveguides are shallower and have a larger surface index change. According to the discussion of Sec. III, this should produce greater scattering from surface roughness or surface index inhomogeneities. However, we have observed that recent Battelle fabrication methods employing flowing water vapor [15] produce less surface disruption than the above-described Westinghouse procedure.

Methods of Data Acquisition

Figure 21 shows one of two experimental configurations used to measure in-plane scattering parameters in $Ti:LiNbO_3$ waveguides provided by Westinghouse. The system uses the conventional Fourier-transform geometry in which a collimated guided beam is focused by a lens to provide the far field distribution from which scattering parameters are obtained in accord with Eq. [57]. In Fig. 21 a second lens is employed to produce a 25X magnified image of the far-field distribution on the linear detector array of an optical mutichannel analyzer (OMA). The length of the detector array is 12.7 mm. Thus the array records the intensity distribution over a length 12.7 mm/25 $\approx$ 0.5 mm measured in the focal plane of the first lens. Since the focal length of the first lens is 45 mm, the detector array subtends an angular range of 0.5/45 or 0.64°. In order to examine a total angular range of 6°, it is necessary to step the second lens perpendicular to the beam through approximately 10 positions separated by 0.5 mm. At each position, a photograph of the OMA output constitutes part of the raw data. One such photograph is shown in Fig. 22.
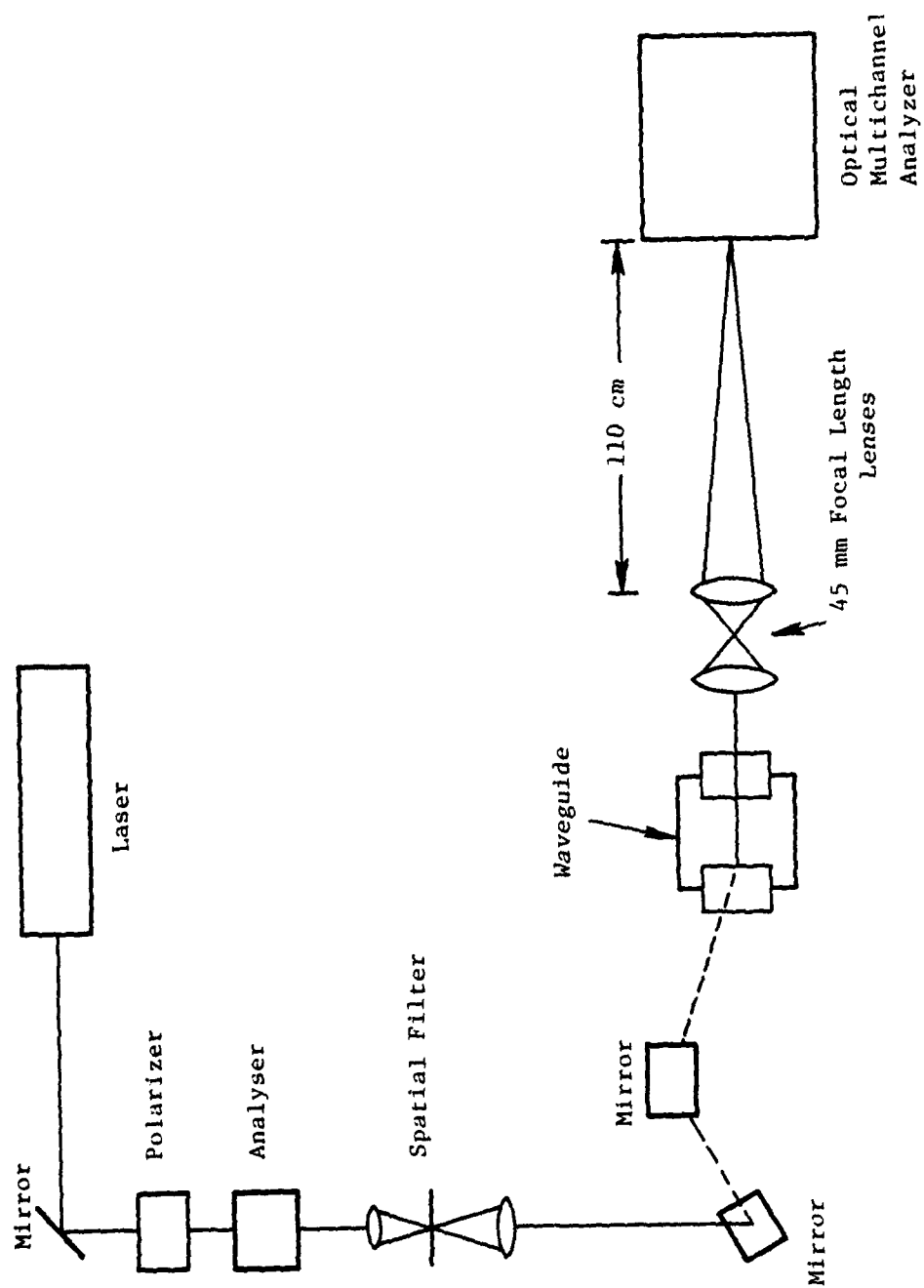
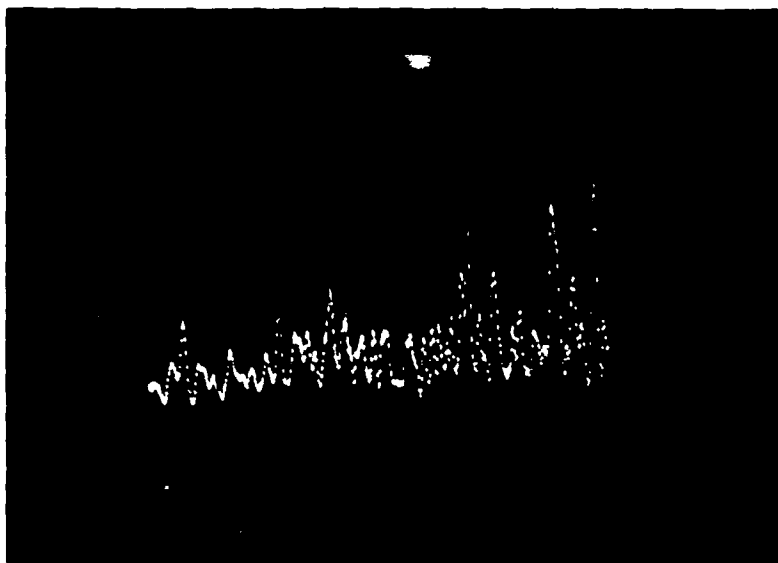Figure 21. Schematic diagram of experimental configuration for in-plane scattering measurements.

62

Figure 22. Representative waveguide scattering
data taken using the OMA.

The OMA is calibrated so that the scattered power into any of the 500 pixels may be inferred from the height of the signal measured from the photograph or read from the instrument display panel when the data is taken. Although the peak power from the focused unscattered beam is shielded from the detector array, this power is known from a separate measurement of the total power in the beam, plus an initial determination of the fraction of this power captured by a centrally illuminated pixel when the beam is not shielded from the array.

Thus, $\Delta P(\phi)/P(0)$ may be measured for scattering angles ranging from $\phi = 0°$ to $6°$ in air, or $0°$ to $6°/2.2 = 2.7°$ in the waveguide medium. Since the scattered power goes down as the scattering angle ϕ increases, the laser power is increased as needed to insure that the level of scattered power incident on the detector array is maintained at a suitable value in excess of the noise level but below saturation. We have measured and plotted the scattered power only in the fluctuation peaks in order to provide the envelope of the actual distribution. For data like that shown in Fig. 22 we select three to five roughly equally spaced fluctuation peaks for use in the analysis.

Westinghouse Samples

Westinghouse Corporation provided us with two samples made by similar techniques but of very different quality. Most of our results were obtained with the better of the two samples, called W1. Using the experimental arrangement of Fig. 21, we took data with W1 for prism separation of about 53 mm and about 1 mm, and plotted the results on the same graph. Several months later we repeated the experiment to check for reproducibility. Figures 23 and 24 show the results of these two runs.

Data obtained with input and output prisms separated by only 1 mm are plotted as plus signs, while data obtained with prisms separated by 52 or 53 mm are plotted as dots. Scattering contributed from the waveguide path should cause the dots to be located above the plusses, assuming that the scattering associated with prism coupling is the same for both prism separations. We find that dots lie above plusses only for scattering angles less than $3°$ in Fig. 23. In Fig. 24, the scattered power at similarly

Figure 23. Normalized scattered power versus scattering angle for the TM_0 mode of Sample W1. Dots correspond to 53 mm prism separation. Pluses correspond to less than 1 mm prism separation.
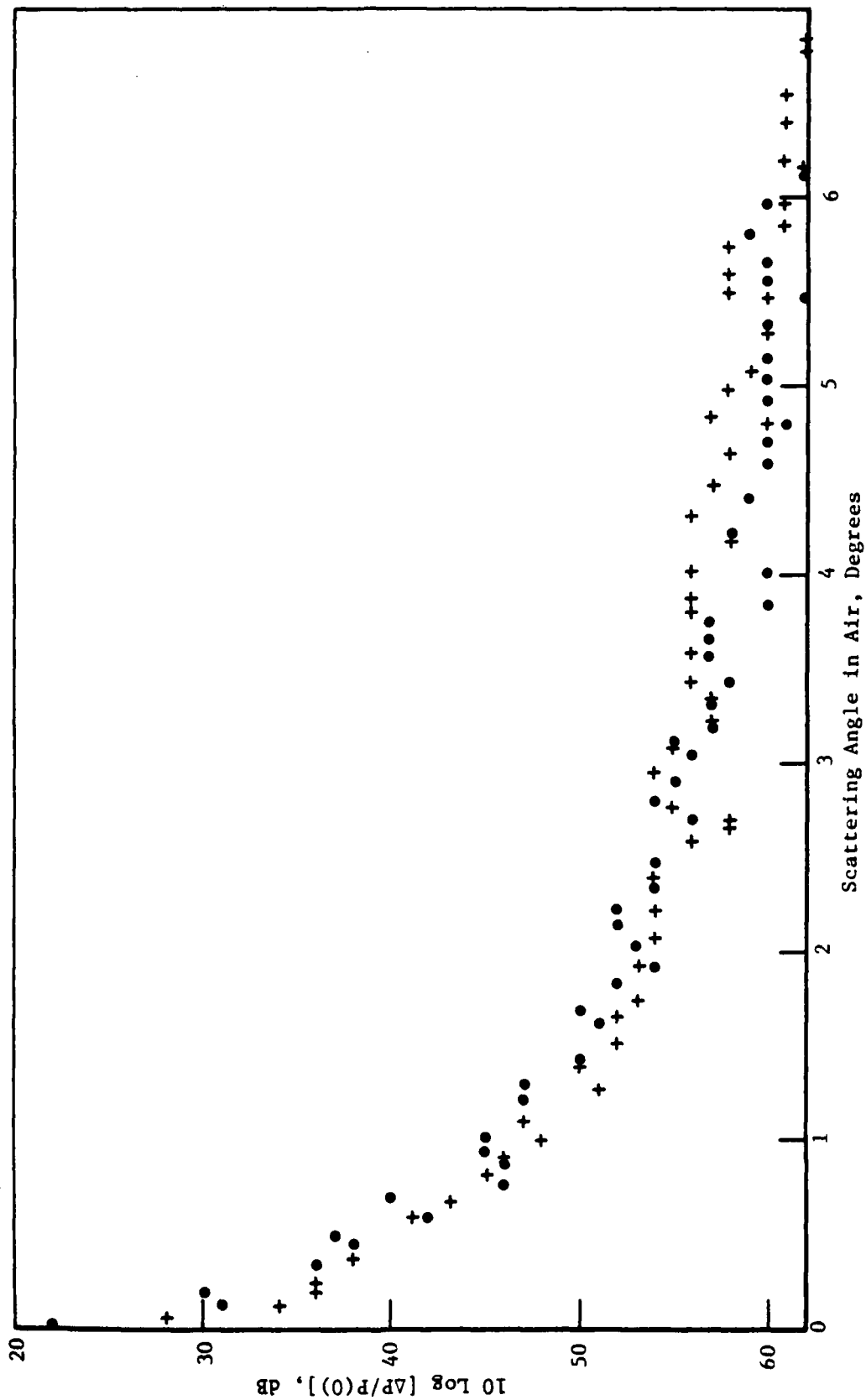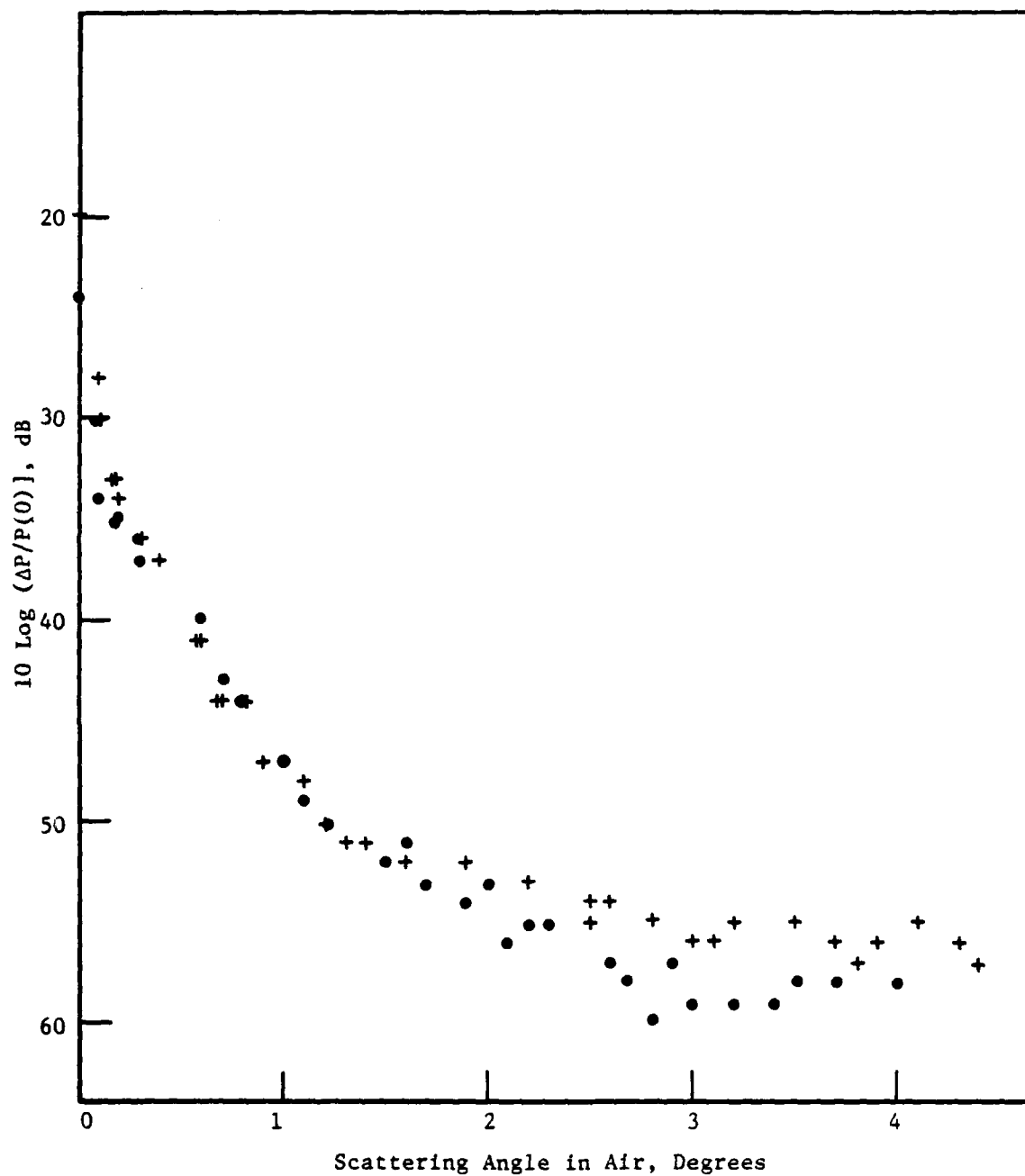
Figure 24. Normalized scattered power versus scattering angle for the TM_0 mode of sample W1. Dots correspond to 52 mm prism separation. Pluses correspond to less than 1 mm prism separation. Data were taken two months after data of Fig. 23 using essentially the same experimental set up.

66

small angles is nearly indpendent of prism separation. At large angles,
plusses are above the dots in both figures, indicating the unphysical result
that scattering is greater when waveguide path length is less.

We later learned that background scattering from optical components
other than prisms was dominant at these large scattering angles. This scat-
tered component was apparently detected in greater amounts when the prisms
were placed close together, owing to the experimental geometry. Because of
it, we have to ignore the data at scattering angles larger than 2.2° in
both Fig. 23 and 24. At very small scattering angles, less than 0.5°, we
remain unsure of the data because of the pseudo-scattering associated with
spatial variations in coupling efficiency, discussed earlier.

As a result, we concentrate our analysis on data falling in the range
0.5°-2.2°. Moreover, we correct the data in this range by subtracting that
part of the scattered power contributed by the nearly constant background
at larger angles. This background was estimated at -56 dB for the + data
and -58 dB for the ● data. The results are found to closely fit a Lorentzian
angular distribution characteristic of RGD scattering centers,

$$\Delta P(\phi)/P(0) = (\Delta P/P)_{max} [1 + (k_o a \pi/180)^2 \phi^2]^{-1} \tag{62}$$

where $(\Delta P/P)_{max}$ depends on waveguide and prism scattering parameters. Figures
25 and 26 show the corrected data from Figs. 23 and 24, respectively, plotted
in the form $P(0)/\Delta P(\phi)$ versus ϕ^2. When plotted in this form, Eq. (62) becomes
a straight line. Fits to the data shown in the figures are determined using
the method of least squares. Table IV shows the tabulated values for slope
and intercept along with the corresponding standard deviations.

Ideally, the measured slope and intercept values serve to determine
$(\Delta P/P)_{max}$ and a. However, the negative value for the intercept found
in all cases is unphysical. The experiment simply cannot be used to determine
the on-axis scattering to any useful degree of accuracy. The best that
can be done is to use the slope information to obtain the combination of parameters
$(\Delta P/P)_{max}/(k_o a \pi/180)^2$. If we refer to this combination as $Q(L)$, where L
is the coupling prism separation, then the waveguide contribution to scatter-
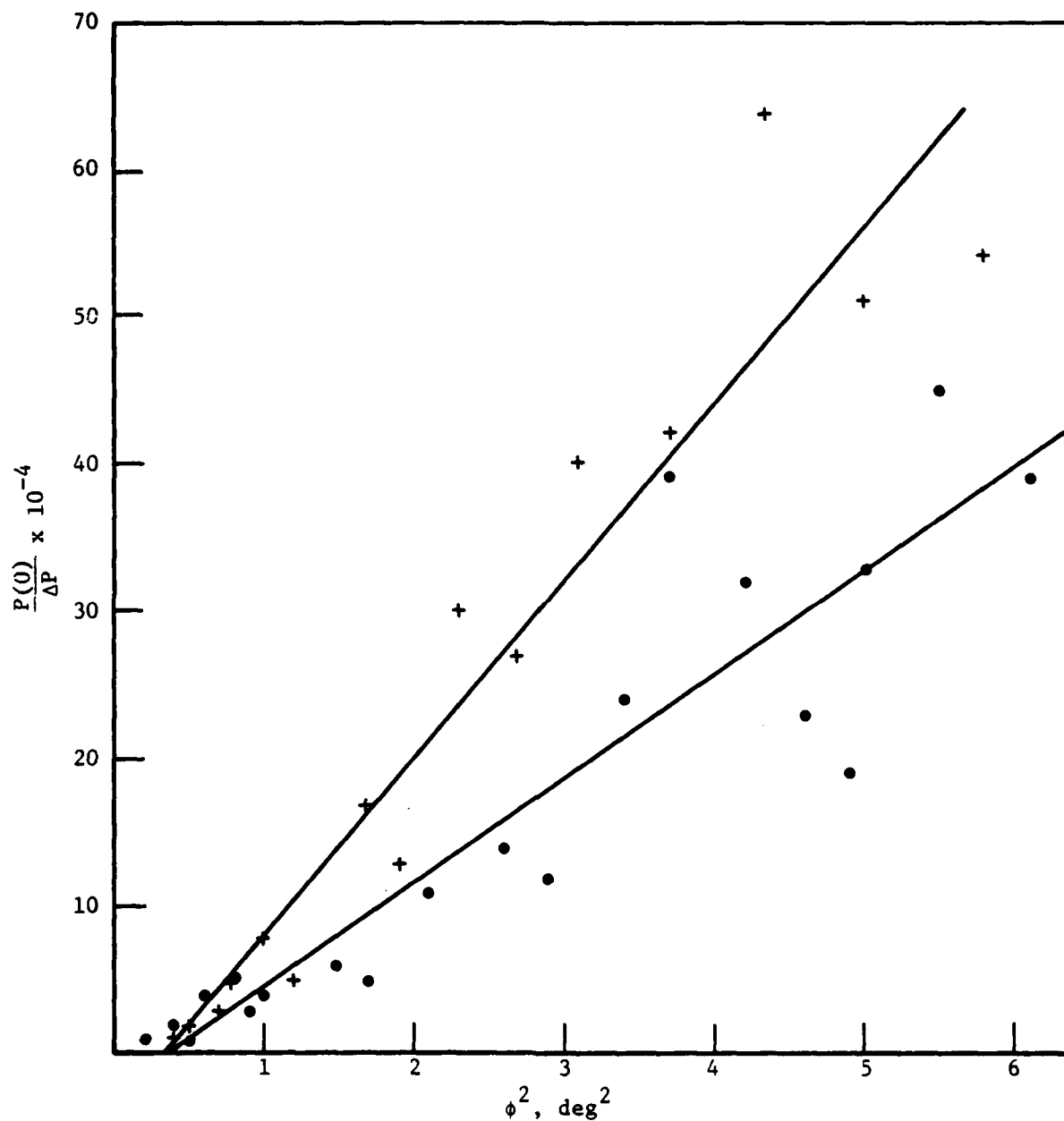ing at large angles is

Figure 25. Least squares analysis of scattering data presented in Figure 23. +, prism separation of 1 mm; •, prism separation of 53 mm.
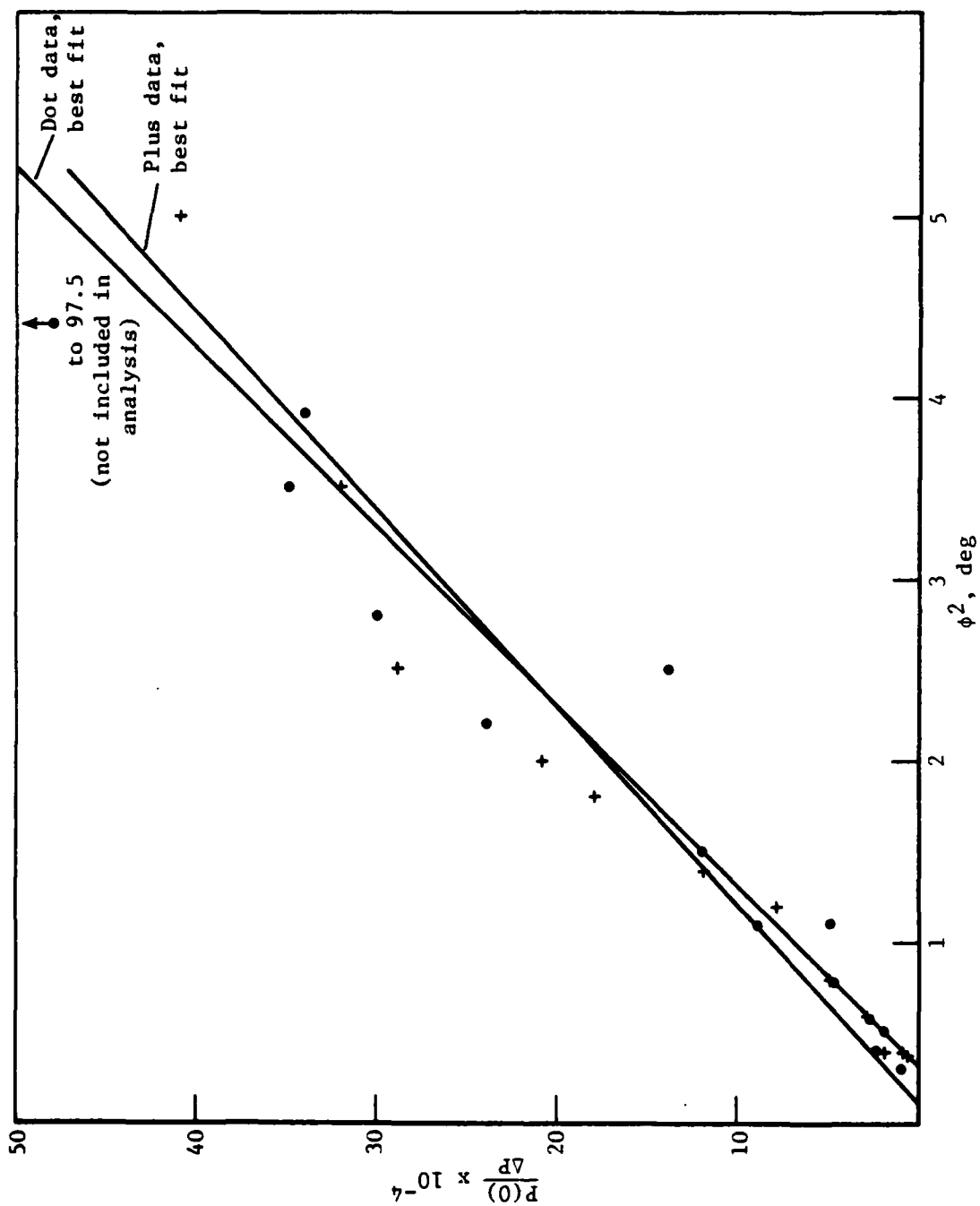
Figure 26. Least squares analysis of scattering data presented in Fig. 24
+, Prism separation of 1 mm; ●, prism separation of 52 mm.

TABLE IV. SCATTERING PARAMETERS FOR WESTINGHOUSE WAVEGUIDE W-1

Date of Experiment	Referenced Figures	Prism Separation (mm)	Intercept $10^{-4} \times [(\Delta P/P)_{max}]^{-1}$	Slope $10^{-4} \times (k_o a \pi/180)^2/(\Delta P/P)_{max}$
Sept. 25, 1981	23,25	53	-2.32 ± 2.36	7.00 ± 0.76
Sept. 29, 1981	23,25	1	-3.76 ± 2.96	11.90 ± 1.03
Nov. 24, 1981	24,26	52	-3.01 ± 1.97	10.09 ± 0.94
Nov. 25, 1981	24,26	1	-0.98 ± 1.45	9.19 ± 0.67

70

$$\Delta P(\phi)/P(0) \simeq (2/\pi)^{1/2}(\lambda_o/n)[(L_{max}-L_{min})/W]\Sigma\sigma(0)/(k_o a\pi/180)^2\phi^2$$

$$\simeq [Q(L_{max}) - Q(L_{min})]/\phi^2 \tag{63}$$

In this expression L_{max} is 52 or 53 mm and L_{min} is 1 mm. Comparison of Eq. (63) with our experimental results enables us to calculate $\Sigma\sigma(0)/a^2$. For the first run made with waveguide W 1, we find $\Sigma\sigma(0)/a^2 = 6.18 \times 10^{-8}$ μm^{-3}. For the second run, we obtain the unphysical result $\Sigma\sigma(0)/a^2 = -1.04 \times 10^{-8}$ μm^{-3}. However, if we use Q-values removed one standard deviation from the best value, we can obtain a positive result; namely $\Sigma\sigma(0)/a^2 = 0.84 \times 10^{-8}$ μm^{-3}. The smallest value of $\Sigma\sigma(0)/a^2$ obtained for the first run using Q-values within one standard deviation of the best values in $\Sigma\sigma(0)/a^2 = 3.88 \times 10^{-8}$ μm^{-3}. The inconsistencies in the two runs may result from changes in the prism contribution to scattering resulting from different prism placements.

Figure 27 shows the predicted IOSA dynamic-range variation with scattering-center size a, obtained using the average value for the two runs, $\Sigma\sigma(0)/a^2 = 2.57 \times 10^{-8}$ μm^{-3}, corrected *for the longer wavelength* used in the IOSA. The requirement for meeting the 40 dB dynamic range specification is that a be less than about 50 μm. Our only evidence for the value of a is from data like that in Fig. 19, which is rendered uncertain by the random fluctuations in the scattered intensity and by the pseudo-scattering associated with nonuniform coupling efficiency. However, all data of this type is consistent with values of a in the range 14 μm – 50 μm, with $a = 25$ μm being an average over nine different runs using seven different samples. The conclusion derived from Fig. 27 is that the IOSA dynamic range will be about 42 dB, or 2 dB greater than specifications require. Although this result is encouraging, we note that the $\pm$ 5 dB error bars shown in the figure, based on the uncertainties in determining $\Sigma\sigma(0)/a^2$ are critical. In the worst case situation, the 40 dB dynamic range is not met for $a > 12$ μm.

Battelle Sample #226

In order to provide a comparison between waveguides fabricated at different facilities Battelle sample #226 was subjected to the same experimental procedures that lead to the results in Figs. 23 and 24. This waveguide
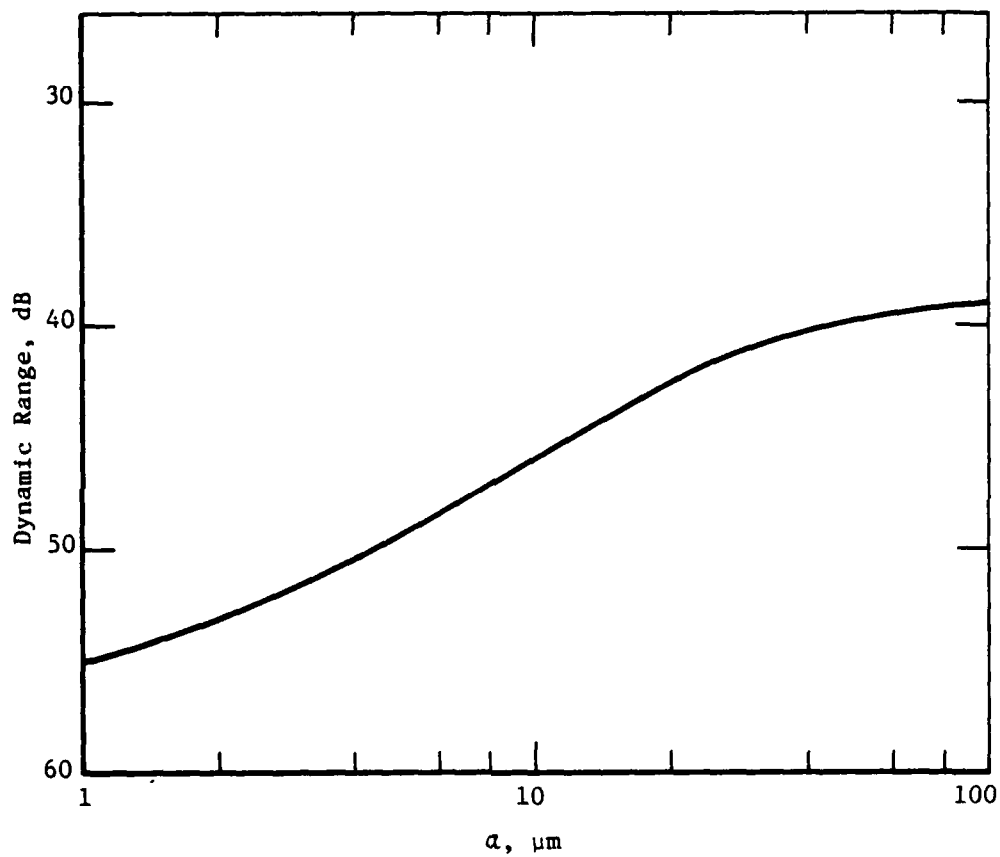
Figure 27. IOSA dynamic range versus scattering-center size
a, based on the results of Table IV for sample
W1.

was formed using ∼175 A of Ti diffused for 2.5 h at 965°C in moist flowing oxygen.[15] This fabrication procedure is now used routinely for most Battelle device-oriented integrated optics programs. The surface quality of samples fabricated in this way is usually very good in that the often encountered orange peel texture of the diffused surface is absent. Sample 226 was found to be particularly good in this regard.

The experimental data for relative scattered power versus scattering angle is plotted in Fig. 28. For this data an aperture was inserted in the beam to block the background scattered light. Accordingly, the results should be valid over the full angular range examined. We find a clear increase in scattering associated with a longer waveguide path length for scattering angles in the range 0.5-2.2°. However, outside this interval the data are fairly well intermixed.

We have analyzed the results to determine the best Lorentzian fits to the data over a specified angular range. Two different angular ranges were selected. For $0.5° < \phi < 2.45°$ the data shows a definite excess of scattered power associated with a longer waveguide path length. For results in this interval the best fitting slopes of the $P(0)/\Delta P$ versus ϕ^2 curves were used to obtain $\Sigma\sigma(0)/a^2 = 2.04 \times 10^{-6}$ μm^{-3}. This is nearly two orders-of-magnitude larger than the value obtained for W-1, indicating that IOSA dynamic range with the Battelle sample would be nearly 20 dB worse than the value obtained from Fig. 27 for the Westinghouse sample.

However, we know of no experimental reason for limiting analysis to angles less than 2.45°. When we analyze all data in the range $0.5° < \phi < 6°$, the best fitting slopes of the $(P/\Delta P)$-versus-ϕ^2 curves indicate a value $\Sigma\sigma(0)/a^2 = 4.10 \times 10^{-8}$ μm^{-3}. This is only a factor 1.6 larger than we obtained with W-1. As with W-1, a value of zero scattering may be consistent with the data if the true slopes of the $P/\Delta P$ versus ϕ^2 curves are within one standard deviation of the statistically determined best values. It is simply not possible to state with confidence whether the waveguides are good enough for the IOSA application, or even whether the Westinghouse fabrication methods are to be preferred over the Battelle methods.

73

was formed using ∿175 A of Ti diffused for 2.5 h at 965°C in moist flowing oxygen.[15] This fabrication procedure is now used routinely for most Battelle device-oriented integrated optics programs. The surface quality of samples fabricated in this way is usually very good in that the often encountered orange peel texture of the diffused surface is absent. Sample 226 was found to be particularly good in this regard.

The experimental data for relative scattered power versus scattering angle is plotted in Fig. 28. For this data an aperture was inserted in the beam to block the background scattered light. Accordingly, the results should be valid over the full angular range examined. We find a clear increase in scattering associated with a longer waveguide path length for scattering angles in the range 0.5-2.2°. However, outside this interval the data are fairly well intermixed.

We have analyzed the results to determine the best Lorentzian fits to the data over a specified angular range. Two different angular ranges were selected. For $0.5° < \phi < 2.45°$ the data shows a definite excess of scattered power associated with a longer waveguide path length. For results in this interval the best fitting slopes of the $P(0)/\Delta P$ versus ϕ^2 curves were used to obtain $\Sigma\sigma(0)/a^2 = 2.04 \times 10^{-6}$ μm^{-3}. This is nearly two orders-of-magnitude larger than the value obtained for W-1, indicating that IOSA dynamic range with the Battelle sample would be nearly 20 dB worse than the value obtained from Fig. 27 for the Westinghouse sample.

However, we know of no experimental reason for limiting analysis to angles less than 2.45°. When we analyze all data in the range $0.5° < \phi < 6°$, the best fitting slopes of the $(P/\Delta P)$-versus-ϕ^2 curves indicate a value $\Sigma\sigma(0)/a^2 = 4.10 \times 10^{-8}$ μm^{-3}. This is only a factor 1.6 larger than we obtained with W-1. As with W-1, a value of zero scattering may be consistent with the data if the true slopes of the $P/\Delta P$ versus ϕ^2 curves are within one standard deviation of the statistically determined best values. It is simply not possible to state with confidence whether the waveguides are good enough for the IOSA application, or even whether the Westinghouse fabrication methods are to be preferred over the Battelle methods.
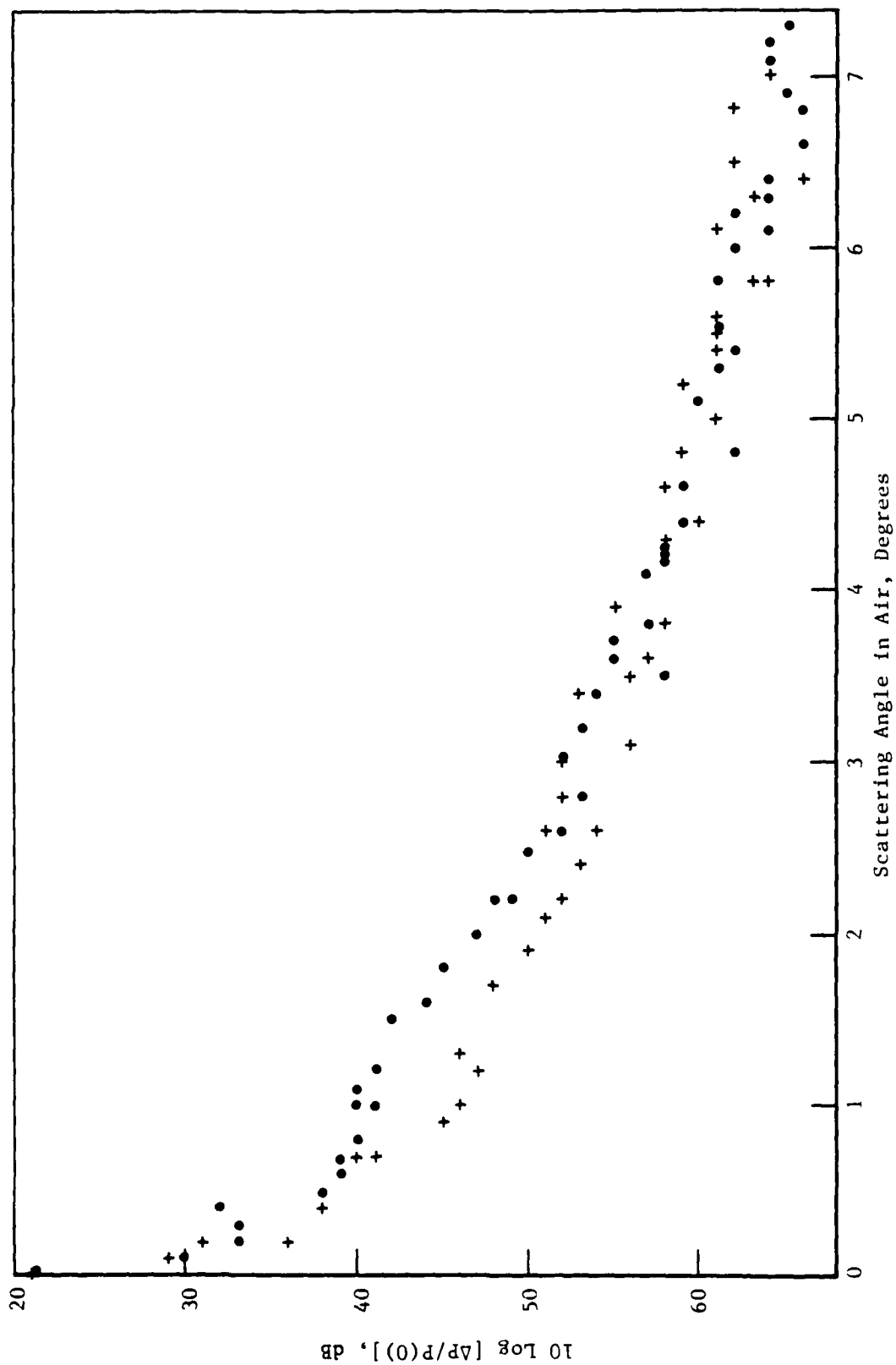
Figure 28. Normalized scattered power versus scattering angle for the TM_O mode of sample 226. Dots correspond to 14 mm prism separation. Pluses correspond to 1 mm prism separation.

74

To further illustrate the problem, Fig. 29 shows data obtained using Battelle sample 166, from which the results of Fig. 19 were obtained using a different experimental technique. Three different prism separations were used in obtaining the data in Fig. 29, 1 mm, 16 mm, and 11 mm. The last separation was motivated by the high scattering observed at 16-mm separation. It was suspected that prism placement was contributing an anomalously large amount of scattering to the observation. Judging from the results of Fig. 29, this was apparently the case. However, the scattering at 11-mm separation is anomalously low compared not only to the 16-mm result but also to the 1-mm result. For this reason, we made no attempt to statistically analyze the data.

Surface Degradation From Low-Temperature Annealing

In the course of working with the various samples of the program, a previously unobserved source of scattering came to our attention. We had noted early in the program that of the two nominally identical samples sent to us by Westinghouse, one was of decidedly superior quality as judged by in-plane scattering levels. This is the sample called W-1 that we have used to take the majority of data reported here. Late in the program we subjected the sample to a series of thermal anneals to erase the effects of optical damage which may have been generated in the course of previous experiments. The first anneal consisted of a 15 minute heat treat in flowing O_2 at 200°C. The sample was allowed to cool at the natural rate of the oven, and in-plane scattering data taken with 1 mm prism separation showed no ill effects produced by the anneal.

Later a second anneal was performed under identical conditions except that the sample was eased from the hot zone at the rate of about one inch per ten minutes. Figure 30 shows the subsequent intensity profile of the focused beam after the anneal in comparison to its previous appearance.

After a third anneal (200°C, 25 min, flowing O_2) a pinging and crackling sound was heard during withdrawal conducted at the rate 1 inch per 15 min. In a fourth anneal, the withdrawal rate was increased near the end (30°C down to room temperature) and the crackling sound was observed to occur in coincidence with this.

No damage to the crystal surface was apparent to the unaided eye at this time. Subsequently a fifth anneal was performed at 500°C for 1 hour in
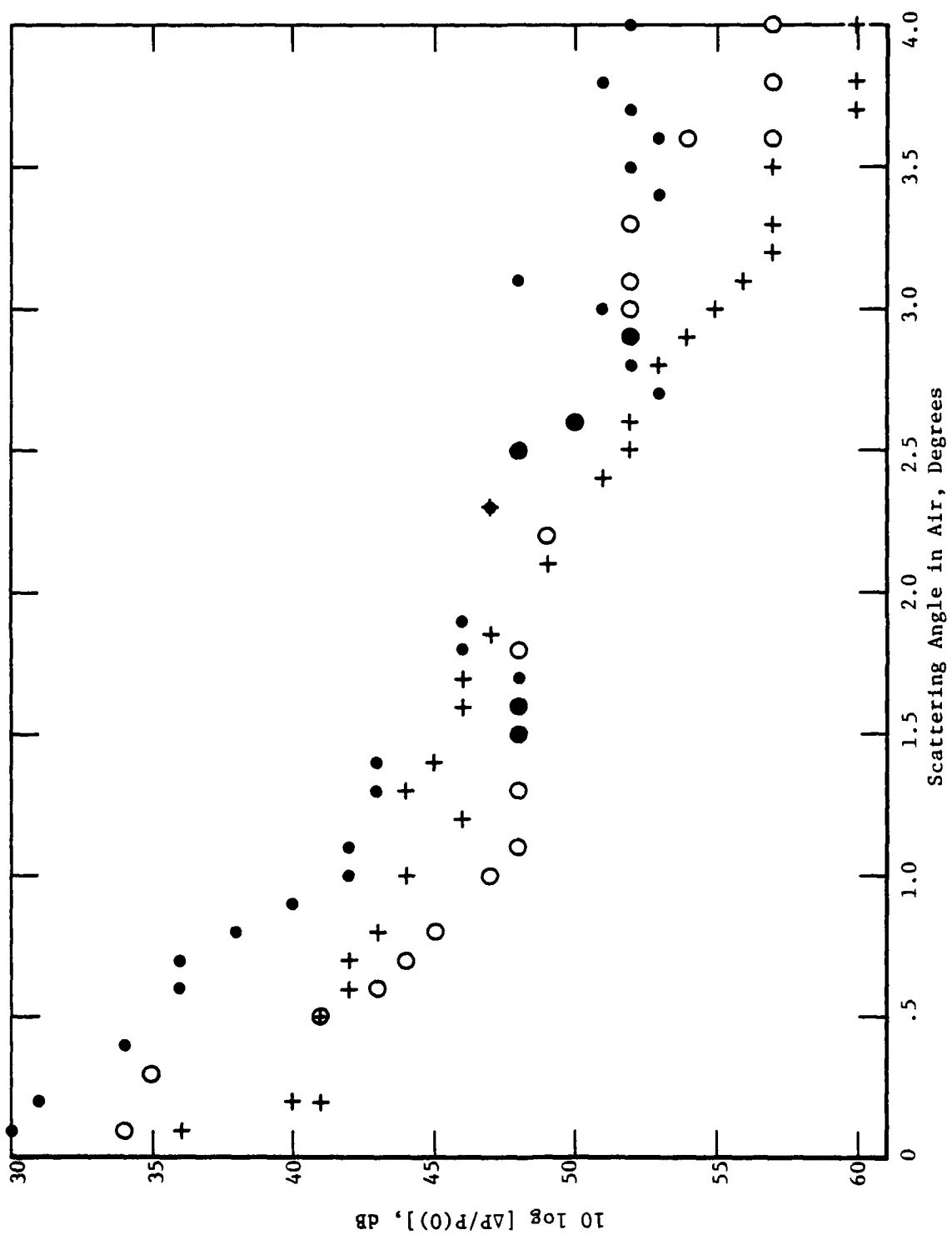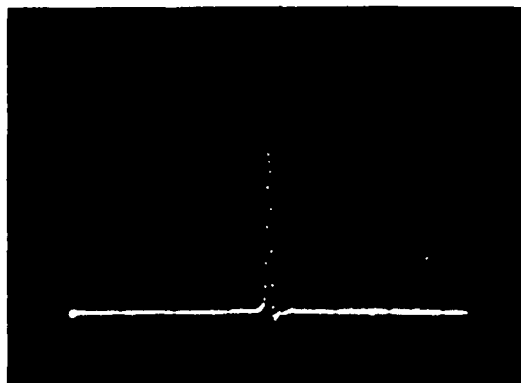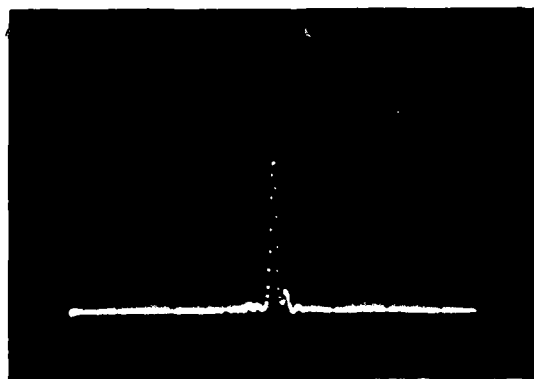
Figure 29. Normalized scattered power versus scattering angle for the TM_0 mode of sample 166. + = 1 mm prism separation. ● = 16 mm separation. O = 11 mm separation.

(a)

(b)

Figure 30.   Intensity profile (linear scale) of focused beam
passed through sample W1.   (a)   Before anneal
treatments (b) after two anneals.

flowing O_2, followed by an overnight cool at the natural rate of the oven. The idea here was that a reversible phase transformation could have occurred at the low temperature anneals, and that a longer, higher temperature anneal might restore the crystal to near its original state.

Figure 31 shows the in-plane scattered energy distribution for the sample after this heat treatment in comparison to previous results that were plotted in Fig. 24. It is apparent that significant degradation of the waveguide has occurred from the five heat treatments. Figure 32 shows a micrograph of the waveguide surface taken at this time that verifies this. Also shown is a micrograph of the surface of sample W-2. It is likely that same phenomena at work in the low temperature anneals of W-1 was operative during the fabrication of sample W-2. The implication is that care must be taken in using the Westinghouse fabrication technique. Since Battelle samples have not shown this problem and since the main difference between the Battelle and Westinghouse fabrication methods is the use, at Westinghouse, of a $LiNbO_3$ - powder environment to prevent outdiffusion, we speculate that this environment is the source of the problem.

Although we did not subject Battelle samples to the same anneal schedule that we used for W-1, a general observation is that outdiffusion prevention using flowing H_2O vapor[15] leaves the waveguide surface relatively free of the often-observed orange peel texture. If, as we speculate, the presence of orange peel correlates with surface strains that are released in the low temperature anneals, fabrication methods which avoid orange peel are to be favored. Unfortunately we did not perform a careful micrographic examination of samples W-1 and W-2 when they were received to see if they had orange peel. Because of this and because we did not subject sample 226 to the same anneal schedule as W-1, we do not have a sufficient set of evidence from which to draw definite conclusions, but we believe that our speculations warrant attention. For completeness we note that the data in Fig. 28 for Battelle sample 226 was obtained following a low-temperature anneal, but it is not known whether the sample was cooled rapidly enough to provide an adequate test for thermal stability.
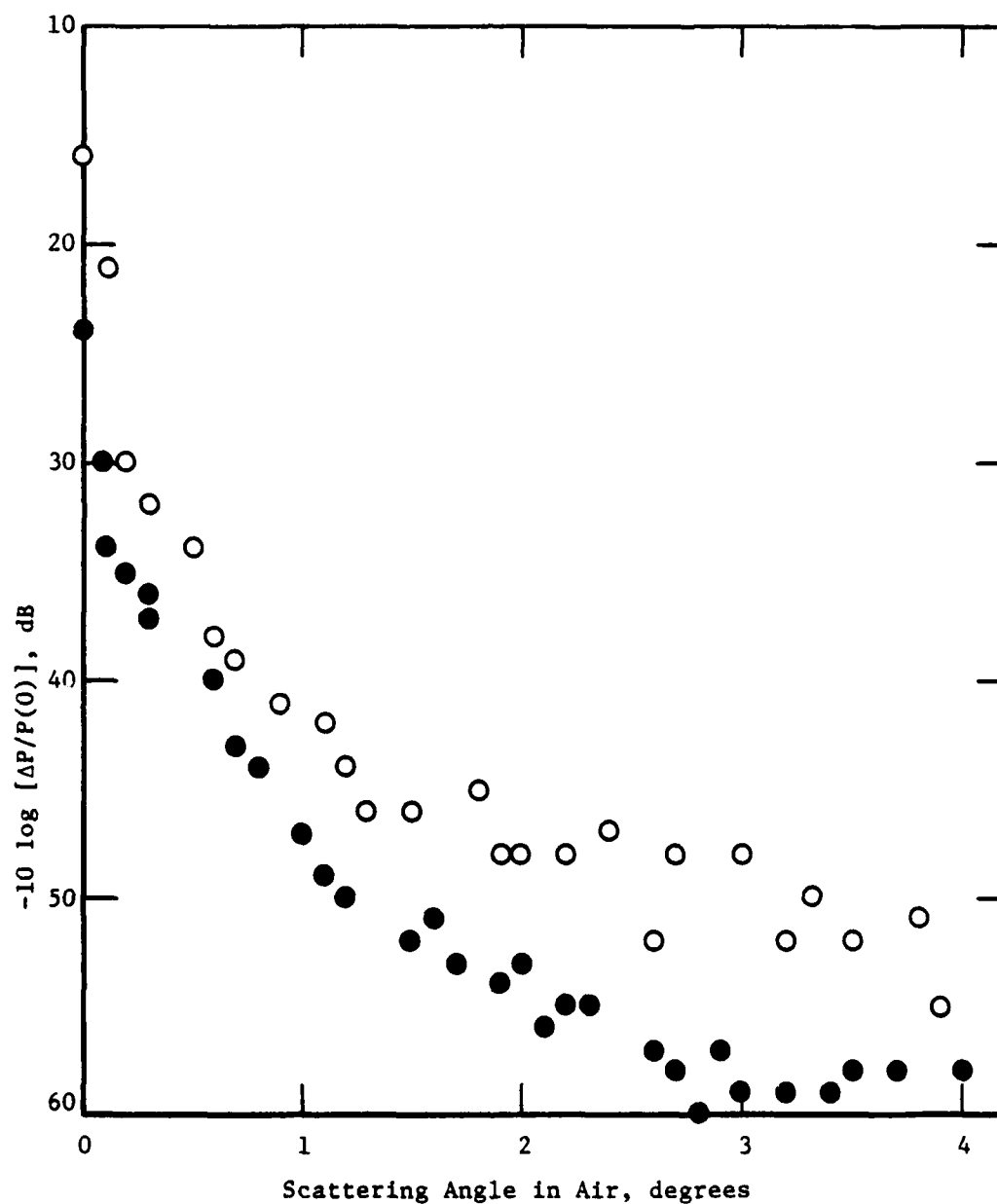
Figure 31. Comparison of scattering in sample W-1 before and after five low-temperature anneals. Closed circles: before annealing (waveguide path = 52 mm). Open circles: after annealing (waveguide path = 57 mm).

c-axis

←——— 50 μm ———→

(a)

c-axis

←——50 μm——→
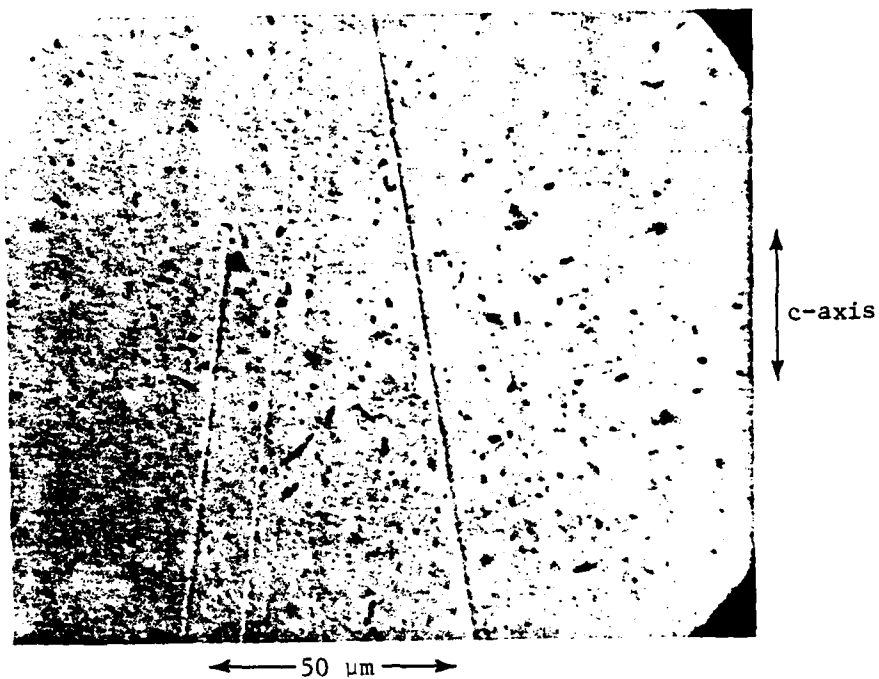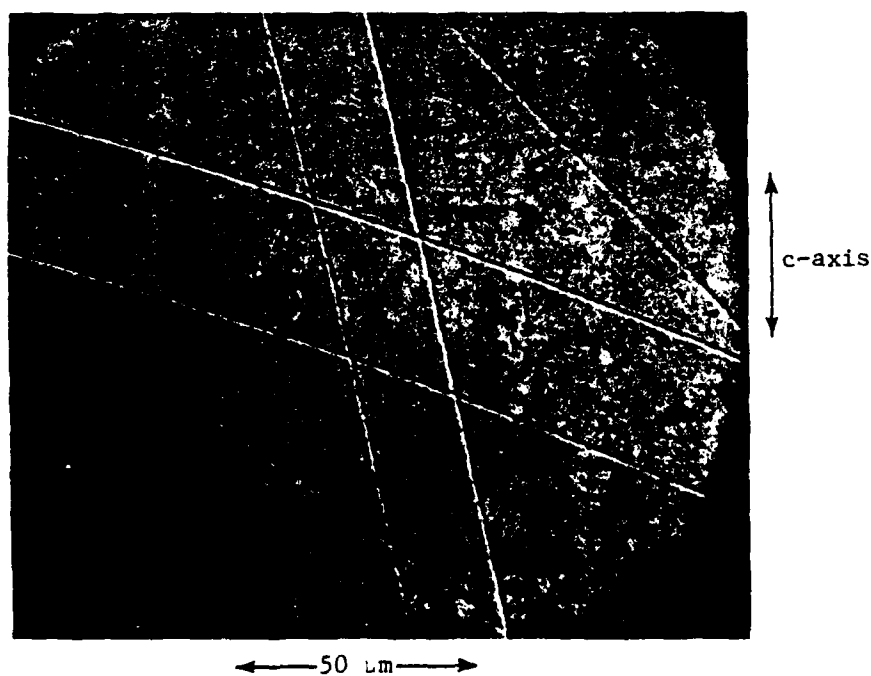
(b)

Figure 32. Micrographs of the surface of the Westinghouse samples.
(a) Sample W-1, after five low-temperature anneals.
(b) Sample W-2, after one low-temperature anneal.

80

OTHER IN-PLANE SCATTERING EXPERIMENTS

The Use of End-Fire Input and Edge Output Coupling

Other experiments to measure in-plane waveguide scattering were per-
formed using different geometries to circumvent the problem of scattering from
prism coupling. The obvious modification of this type involves the use of end-fire
coupling to replace prism coupling. However, imperfect polishing of the edges
leads to scattering that is in its effect no different than that associated
with prism coupling. If the edge has an rms roughness σ and an autocorrela-
tion length a, an analysis similar to that used for the derivation of Eq. 38
shows that the associated scattered-power distribution is given by

$$\Delta P/P(0) = (16/\pi) \ k_o^2(n-1)^2\sigma^2(a/W)L(k_o a\phi). \tag{64}$$

For $k_o = (2\pi/0.83) \ \mu m^{-1}$, $a = 20 \ \mu m$, $W = 4$ mm, and $n = 2.2$, an on-axis scatter-
ing level of 30 dB is consistent with a surface roughness of $\sigma = 262$ Å. This
is much rougher than the levels that may be achieved in polishing flat surfaces
of $LiNbO_3$.[11] However, the special problems encountered in polishing sharp edges
on the material may lead to roughness values of this magnitude.

We have performed the experimental comparison in which a focused
beam was end-fired into Westinghouse sample W1 and output coupled using either
a prism or diffraction from the polished waveguide termination edge. The
experimental geometry is shown in Fig. 33 for the case of prism output coupl-
ing. The results of the comparison experiment are displayed in Fig. 34. It
is evident that scattering from polished-edge output coupling is greater than
that from prism output coupling. As a result of this measurement, we did not
further investigate the former output-coupling method. The theoretical curve
for the case of prism output coupling will be discussed in the following
paragraphs.

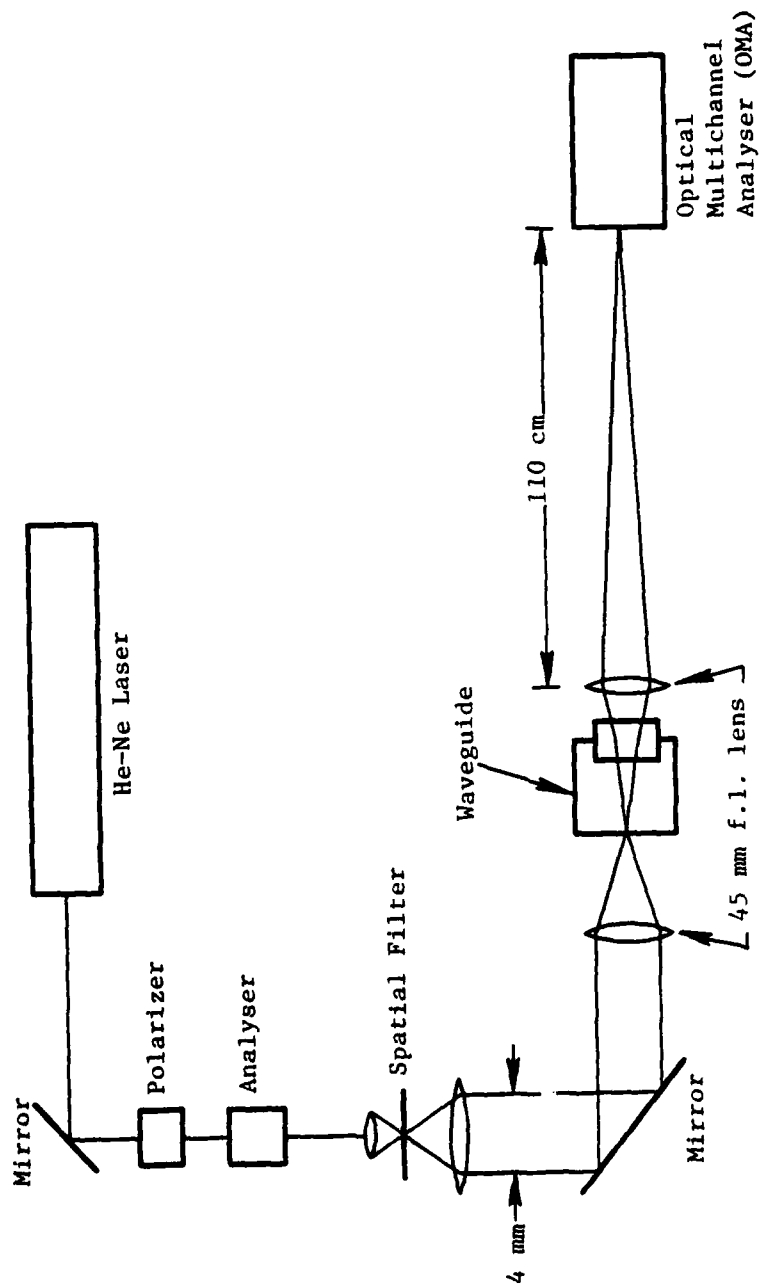Figure 33. Schematic diagram of experimental set up using end-fire input coupled light to avoid effects of prism-associated scattering. Output beam is either prism coupled (as shown) or edge coupled.
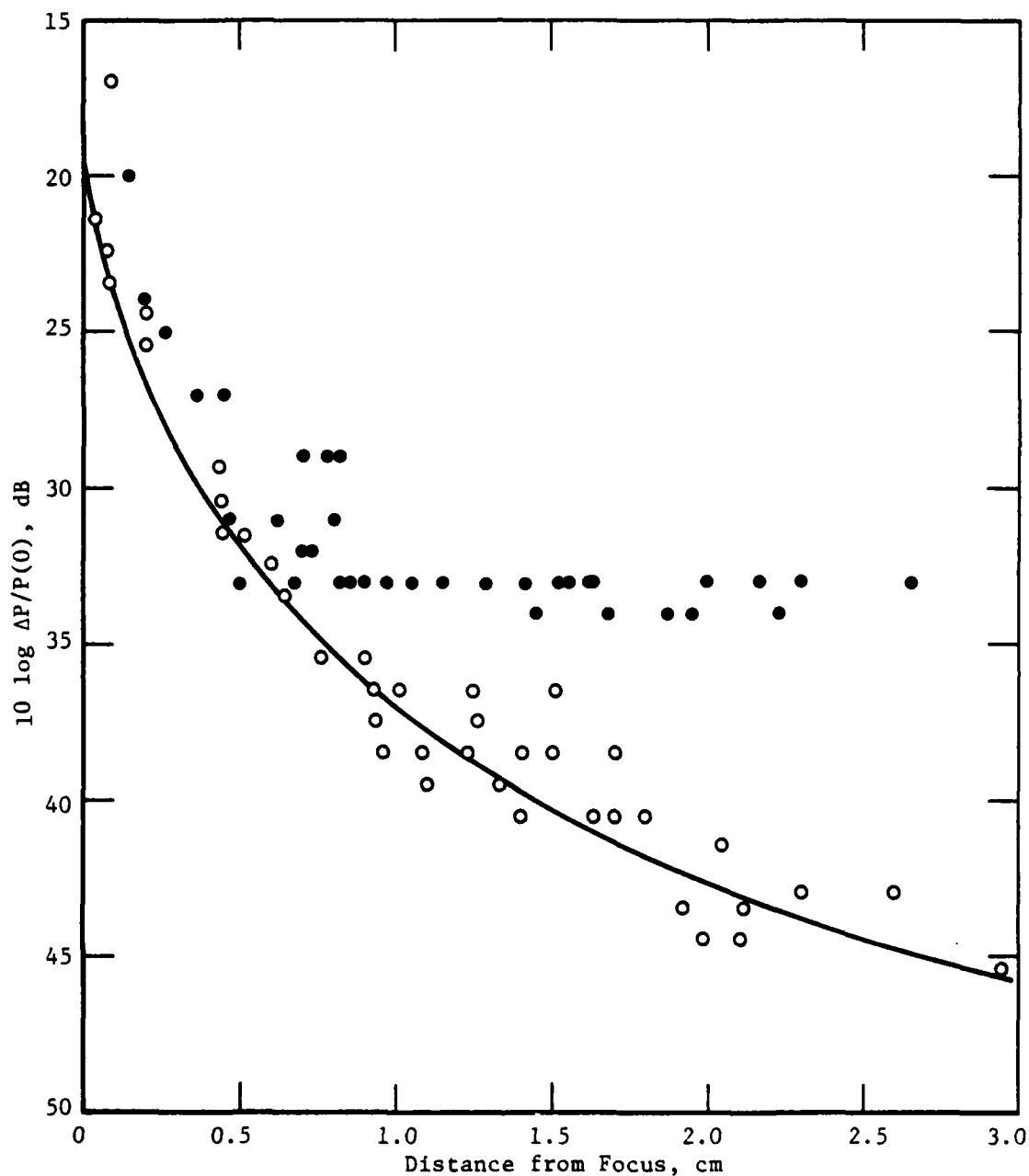
82

Figure 34. Effect of output coupling method on scattered energy
distribution. ●, End-fire input and edge output cou-
pling. o, End-fire input and prism output coupling.
Experimental geometry is that of Figure 33.

83

The Image Geometry for Studies of In-Plane Scattering

From Fig. 33, it may be noted that the focused beam incident on the detector is really an image of the focused beam coupled into the waveguide. This is distinguished from the conventional measurement using a collimated input beam, in which case the focused beam at the detector is a Fourier transform of the input beam.

The significance of this is illustrated in Fig. 35. In the Fourier-transform geometry, all rays scattered at the same angle are projected to the same off-axis position y in the focal plane. Because of this feature, the shape of the scattering cross section is known directly from the shape of the scattered-energy distribution. This feature is absent in the imaging geometry, because the position y to which a given scattered ray is projected depends not only the angle of scattering but also on the location of the scattering center in the waveguide. This makes it necessary to do a bit of modeling to extract scattering parameters from the data; however, an advantage is that rays scattered from the *point of input coupling* are imaged to y = 0 and do not contribute to the scattered m-line distribution. This enables us to eliminate background scattering from input coupling from our measurement, and is very useful if output coupling can be accomplished with little additional scattering added to that from the waveguide. Assuming that this is a possibility, we made a careful analysis of those results in Fig. 34 obtained using prism output coupling, and we also employed the image geometry to study other waveguide samples as well.

Interpretation of Image-Geometry Results

The analysis to determine scattering center parameters from image-geometry results is similar to that employed to calculate the scattered signal from the regions of the IOSA where the guided beam is either converging or diverging (regions A and D of Fig. 1). The approach is to divide the beam path in the waveguide into increments of area and to calculate the scattered power from each increment received at a selected pixel in the detector array. The total power is calculated by integrating over all increments of area in
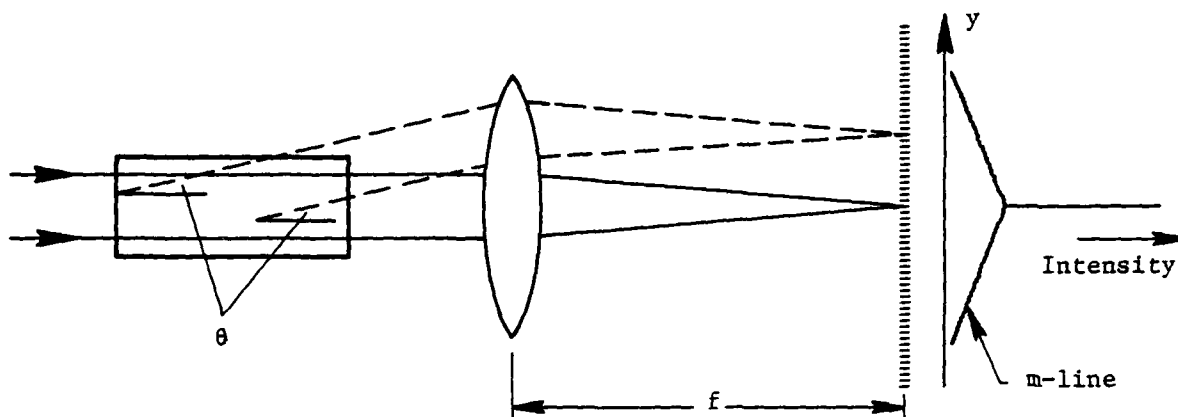
(a)
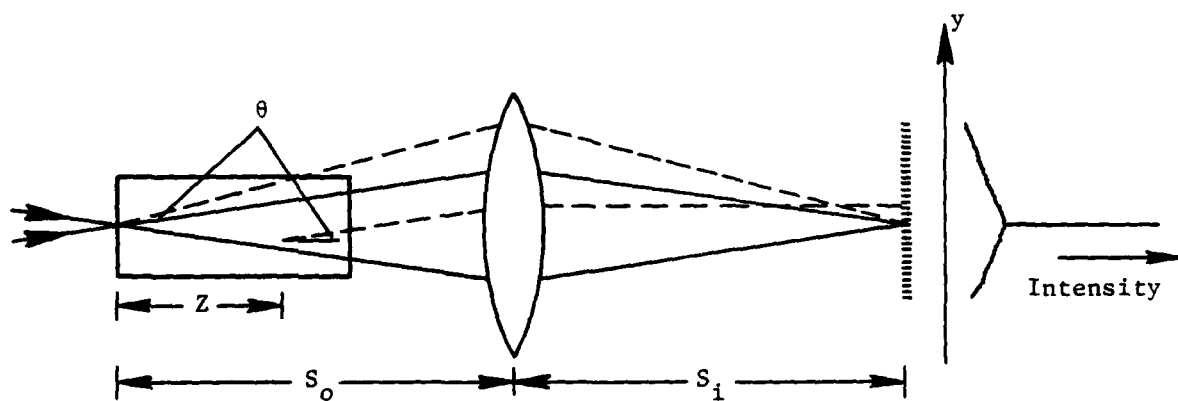
$$1/S_o + 1/S_i = 1/f$$

(b)

Figure 35. (a) Conventional Fourier – transform approach for measuring
in-plane scattering, in which all rays scattered at angle θ
are projected to the same point on the m-line. (b) Imaging
method for measuring in-plane scattering, in which rays scat-
tered at the point of input coupling ($Z = 0$) do not contrib-
ute to the measured m-line.

the beam path. If the pixel has an aperture Δy and is a positive distance y from the optical axis, the received power in the case of RGD scattering centers is

$$\Delta P = P_o \Sigma\sigma(0) M^{-1} \ [y(I_+ - I_-) + (\Delta y/2) \ (I_+ + I_-)]$$

$$I_\pm = I[(ka/L)(y \pm \Delta y/2)/M]$$

$$I(u) = u^{-1} \tan^{-1} u + \ell n(1 + u^{-2})^{1/2}. \qquad (65)$$

In this expression P_o is the total power and $M = S_i/S_o$ is the magnification associated with the imaging geometry, approximately equal to 25 in our experiments.

For all values of y that we measured, an excellent approximation to Eq. 65 is

$$\Delta P \simeq P_o \ \Sigma\sigma(0) \ M^{-1}\Delta y \ \ell n[1 + (ML/ka y)^2]^{1/2} \qquad (66)$$

The ratio of scattered power to the peak, on-axis unscattered power is

$$\Delta P/P(0) = (2/\pi)^{1/2} \ (F\lambda_o/W) \ \Sigma\sigma(0) \ \ell n[1 + (ML/ka y)^2]^{1/2} \qquad (67)$$

The theoretical curve in Fig. 34 is based on the parameter values $\Sigma\sigma(0) = 0.51 \ \text{mm}^{-1}$ and $a = 16.5 \ \mu m$. The range of data acquired is sufficiently large that values for both parameters can be obtained separately, rather than in the combination $\Sigma\sigma(0)/a^2$, as was the case with the Fourier-transform geometry. However, when we calculate the ratio using the above values for $\Sigma\sigma(0)$ and a, we obtain $1.87 \times 10^{-6} \ \mu m^{-1}$. This is about two orders of magnitude greater than we achieved using the Fourier transform geometry. We were never able to resolve why the scattering should be so much greater for the image geometry, and we abandoned it as a measurement technique later in the program.

IOSA DYNAMIC-RANGE FORECAST

The IOSA dynamic range specifications are prescribed at the fourth off-axis pixel on either side of a central illuminated pixel. This has been taken into account in generating previous figures in which dynamic range has been plotted against various scattering parameters. It is important, however to know how the dynamic range behaves as a function of pixel number, given the scattering parameters measured in this program. The information is provided here. We emphasize that the calculations are only as good as the measurements, and the measurements were plagued with experimental uncertainties from background scattering that were not successfully resolved. Consequently the results are best estimates that may or may not hold up as spectrum analyzers are actually made and tested.

The relation to be plotted is $10 \log [\Delta P(m)/P]$ versus m, where $\Delta P_{tot}(m)$ is the total scattered power received at pixel m and P is the power launched into the waveguide mode. The ratio $\Delta P(m)/P$ is calculated from IOSA design and scattering parameters according to Eq. 25. Values for these are listed in Table V. The design parameters are relevant to the Westinghouse IOSA effort,[4] while the scattering parameters are those obtained for sample W-1.

With regard to specification of the scattering parameters, a word of explanation is in order. For two different runs we found $\Sigma\sigma(0)/a^2 = (6.2 \pm 2.4) \times 10^{-8} \ \mu m^{-3}$ and $(-1.0 \pm 1.9) \times 10^{-8} \ \mu m^{-3}$. Assigning equal weight to each run, the average is $2.6 \times 10^{-8} \ \mu m^{-3}$. The standard deviation calculated from the input standard deviations is $2.2 \times 10^{-8} \ \mu m^{-3}$ while that calculated from the two point sample population is $5.0 \times 10^{-8} \ \mu m^{-3}$. If we base our calculations of IOSA dynamic range on the average $\Sigma\sigma(0)/a^2 = 2.6 \times 10^{-8} \ \mu m^{-3}$, there is a reasonable chance that our calculated dynamic range values are too high by 3 to 5 dB, depending on which value for standard deviation we select. Equally consistent with our results is the possibility that our calculated values are too low by the same amount. The possibility that the waveguide scattering is acutally zero is also consistent with our results; however, the preponderance of our data taken over three years shows an average scattering greater than zero. Therefore, we are inclined to minimize this possibility. Error bars of $\pm$ 5 dB shown in the figures are based on these deliberations.

TABLE V.   DESIGN AND SCATTERING PARAMETERS USED TO
           CALCULATE SCATTERING LIMITATIONS TO IOSA
           DYNAMIC-RANGE

Lens Focal Length	F	27.2 mm
Lens-Lens Separation	L	18.0 mm
Detector Aperture and Spacing	δY	12.0 μm
Diffraction Angle	ψ	0.066 radians
Diffraction Efficiency	η	0.05
Free-Space Wavelength	λ_o	0.83 m
Refractive Index	n	2.2
Scattering Parameter	$\Sigma\sigma(0)/a^2$	1.15×10^{-8} μm^{-3}

In Table V the value for $\Sigma\sigma(0)/a^2$ have been corrected for the fact that the IOSA will operate with light of 0.83 μm wavelength. Our experiments were performed at 0.633 μm, and for RGD scattering, $\sigma(0)$ is proportional to λ^{-3} as described by Eq. 39. Therefore $\Sigma\sigma(0)/a^2 = 2.6 \times 10^{-8} \times (0.633/0.83)^3 = 1.15 \times 10^{-8}$ μm^{-3}. This value is used in Table V. Note that in general there will be a wavelength dependence of the index parameter δn_g which is an important factor in Eq. 39. However, we have neglected this possibility in our analysis. The results of our analysis are shown in Fig. 36, where dynamic range versus pixel number is plotted with scattering center size as a parameter. The range of scattering center size selected, from 10 to 50 μm, is consistent with our experimental evidence. Interestingly, dynamic range is not sensitive to this parameter at large pixel numbers. Also note the slight asymmetry in the curves associated with the contribution to scattering from the 0-order undiffracted beam. This beam is focused at a position corresponding to pixel position 150. Owing to the rapid fall off of scattered intensity with scattering angle for RGD scattering centers, the contribution from this source is not significant even though it carries 95% of the total unscattered IOSA beam power.

These results suggest that the IOSA dynamic range specifications are met by sample W-1 and the Westinghouse design. Even in the worst case represented by the ± 5 dB error bar in Figure 36, 40 dB dynamic range is achieved at the eighth off-axis pixel.
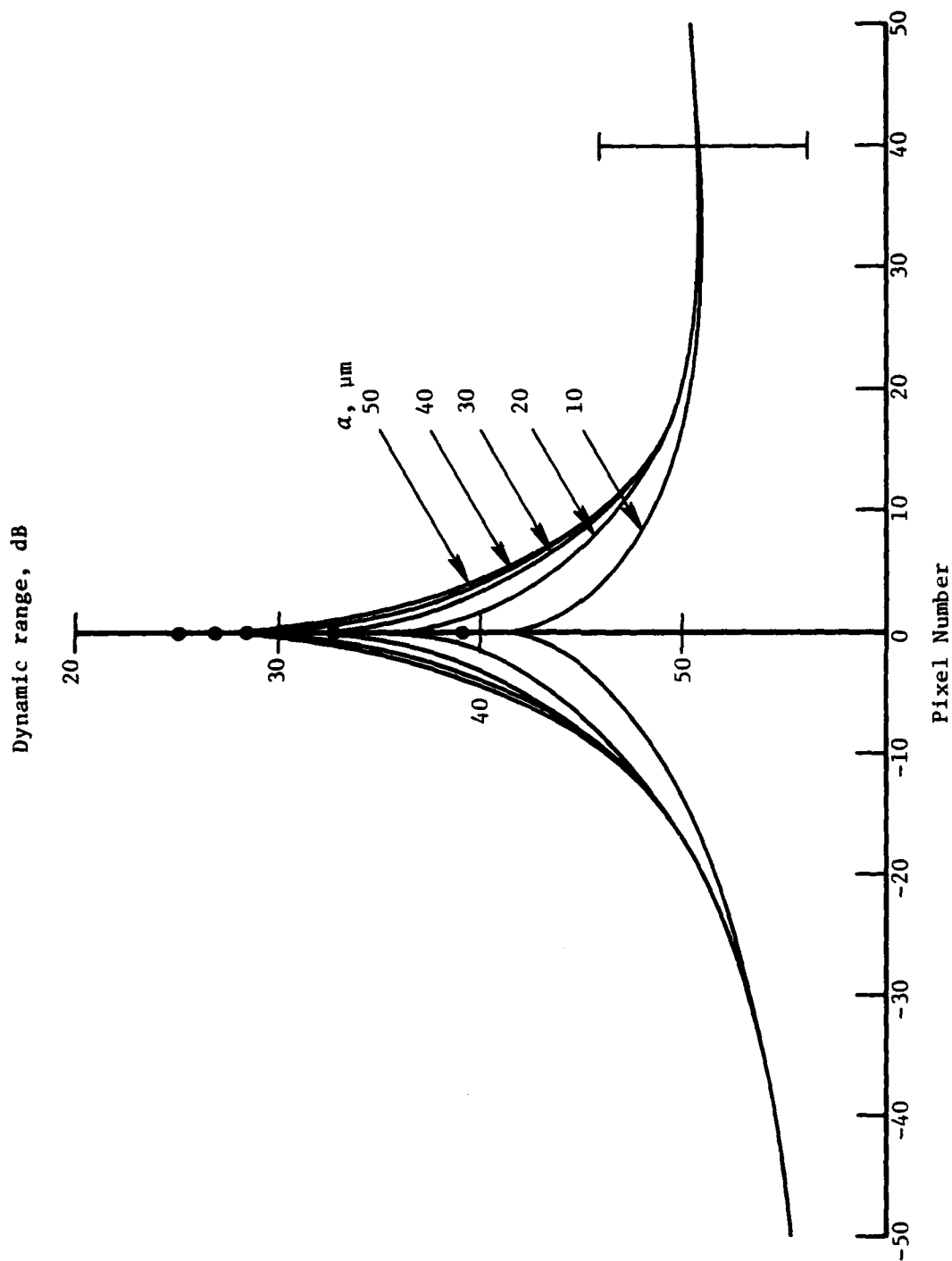
Figure 36. IOSA dynamic range versus pixel number with scattering center size as a parameter. The curves are based on the Westinghouse design and waveguide scattering results shown in Table V. An error bar indicates the amount each curve may be raised or lowered to account for experimental uncertainties in the measurement of $\Sigma\sigma(0)/a^2$.

V. SUMMARY AND CONCLUSIONS

This report has described the results of a research program to characterize and reduce the effects of scattering in Ti-diffused LiNbO$_3$ waveguides. This research has been performed for the Naval Research Laboratories to extend the results of two previous programs on the same subject conducted for the Air Force.[11] The extent of government support shows the perceived importance of scattering to the success of planar integrated optics as a signal-processing technology. All who have been involved with the technology and the problem of scattering have appreciated its difficulty. We nevertheless expected that the results of this work, as exemplified by Fig. 36, would be more definitive if not more optimistic. Because of experimental problems, the program emphasized the measurement of waveguide scattering rather than the understanding of its causes and the means for its reduction. In the future, progress in these areas will come from those who, viewing scattering from a fresh perspective, discover new experimental approaches to the problem. We take considerable satisfaction in providing these workers with a sound foundation on which to base their research.

First of all, our evidence suggests the dominance of Rayleigh-Gans-Debye scattering associated with scattering centers in the size range 10-50 μm and typical effective refractive index inhomogeneity 10^{-6}. These numbers alone suggest the difficulty in directly observing the scattering centers using diagnostic tools. Our best assessment is that the scattering sources lie close to the waveguide surface and that the low value of δn_g results from their small depth normal to the waveguide plane. Two candidate mechanisms for such scattering centers are surface roughness and Li-Ti-O compound formation during diffusion. Stylus profilometers are adequate for the measurement of surface roughness and this is certainly one diagnostic approach recommended for future scattering research. SIMS analysis has been useful for verifying the occurence of anomalously high Ti levels at the waveguide surface,[2] but this technique is not likely to have the lateral resolution necessary to identify and study individual scattering sites. Nevertheless, by combining stylus measurements, SIMS measurements and in-plane scattering measurements it is believed that valid conclusions about the dominant source of scattering can be drawn. This was the plan of the current program, and it is still

91

recommended for future work if the experimental problems in generating good in-plane scattering data may be solved.

Assuming that surface-localized scattering centers are dominant in Ti-LiNbO$_3$ waveguides, scattering reduction is simply achieved by reducing the waveguide modal field value at the surface. This generally means that longer, hotter diffusion treatments produce better waveguides, other things being equal. But other things are generally not equal. Diffusion time and temperature have an effect on surface compound formation,[14] while surface-compound formation appears to have an effect on surface roughness.[11,17] Thus the interplay of phenomena is complex. Each datum point to be used in analyzing the situation requires the fabrication of a new waveguide and the subsequent performance of stylus, SIMS, and in-plane scattering measurements, for example. Thus, the approach to the problem is likely to be expensive and time consuming. Based on the limited effort of this program, we have not noticed significant differences between waveguides to result from variation of fabrication procedures, within reasonable and commonly accepted standards. One Westinghouse waveguide was superior to Battelle waveguides, but degraded as the result of a low temperature thermal anneal. Another Westinghouse waveguide was inferior to Battelle samples. In short, there has been little to recommend one fabrication technique over another.

Despite this unenthusiastic summary of our current understanding of the scattering problem, one encouraging result stands out: when our best measurements are made and analyzed to the best of our ability, the scattering limitations to IOSA dynamic range are forecast to be within specifications. By doing nothing more to understand and reduce waveguide scattering, we may still produce waveguides good enough for many integrated-optics applications. And they will undoubtedly get better as people make and use more waveguides for an expanding set of applications.

REFERENCES

1. M. C. Hamilton, D. A. Wille, and W. J. Miceli, "An Integrated Optical RF Spectrum Analyzer", Opt. Eng., 16 (5), 475-478 (1977).

2. W. K. Burns, P. H. Klein, E. J. West, and L. E. Plew, "Ti Diffusion in Ti:LiNbO$_3$ Planar and Channel Optical Waveguides", J. Appl. Phys., 50 (10), 6175-6182 (1979).

3. D. Marcuse, Light Transmission Optics, Van Nostrand Reinhold, New York, 1972, Chapters 8 and 9.

4. D. Mergerian, E. C. Malarky, R. P. Pautienus, J. C. Bradley, G. E. Marx, L. D. Hutcheson, and A. L. Kellner, "Operational Integrated Optical R.F. Spectrum Analyzer", Appl. Opt., 19 (18), 3033-3034 (1980).

5. H. C. Van de Hulst, Light Scattering by Small Particles, Wiley, New York, 1957.

6. K. H. Haegele and R. Ulrich, "Pyroelectric Loss Measurement in LiNbO$_3$:Ti Guides", Opt. Lett., 4 (2), 60-62 (1979).

7. J. W. Goodman, Introduction to Fourier Optics, McGraw-Hill, San Francisco, CA, 1968, Chapter 4.

8. W. T. Welford, "Laser Speckle and Surface Roughness", Contemp. Phys., 21 (4), 401-412 (1980).

9. D. W. Vahey, R. P. Kenan, and W. K. Burns, "Effects of Anisotropic and Curvature Losses on the Operation of Geodesic Lenses in Ti:LiNbO$_3$ Waveguides", Appl. Opt., 19 (2), 270-275 (1980).

10. G. B. Hocker and W. K. Burns, "Modes in Diffused Optical Waveguides of Arbitrary Index Profile", IEEE J. Quantum Electron., QE-11 (16), 270-276 (1975).

11. D. W. Vahey, N. F. Hartman, and R. C. Sherman, "Optical Waveguide Scattering Reduction II", Air Force Technical Report AFAL-TR-80-1186, Final Report for the period 2 July 1979 to 2 August 1980, prepared by Battelle Columbus Laboratories.

12. R. Holman, private communication.

13. W. K. Burns, private communication.

14. R. J. Esdaile, A. D. McLachlan, and R. M. DeLaRue, "New Aspects of Titanium Diffusion in Lithium Niobate", Talk WB3-1, Technical Digest, Conference on Integrated and Guided Wave Optics, Incline Village, Nevada, January, 1980.

15. J. L. Jackel, V. Ramaswamy and S. P. Lyman, "Elimination of Outdiffused Surface Guiding in Titanium-Diffused LiNbO$_3$", Appl. Phys. Lett., <u>38</u> (7), 509-511 (1981).

16. L. O. Svaasand, M. Eriksrud, G. Nakken, and A. P. Grande, "Solid Solution Range of LiNbO$_3$", J. Crystal Growth, <u>22</u>, 230-232 (1974).

17. D. W. Vahey, "Optical Waveguide Scattering Reduction I", Air Force Technical Report AFAL-TR-79-113, Final report for the period 15 April 1978 to 15 April 1979, prepared by Battelle Columbus Laboratories.

DATE FILMED

7-8